UC Santa Cruz

UC Santa Cruz Electronic Theses and Dissertations

Title

Low temperature properties of strong spin-orbit systems

Permalink

https://escholarship.org/uc/item/18b127t2

Author

Trinh, Jennifer

Publication Date

2016

Peer reviewed|Thesis/dissertation

eScholarship.org Powered by the California Digital Library
University of California

UNIVERSITY OF CALIFORNIA
SANTA CRUZ

LOW TEMPERATURE PROPERTIES OF STRONG SPIN-ORBIT SYSTEMS

A dissertation submitted in partial satisfaction
of the requirements for the degree of

DOCTOR OF PHILOSOPHY

in

PHYSICS

by

Jennifer Trinh

September 2016

The Dissertation of Jennifer Trinh is approved:

_____
Professor Arthur P. Ramirez, chair

_____
Professor B. Sriram Shastry

_____
Professor Frank Bridges

_____
Tyrus Miller
Vice Provost and Dean of Graduate Studies

Table of contents

List of figures……v

Abstract……ix

Acknowledgments……xi

Chapter I: Theoretical concepts……1

1. Spin-orbit coupling……1
2. Resistivity……..6
3. Magnetoresistance……7
    a. Ordinary magnetoresistance……..…8
    b. Magnetoresistance in ferromagnets……10
    c. Linear magnetoresistance (LMR)……12
        i. LMR through disorder……12
        ii. Quantum LMR……13
4. Hall effect ……...…….14
    a. Ordinary Hall effect……14
    b. Anomalous Hall effect……15
5. Thermal transport……22
    a. Specific heat……22
    b. Thermopower……...25
        i. Metals and semiconductors……..26
        ii. Phonon drag ...……27
6. Magnetic susceptibility……28

Chapter II: Experimental techniques……...31

1. Electrical transport……...31
    a. Four and five probe……..31
    b. Van der Pauw ……..33
2. Thermal transport……36
    a. Thermopower……...36
    b. Specific heat……39
3. Magnetic susceptibility……42

Chapter III: Thermodynamic measurement of angular anisotropy at the hidden order transition of URu_2Si_2……...44

1. History of hidden order……44
2. Hastatic order……...46
3. Angular anisotropy measurement……47
4. Results and discussion……50

Chapter IV: Anomalous thermopower-mobility proportionality in $FeSb_2$……..62

1. Introduction to $FeSb_2$……...62
2. Experimental setup ……..……..…63
3. Results and discussion ...……..…64
4. Discussion of proportionality between $S(T)$ and $\mu_H(T)$……...……74

Chapter V: Positive linear magnetoresistance in $BaIrO_3$……79

1. Background on $BaIrO_3$……79
2. Experimental setup……..81
3. Results and discussion……83

Chapter VI: Low-temperature effects of In doping in $CoSb_3$/$RhSb_3$……...……91

1. Background……..91
2. Experimental methods……94
3. Results and discussion……94
4. Conclusion……103

Chapter VII: Magnetic ground states of the rare earth tripod kagome lattice……...104

1. Introduction……104
2. Experimental methods ...……..106
3. Structure……108
4. Magnetic properties……..110
5. Theoretical investigation and discussion……..……112
6. Summary……118

Chapter VIII: Concluding Remarks and Outlook……..119

Appendices……121

1. Van der Pauw LabVIEW program……...121
2. Thermopower Visual Basic 6 program……....124
3. Specific heat Visual Basic 6 program……..144

References……..160

List of figures

Figure 1.1: Inverted band structure of a TI, where s and p are orbital labels. When an inverted insulator is placed next to an ordinary insulator (such as air/vacuum), the bands must cross at the surface, which results in a metallic boundary.……...3

Figure 1.2: Pyrochlore lattice unit cell with principal crystal axes and two different spin configurations for $Dy_2Ti_2O_7$, as described (and adapted from) in (Ramirez, Hayashi et al. 1999)...……..…….4

Figure 1.3: Hall effect in Ni (data from (Smith 1910), image from (Nagaosa, Sinova et al. 2010)). The low field slope is attributed to the anomalous Hall contribution while the high field slope (after saturation of magnetic moments) is due to the ordinary Hall effect. ……16

Figure 1.4: (a) Parallel transport on a flat surface and (b) on a sphere…..…...……19

Figure 1.5: Different T-dependent signatures for various magnetic phases, where AFM = antiferromagnetic, PM = paramagnetic, and FM = ferromagnetic. T_c indicates the Curie temperature while T_N is the Néel temperature. ……...……30

Figure 2.1: Five-probe configuration for Hall measurements. ……...33

Figure 2.2: The (a) standard Hall, (b) five-probe Hall. (c) clover and (d) square van der Pauw configurations. The clover configuration contacts are labeled for reference in the discussion of the vdP measurement. …….34

Figure 2.3: The van der Pauw program control window. The white background boxes indicate inputs, while the gray background boxes are outputs which display information about the measurement. ……...35

Figure 2.4: Sample puck used for thermopower measurements……..36

Figure 2.5: The Visual Basic 6 thermopower program control panel. The main plot window (center) displays the temperature drifts as a function of time for the sample and the reference, while thermopower data as a function of T are displayed in the plot window on the bottom right. The points on the plots in the figure are not actual data……...38

Figure 2.6: Control window for the dilution refrigerator specific heat program…....41

Figure 3.1: (a)The URu_2Si_2 sample used in this study. The c-axis is perpendicular to the upwards-facing plane. (b) 6 of the 19 Stycast wedges used for the angular variation between the sample's c-axis and H…….....49

Figure 3.2: Linear and nonlinear susceptibility versus temperature for fields along the c-axis ($\theta = 0°$) and in the basal plane ($\theta = 90°$)……50

Figure 3.3: Angular dependence of (a) the jump $\Delta\chi_3 3$ in the nonlinear susceptibility at the hidden order transition and (b) the magnetic susceptibility just above the hidden order transition at 18 K……51

Figure 3.4: Angular dependence of $\Delta\chi_3$ and χ_3 at three different temperatures, showing the disappearance of the Ising behavior at high temperatures……...53

Figure 3.5: $\Delta\chi_3$ as a function of $\cos^4\theta$, fit to equation 5.12 for different values of Φ. Blue dashed lines indicate Φ-values assuming an angular offset of 3° ($\theta' = \theta \pm 3°$). Inset shows the effect of Φ on the goodness of fit, expressed as the reduced χ^2……56

Figure 4.1: Electrical resistivity ($\rho(T)$) as a function of temperature. Inset a) shows the Arrhenius plot while inset b) displays the Hall coefficient for $FeSb_2$. $R_H(T)$ was extracted from the high-field (3 T – 6 T) slope of $\rho_{xy}(H)$……..…..66

Figure 4.2: Hall resistivity, $\rho_{xy}(H)$, as a function of field at select temperatures between 10 K – 30 K. Fits to the Hall mobility, $\mu_H(T)$, are shown in the inset……..67

Figure 4.3: Magnetoresistance, $\Delta\rho/\rho_0(H)$, as a function of field. The dashed lines are to help guide the eye, showing the onset of the linear magnetoresistance, LMR, at the crossover field, H_{cr}. Inset shows quadratic ($a(T)$) and linear ($b(T)$) coefficients from a fit to $\Delta\rho/\rho_0(T,H) = a(T)H^2 + b(T)H$……..68

Figure 4.4: (a) Magnetoresistance $\Delta\rho/\rho_0(T)$, and Hall mobility, $\mu_H(T)$, as a function of temperature, as compared to the linear MR coefficient from the inset of figure 2, scaled ($11b(T)$, corresponding to the left axis in units of T^{-1}). (b) The thermopower, $S(T)$, and Hall mobility, $\mu_H(T)$, as a function of temperature……71

Figure 4.5: Proportionality constant, $|S(T)|/\mu_H(T)$, scaled by ${S_{max}}^{-1}$, versus temperature for this work and two others. Inset shows S_{max} as a function of $\mu_H(T_{max})$…….....75

Figure 5.1: Schematic band diagrams showing various energy scales involved in the formation of a J^{eff} = ½ Mott insulator: (a) without SOC or U, (b) with an unrealistically large U that results in the canonical S = ½ Mott state, (c) with SOC only, (d) with both SOC and U. Adapted from (Kim, Jin et al. 2008)……80

Figure 5.2: Monoclinic 9R polytype $BaIrO_3$ (green = Ba, brown = Ir, red = O). From (Flynn, Li et al. 2016)……..82

Figure 5.3: Resistivity as a function of temperature. Inset shows $d\log\rho/dT$ (black, left axis) and $\Delta\rho/\rho_0$(red, right axis) versus temperature……..……...83

Figure 5.4: (a) Magnetoresistance as a function of field at multiple temperatures near T_c = 163 K and (b) well below T_c……85

Figure 5.5: Quadratic (a) and linear (b, left axis) coefficients of the magnetoresistance field dependence, as a function of temperature, compared to the full magnetoresistance ((b) right axis, red)…….……87

Figure 5.6: Transverse resistivity as a function of field at several temperatures. The black arrow points in the direction of decreasing temperature. Inset shows the Hall coefficient as a function of temperature, as calculated from the high field (linear) portions of the transverse resistivity curves…….....90

Figure 6.1: Crystal structure of $In_x(Co_4,Rh_4)Sb_{12}$, where the cubic sublattice is formed by the Co (Rh) atoms (blue), with Sb_4 (yellow) planar rings (green) and interstitial voids (turquoise) filled with In rattlers (red). From (Eilertsen, Li et al. 2011).……..92

Figure 6.2. Specific heat as a function of temperature squared, per mole of Co or Rh. Inset shows field dependence of $In_{0.1}Rh_4Sb_{12}$…….……..…96

Figure 6.3: Specific heat divided by temperature as a function of T^2 for $RhSb_3$ at $H = 0$ T and 6 T. Inset shows the difference between the two $C(T)$ data sets as a function of T……...97

Figure 6.4: Magnetic susceptibility as a function of temperature……...98

Figure 6.5: Temperature dependence of the sample resistivities. The inset shows and Arrhenius plot of the two semiconducting samples, Co_4Sb_{12} and $In_{0.1}Rh_4Sb_{12}$, from which the activation energies can be extracted……..100

Figure 6.6. Seebeck coefficients as a function of temperature……..102

Figure 7.1: (a) Alternating kagome and triangular layers in a pyrochlore lattice. (b) Alternating RE-kagome and Mg-triangular layers in a TKL. Dashed lines indicate a single unit cell. Local oxygen environments around RE^{3+} for (c) pyrochlore and (e) TKL. (d) A single "tripod." Dashed lines represent Ising axes…….106

Figure 7.2: (a)-(i) Temperature dependence of the inverse χ_{dc}, real part of the χ_{ac}, and magnetic specific heat C_{mag} for $Mg_2RE_3Sb_3O_{14}$. The blue dot in (c) is the Monte Carlo simulation result adopted from (Maksymenko, Chandra et al. 2015) with scaling. (j) the 120° LRO state for $Mg_2Gd_3Sb_3O_{14}$ and $Mg_2Er_3Sb_3O_{14}$. The dashed lines represent a unit cell. (k) The $\boldsymbol{k} = 0$ LRO state and (l) the $\boldsymbol{k} = (1/3,2/3)$ spin-density-wave-like state for $Mg_2Dy_3Sb_3O_{14}$……111

Figure A.1: LabVIEW block diagram for the vdP automation program corresponding to figure 2.3 and the discussion in Chapter 2.1.b……...121

Figure A.2: Main window for the vdP analysis program. A data file from the vdP automation program (figure A.1) is loaded and the data are analyzed via the vdP equation……..122

Figure A.3: Block diagram for the vdP analysis program (figure A.2)…….123

Abstract

Low temperature transport in strong spin-orbit systems

Jennifer Trinh

Spin-orbit coupling (SOC) is a relativistic interaction between the electronic spin and orbital degrees of freedom. The SOC can give rise to a variety of interesting phenomena, most notably at low temperatures in compounds composed of large-Z (atomic number) elements, since the SOC scales as Z^4. In this dissertation, I examine the low-temperature expression of SOC in the transport and magnetic properties of a representative selection of materials, including the heavy fermion system URu_2Si_2, narrow band gap semiconductor $FeSb_2$, 5d transition metal oxide $BaIrO_3$, linear band $CoSb_3$ and $RhSb_3$ skutterudites, as well as a new class of rare earth materials on a novel kagome lattice with non-collinear Ising axes, called the "tripod" kagome lattice. These compounds all feature unusual many-body properties that are either directly or indirectly linked to the large SOC present in each. In URu_2Si_2, for example, the large SOC is foundational to the hidden order (HO) phase that arises at $T_{HO} = 17.5$ K, where a remarkable magnetic signature is seen not in the linear magnetic susceptibility, χ_1, but in the leading nonlinear term χ_3. Exotic magnetic ground states are also seen in the newly synthesized rare earth tripod kagome systems. The SOC is also an important component of the inverted band structure in Dirac materials, and thus plays a role in the band formation of $CoSb_3$ and $RhSb_3$, which have both been predicted to be near a topological transition. Finally, large SOC may also be related to

interesting carrier dynamics in $FeSb_2$ and $BaIrO_3$: $FeSb_2$ displays a unique proportionality between the thermopower, $S(T)$, and Hall mobility, $\mu_H(T)$, while $BaIrO_3$ exhibits a non-saturating positive linear magnetoresistance, despite ferromagnetic order, which usually results in a negative saturating magnetoresistance. These examples showcase the importance of SOC across a range of strongly correlated phenomena spanning itinerant to localized electronic degrees of freedom.

Acknowledgments

My portion of the work presented in this dissertation was supported by the National Science Foundation through grant DGE-1339067.

The text of this dissertation includes reprints of the following previously published material: “Magnetic Ground States of the Rare Earth Tripod Kagome Lattice” by Zhiling Dun, Jennifer Trinh, Kuo Li, Minseong Lee, Kuanwen Chen, Ryan Baumbach, Yufei Hu, Yingxia Wang, Eun San Choi, B. Sriram Shastry, Arthur P. Ramirez, and Haidong Zhou, published in volume 116 of Physical Review Letters in April 2016. Kuo Li, Yufei Hi, and Yingxia Wang synthesized the first batch of the sample with the tripod kagome lattice structure at Peking University, while Minseong Lee and Eun San Choi measured the ac susceptibility at the National High Magnetic Field Laboratory (NHMFL) in Florida. Kuanwen Chen and Ryan Baumbach, also at NHMFL, measured the specific heat of the samples down to 0.4 K, while Arthur Ramirez and I measured the specific heat down to 70 mK at UC Santa Cruz. B. Sriram Shastry, who is also at UC Santa Cruz, provided much of the theoretical framework for this new class of compounds. Zhiling Dun and his supervisor Haidong Zhou at the University of Tennessee provided the final samples used in the study, and Zhiling synthesized the data into a coherent package, writing much of the paper.

Material from the URu_2Si_2 chapter of this dissertation is from a manuscript that has been submitted for publication and is currently under review by Physical Review Letters. The theoretical framework for that paper was provided by Premala

Chandra and Piers Coleman at Rutgers University, and Rebecca Flint at Iowa State University, all of whom contributed substantially to the writing. X-ray diffraction data were provided by Theo Siegrist at NHMFL and Florida State University. I conducted the experimental work and provided analysis of the data.

Finally, a manuscript based on Chapter IV of this dissertation has been submitted for review in the journal Physical Review B (Rapid Communications).

Our $FeSb_2$ samples were provided by the Siegrist lab at NHMFL/Florida State University (Lianyang Dong, Raphael Vasquez, Theo Siegrist). The $BaIrO_3$ and $CoSb_3$/$RhSb_3$ samples were provided by the Subramanian lab (Joshua Flynn, James Eilertsen, Mas Subramanian) at Oregon State University. Our URu_2Si_2 sample was grown at Bell Labs by Ekkes Brück, presently at Delft University of Technology, while the rare earth tripod kagome crystals were provided by the Zhou group (Zhiling Dun and Haidong Zhou) at the University of Tennessee.

Overall, the work in this dissertation was done in collaboration with many excellent theorists and experimental scientists, all of whom have my heartfelt thanks. Thus, while I use the first person voice in the acknowledgments, “we” will be used throughout the rest of this dissertation.

In addition to the many collaborators that I have been fortunate to work with, I am grateful to my family for their enthusiastic support, and to Jia Liu for his endless positivity and care. I would also like to thank my friends within the physics

department for providing warm companionship throughout my time at UC Santa Cruz; the physics department staff, who have always kept things running smoothly; the many professors who have supported, taught, and mentored me, especially Bud (Frank) Bridges, Josh Deutsch, and B. Sriram Shastry for their help with my dissertation; and my fellow labmates in the Ramirez lab – particularly Andrew LaForge, who was an ever-patient supervisor in my early days in the lab.

Most of all, I would like to thank my advisor, Dr. Arthur Ramirez, for his mentorship, boundless enthusiasm, and tireless example. I am grateful for the experience that I have gained under his guidance.

Chapter I: Theoretical concepts

This chapter will review concepts that are important for understanding later chapters. Each section summarizes the basic ideas most pertinent to this work. Later chapters will have more in-depth analysis when relevant. Numerous bibliographic works have also been included for further reference.

1. Spin-orbit coupling

As an electron moves in a circular orbit about a nucleus, the electron's spin magnetic moment, $\mu_s = (-ge/2mc)s$, where s is the spin-angular momentum, g is the Landé g factor, m is the particle mass, and c the speed of light, couples with the magnetic field, B, that is generated by its motion; this interaction is called spin-orbit coupling (SOC) (Shankar 1994). Note that B is distinct from H, the latter of which will be used to denote an external applied magnetic field. One result of this interaction is the splitting of the electron's energy levels based on the direction of the spin angular momentum vector relative to the orbital angular momentum. The typical energy of the SOC scales as Z^4, where Z is the atomic number that represents the number of protons in an atomic nucleus (Shankar 1994). Thus, SOC is most pronounced in systems with large Z, and therefore, with heavier elements.

While the SOC is often subsumed into other parameters, it can lead to a number of intriguing new phases that have recently come into the condensed matter

spotlight. The SOC has taken on greater importance with the prediction and observation of *topological* phases of matter, which include topological insulators and Weyl semimetals. These materials are characterized by linear bands that intersect at a single point, known as the Dirac point (Hosur and Qi 2013), and are thus known as *Dirac materials*. Dirac materials exhibit remarkable phenomena, including spin-polarized transport with spin-momentum locking, distinct surface and bulk phases, relativistic massless particles, and the possible formation of "emergent" particles like the Majorana fermion, a particle that is its own antiparticle and a potential component in future topological quantum computers (Moore 2010, Qi and Zhang 2011). The SOC energy splitting is a crucial ingredient for topological phases, as the energy splitting, coupled with a narrow (or zero) band gap, can lead to inverted conduction and valence bands, as shown in figure 1. The inverted band structure, when adjacent to that of an ordinary (un-inverted) insulator, results in a crossing of the bands at the surface of the material, and thus to a metallic surface state. So long as the two insulators remain insulating, the metallic surface is protected. Materials that exhibit such an insulating bulk and robust metallic surface are called *topological insulators* (TIs). Topological insulators and other Dirac materials hold promise for spintronics, and possibly quantum computing (Nayak, Simon et al. 2008, Qi and Zhang 2011).

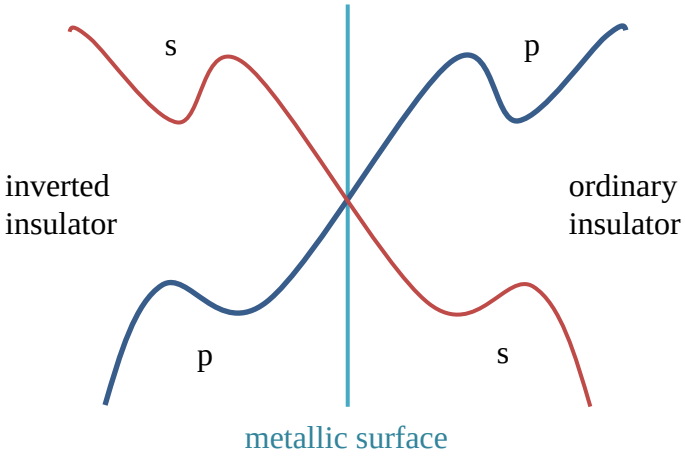


Figure 1.1: Inverted band structure of a TI, where s and p are orbital labels. When an inverted insulator is placed next to an ordinary insulator (such as air/vacuum), the bands must cross at the surface, which results in a metallic boundary.

Since Ir has one of the largest SOC constants of all the transition metals (Cotton and Cotton 1999), iridates exhibit a particularly strong SOC (~0.4 eV) that competes with the comparable energy scales of the Coulomb repulsion, U, and the energy bandwidth, W, and results in exotic behavior (Witczak-Krempa, Chen et al. 2014). Transition metals that are lower on the periodic table have larger orbitals, and for Ir, which is a 5d transition metal, the orbitals are thus expected to overlap to form delocalized states. Many Ir oxides, however, exhibit narrow band gaps at low temperatures that can be related to SOC splitting, and often display unexpected magnetic order or other exotic phases. The pyrochlore and layered iridates, for example, can exhibit Mott insulator behavior, frustrated magnetism, topological order, spin-liquid, and non-fermi liquid behavior (Okamoto, Nohara et al. 2007, Li, Kong et al. 2013, Witczak-Krempa, Chen et al. 2014). These transition metal oxides

(TMOs) are rife with interesting physics and have become a popular topic of study in recent years.

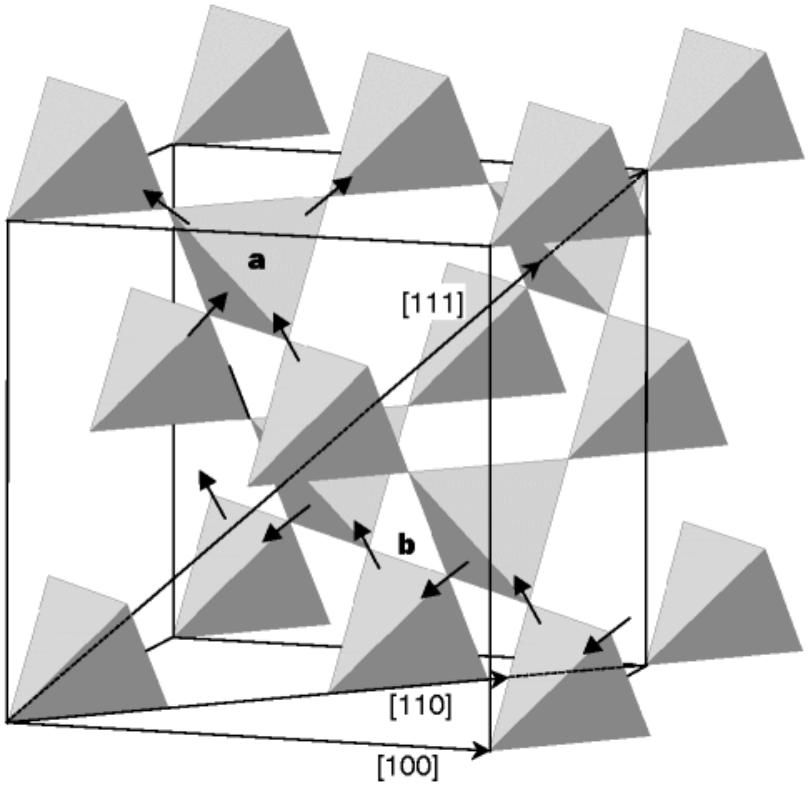


Figure 1.2: Pyrochlore lattice unit cell with principal crystal axes and two different spin configurations for $Dy_2Ti_2O_7$, as described (and adapted from) in (Ramirez, Hayashi et al. 1999).

The rare earth pyrochlores also feature interesting properties due to the complex interplay among SOC (by virtue of its formative role in determining spin dimensionality), dipolar, and exchange interactions. For example, because of the non-uniaxial Ising effective spin, $Ho_2Ti_2O_7$ and $Dy_2Ti_2O_7$ exhibit a spin ice state, where frustrated interactions result in a multiplicity of ground states and therefore a residual entropy (Ramirez, Hayashi et al. 1999, Bramwell, Harris et al. 2001), while $Er_2Ti_2O_7$

displays quantum-order-by-disorder physics, where quantum fluctuations lift a classical degeneracy, resulting in an ordered state (Savary, Ross et al. 2012). The pyrochlore structure, which consists of alternating kagome and triangular layers due to corner-sharing tetrahedra (figure 2), possesses symmetry that leads to frustrated interactions between magnetic rare earth ions. The strong SOC in these materials adds further to the intrigue.

Uranium, which has an even higher Z (= 92), can form a variety of compounds that display superconductivity and heavy fermion behavior (Ott, Rudigier et al. 1983, Stewart, Fisk et al. 1984). In U compounds, the SOC competes with a number of energy scales, including the Coulomb interaction, 5f bandwidth, exchange interaction, and Kondo interaction, which famously gives rise to heavy fermion behavior (Mydosh and Oppeneer 2011), thus stimulating a multitude of novel effects, most prominent of which is the observation that the heavy Fermi quasiparticles can undergo a transition to a superconducting state.

Later in this work, we examine the expression of SOC in a representative selection of materials, including the heavy fermion system URu_2Si_2, the cryogenic thermoelectric candidate $FeSb_2$, the 5d TMO $BaIrO_3$, the nearly topological $CoSb_3$ and $RhSb_3$ skutterudites, as well as a new class of materials with the rare earth tripod kagome lattice (Dun, Trinh et al. 2016). These materials serve as a broad introduction to the wealth of phenomena enabled by SOC.

2. Resistivity

Many of the results presented here will rely on a good understanding of charge transport, the most basic of which is the electrical resistivity, $\rho(T)$. Such measurements can provide a wealth of information about the microscopic processes that govern charge motion and interactions in metals and semiconductors, thus rendering them an invaluable tool for probing systems with strong SOC. The temperature dependence of $\rho(T)$ can discern the presence of a gap, information on scattering rates, electron pairing mechanisms, and other local short-range interactions (Tahir-Kheli 2013). Adding one or two parameters to the basic $\rho(T)$ measurement, such as magnetic field, H, and direction, can provide information about the dominant scattering effects, as well as the charge carrier density and sign, which in turn provide insight into the interactions that charge carriers have with local magnetic moments, the ionic potentials (Fermi surface mapping), and each other (strong correlations). Routine experimental protocols for magnetoresistance ($\Delta\rho/\rho_0(T,H) \equiv (\rho(T,H) - \rho(T,H=0))/\rho(T,H=0)$) and Hall effect have been developed to systematically determine charge-field interactions. The protocols and techniques for studying such effects have also advanced to the stage of technological importance. For instance, $\rho(T)$, Hall effect, and $\Delta\rho/\rho_0(H)$ are all presently used in applications such as information storage and remote sensing, and in spintronics, which have been proposed as the physical basis for new information technologies (Wolf, Awschalom

et al. 2001). The next few sections will provide an overview of current theoretical frameworks for understanding and analyzing magnetoresistance and Hall effect data.

3. Magnetoresistance

Narrow band gap systems (NBGs, with E_g on the order of a few hundreds of meV (Klimm 2014)) are very sensitive to extrinsic effects, such as impurities and defects, which can significantly alter transport properties by adding states in the gap or increasing the degree of disorder. While $\rho(T)$ can provide some information regarding high levels of these defects, $\Delta\rho/\rho_0(T,H)$ is a more sensitive probe for revealing details about local scattering effects. For example, the change in $\rho(T)$ in a magnetic field can be orders of magnitude in manganese-based perovskites, displaying *colossal magnetoresistance* (CMR) (Ramirez 1997). The effect has been attributed to double exchange interactions among Mn^{3+} and Mn^{4+} ions, modified by a strong electron-phonon coupling. Such a microscopic description was proposed in order to explain simultaneous changes in $\rho(T)$ and $M(T)$, thus demonstrating the significance of $\Delta\rho/\rho_0$, but also its complexity.

In this section, we focus on a few experimental signatures of $\Delta\rho/\rho_0$. We start with the basic ordinary $\Delta\rho/\rho_0$ and build upon our understanding of it in order to examine the negative $\Delta\rho/\rho_0$ (NMR) commonly found in ferromagnets, as well as linear $\Delta\rho/\rho_0$ (LMR), which has been of great interest recently due to its prevalence in

a number of novel materials systems, two of which will be examined in Chapters IV and V. Additionally, $\Delta\rho/\rho_0$ can be useful for field sensing and memory storage applications, and so materials that exhibit large or linear $\Delta\rho/\rho_0$ can also have technological importance. Here, we present a broad overview of the sources for $\Delta\rho/\rho_0$ and LMR.

a) Ordinary magnetoresistance

In the absence of additional interactions, the ordinary $\Delta\rho/\rho_0$ (OMR) is due to the Lorentz force on an electron in a magnetic field,

$$F = -e(E + v \times \mu_0 H), \tag{1.1}$$

where e is the elementary charge, E is the electric field, B is the magnetic induction, v is the velocity of the charge carrier, and μ_0 is the permittivity of free space. From this equation, it should be clear that the longitudinal $\Delta\rho/\rho_0$ (with $v \parallel I \parallel H$) should be zero. The magnetic field component of the Lorentz force causes the charge carriers to travel in a curved trajectory that is perpendicular to both v and H, completing a circular path with frequency

$$\omega_c = {eH}/{m^*}, \tag{1.2}$$

called the cyclotron frequency (Ashcroft and Mermin 1976). Here m^* is the effective carrier mass. This curved trajectory leads to an increased path length, thus increasing

the number of scattering events for a charge carrier traversing the sample . In metals with a single scattering mechanism and carrier scattering time τ that is approximately constant at all points on the Fermi surface, the transverse MR can be expressed as a function of H/ρ_0 – that is,

$$\Delta\rho/\rho_0 = F\left(H/\rho_0\right), \tag{1.3}$$

a near universal relation known as *Kohler's rule*. To derive Kohler's rule, we write ω_c in terms of the zero-field conductivity, given by

$$\sigma_0 = ne^2\tau/m^*, \tag{1.4}$$

where n is the carrier density. In terms of σ_0, ω_c becomes

$$\omega_c\tau = H\sigma_0/ne. \tag{1.5}$$

The left-hand side is the average number of cycles completed by a carrier in circular orbit, given τ. Thus, in a system with a single scattering mechanism, $\rho(T)$ in a field can be thought of as a simple function of the linear dimension of the carrier trajectory, which is proportional to the number of cyclotron orbits, or $\omega_c\tau$. An increase in H leads to a proportional increase in $\omega_c\tau$, whence follows Kohler's rule.

The OMR can range from a few percent up to 200% for $H < 1$ T (Feng and Jin 2005). In this low field scenario, $\Delta\rho/\rho_0$ should be even in H and analytic at

$H = 0$ in order to satisfy time reversal invariance, which leads to a H^2-dependence (Pippard 1989). In higher fields (typically $H > 2$ T) with closed orbits, $\Delta\rho/\rho_0$ tends to saturate.

b) Magnetoresistance in ferromagnets

Magnetic order adds a layer of complexity that gives rise to a host of unique types of $\Delta\rho/\rho_0$. One such type is *giant magnetoresistance* (GMR, distinct from the CMR discussed above), which arises across ferromagnetic (FM)/antiferromagnetic (AFM) boundaries (Baibich, Broto et al. 1988). Meanwhile, *tunnel magnetoresistance* (TMR) occurs in magnetic tunnel junctions, or systems consisting of two ferromagnetic layers with a thin layer of insulating material in between, which carriers must tunnel through (Yuasa, Nagahama et al. 2004). These effects, in addition to CMR and other types of $\Delta\rho/\rho_0$ in multi-layered structures, have led to technological advancements in memory read/write devices and storage, and are the foundation for modern spintronics applications (Wolf, Awschalom et al. 2001).

Here, we focus on $\Delta\rho/\rho_0$ in *bulk* ferromagnets. Although most materials have a positive (ordinary) magnetoresistance due to a deflected electron trajectory in the presence of H, some systems, such as ferromagnets, exhibit negative magnetoresistance (NMR) as a result of interactions between spins. In ferromagnets, the increased domain ordering and suppressed spin fluctuations lead to a decrease in

resistance with increasing H, with the effect typically on the order of a few to a few tens of percent (Yamada and Takada 1972, Falicov and Hood 1994). The NMR is most pronounced near the ferromagnetic transition temperature, T_c, where critical fluctuations dominate and usually result in a negative peak in $\Delta\rho/\rho_0$ at T_c (Balberg and Helman 1978).

Additionally, bulk ferromagnets exhibit a longitudinal $\Delta\rho/\rho_0$, contrary to the OMR case. However, the longitudinal $\Delta\rho/\rho_0$ is often different in magnitude from the transverse (typically by a few percent (Li, Wang et al. 2009)), and this difference is quantified through the *anisotropic magnetoresistance* (AMR), defined as $\Delta\rho_{AMR} = \rho_{\parallel} - \rho_{\perp}$ (Mcguire and Potter 1975). This difference is a result of SOC, and can therefore vary drastically from compound to compound, depending on the SOC strength and orbital anisotropy (Getzlaff 2008). A simple way to understand the effect is that, when $H \perp I$, one can think of the carrier orbit as being in the plane of I, which results in a smaller cross section for scattering, while for $H \parallel I$, the electronic orbit is oriented perpendicular to I and leads to more scattering. Most materials only exhibit an AMR of a few percent, but perovskite manganite films can exhibit an AMR of over 30% (Li, Wang et al. 2009), while an AMR of up to 50% has been reported in ferromagnetic U compounds (Wisniewski 2007). AMR was previously used for applications in digital recording, magnetic bubble memory devices, and magnetic field sensors, but have since been replaced with more efficient technologies (Freitas, Ferreira et al. 2007).

c) Linear magnetoresistance (LMR)

As mentioned above, the ordinary $\Delta\rho/\rho_0$ should result in a quadratic H-dependence that saturates at $H > 2$ T. In 1928, however, Peter Kapitza observed linear $\Delta\rho/\rho_0$ (LMR) in elemental bismuth (Kapitza 1928), and it was inferred to be a common effect, then called "Kapitza's law." Further studies ultimately concluded that LMR only occurs in specific circumstances. We will discuss a few of those cases below.

i) LMR through disorder

We start with the most common classical route to LMR: disorder. In 1960, Conyers Herring published a treatise on the effects of inhomogeneities on "galvanomagnetic" properties (Herring 1960). His study found that, at high enough fields, $\Delta\rho/\rho_0$ would have a correction that was linear in H. The linear $\Delta\rho/\rho_0$ arose from Hall field (transverse electric fields in the plane) fluctuations, which arise due to the inhomogeneities. In 2000, Parish and Littlewood built upon this model by taking the limit of strong disorder, as seen in the silver chalcogenides, Ag_2Se and Ag_2Te (Parish and Littlewood 2005). In their model, strong disorder took the form of a four-terminal network of circular resistors, each with a random value. As in Herring's model, the disorder leads to fluctuations in the carrier mobility that are manifested as

an admixture of longitudinal and Hall contributions, thus leading to LMR. Unlike in Herring's model, however, Parish and Littlewood have the additional prediction that the low-field limit will be quadratic in H, and that the crossover field will go as either $\langle\mu\rangle^{-1}$ or $(\Delta\mu)^{-1}$, where $\langle\mu\rangle$ is the average mobility while $\Delta\mu$ is the width of the mobility disorder (Parish and Littlewood 2003). We will revisit this model in Chapter IV.

Disorder can also lead to a positive LMR in ferromagnets. Manyala et al. similarly found that disorder could lead to a linear in H correction due to quantum interference effects (Manyala, Sidis et al. 2000). Here, the effect is slightly different from the Herring or Parish-Littlewood case, as the disorder and ferromagnetic order lead to electron-electron interaction events that cause their wavefunctions to interfere coherently. A similar theory for disordered paramagnetic metals has previously been posited (Lee and Ramakrishnan 1985).

ii) Quantum LMR

Quantum LMR has been of particular interest recently due to its relevance to topological systems, which exhibit LMR related to their linear bands (Singh, Gopal et al. 2016). First proposed by A. Abrikosov in 1998 (Abrikosov 1998), quantum LMR was hypothesized to occur in systems where the Landau levels are well-formed and all of the electrons have coalesced into the lowest Landau level. This condition has

been termed the quantum limit, given by $\hbar\omega_c > E_F$, where ω_c is defined in equation 1.2 and E_F is the Fermi energy. The *extreme quantum limit* can be expressed as

$$n \ll \left(\frac{eH}{\hbar c}\right)^{3/2} \text{ and } T \ll \frac{eH\hbar}{m^* c} \tag{1.6}$$

(Abrikosov 2000). These conditions are thought to be met in systems with gapless linear dispersions, or in inhomogeneous polycrystalline semiconductors with gaps narrow enough that the disorder can lead to an electronic energy spectrum that resembles that of a semimetal (e.g. the non-stoichiometric silver chalcogenides, $Ag_{2\pm\delta}Te$ and $Ag_{2\pm\delta}Se$ (Lee, Rosenbaum et al. 2002)). Both descriptions can apply to Dirac materials, and thus QLMR has been a popular model for explaining LMR in materials like graphene (Friedman, Tedesco et al. 2010). However, many of these materials that exhibit LMR also have some degree of disorder thus leading to ambiguity between the QLMR and disorder-driven classical MR. The question is then whether the disorder gives rise to a classical LMR based on additional Hall field contributions, or to a gapless band in the quantum limit. Both the Parish-Littlewood model and the QLMR model have been applied throughout the literature (Hu, Rosenbaum et al. 2005, Zhang, Yu et al. 2011).

4. Hall effect

a) Ordinary Hall effect

As discussed above, charge carriers experience the Lorentz force in the presence of an applied field, H. In a transverse configuration, wherein the voltage leads are placed perpendicular to I (ρ_{xy} is measured), H leads to a potential difference, called the Hall voltage, between the edges of the sample. A charge carrier will travel to one edge of the sample or the other depending on its sign; thus, the sign of the Hall voltage provides the sign of the charge carriers. Additionally, because the Hall voltage is independent of τ and m^*, it can directly yield the carrier density through

$$R_H = {}^{1}/_{ne}. \tag{1.7}$$

For a full derivation, see (Ashcroft and Mermin 1976). Thus, the Hall effect measurement is an invaluable tool for sample characterization. We will discuss Hall effect measurement techniques in the next chapter.

b) Anomalous Hall effect

In 1881, Edwin Hall found that ferromagnetic iron exhibited a "pressing current" (current that was "pressed" toward one side of the sample) that was ten times larger than in nonmagnetic conductors (Nagaosa, Sinova et al. 2010). This effect is now known as the Hall effect, and the additional contribution to the transverse resistivity found in magnetic materials is known as the *anomalous* (or extraordinary)

Hall effect. Studies have demonstrated that the Hall effect can more fully be written as

$$\rho_{xy} = R_H H + R_{AHE} M, \tag{1.8}$$

where M is the magnetization of the sample and R_{AHE} is the Hall coefficient associated with the AHE (Pugh 1930). However, in many systems, the actual relationship is more complex, as the total field felt by electrons as they traverse through the material is often difficult to determine, especially if the internal field is spatially dependent due to inhomogeneities. Hall effect data in many magnetic systems have thus eluded explanation throughout the years; nonetheless, the term "anomalous Hall effect" has been nearly universally applied to them.

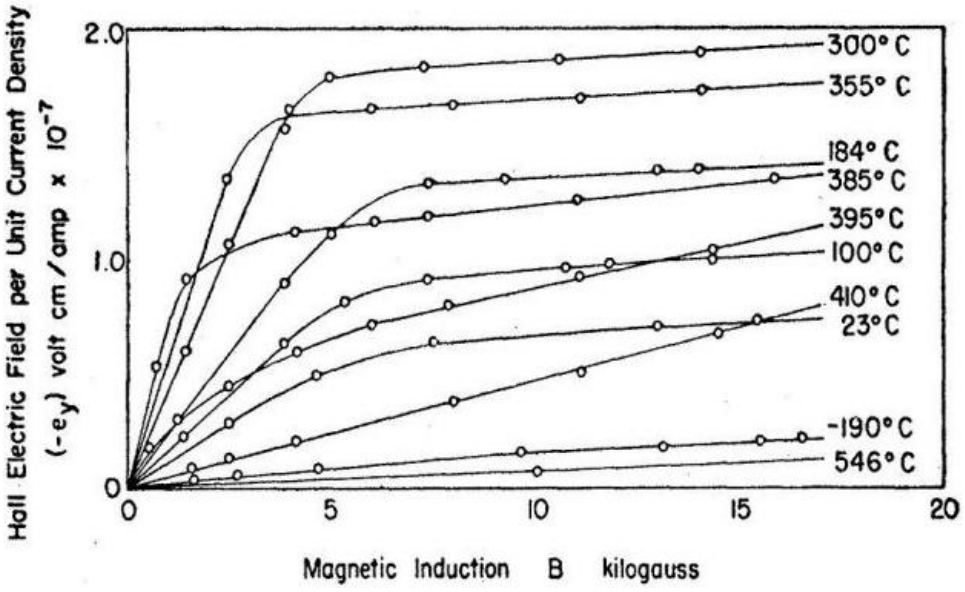


Figure 1.3: Hall effect in Ni (data from (Smith 1910), image from (Nagaosa, Sinova et al. 2010)). The low field slope is attributed to the anomalous Hall contribution while the high field slope (after saturation of magnetic moments) is due to the ordinary Hall effect.

The origin of the anomalous Hall effect (AHE) at low fields in magnetic materials was heavily debated in the past, due to uncertainty in both the distinctions and interactions among various proposed effects, as well as a lack of alternative methods of verification (Nagaosa, Sinova et al. 2010). However, three main explanations have emerged. In 1954, Karplus and Luttinger (KL) proposed an "anomalous velocity" mechanism that attempted to explain effects seen in ferromagnetic and strongly paramagnetic samples through the spin-orbit interaction of magnetically polarized conduction electrons (Karplus and Luttinger 1954). KL found that the field-induced Hall current was proportional to the degree of magnetization in the sample as in equation 1.8, independent of scattering effects from disorder. Given the insensitivity to disorder, KL's explanation was initially discounted. In 2002, Jungwirth et al. reframed KL's model in terms of the Berry Phase, which is a quantum mechanical phase that arises when an electron evolves adiabatically through a closed loop in parameter space, and leads to the change in group velocity that is the KL anomalous velocity (Berry 1984, Jungwirth, Niu et al. 2002). The anomalous velocity is now understood as a correction to the quasiparticle group velocity perpendicular to the electric field, as if in the presence of another fictitious magnetic field, due to topological properties of the Bloch states (Nagaosa, Sinova et al. 2010). The KL anomalous velocity has since gained favor as a primary AHE mechanism.

The anomalous velocity mechanism is closely related to the geometrical concept of parallel transport. In parallel transport, a vector a is transported about a closed loop on a surface and is kept tangent to the surface at each point (see figure 1.4). As well, a is not allowed to rotate about the normal vector at each point – in other words, it is kept as parallel as possible to its original orientation at each displacement about the loop (analogous to the condition of adiabaticity). After completing an arbitrary loop on a flat surface, a will point in exactly the same direction as its initial orientation. However, if the surface is curved (e.g. the surface of a sphere), then a will point in a direction different from the initial direction (see figure 1.4). The angle between the initial and final orientations is called the "anholonomy angle," and is determined by the path taken and the total curvature of the surface. The total curvature of a surface is a topological invariant called the *Euler characteristic*, χ, expressed as

$$\iint K da = 2\pi\chi \,, \tag{1.9}$$

where K is the local curvature and the integral is over the entire surface (Weinstein). The Euler characteristic stays the same regardless of how the surface is warped or bent. For example, the Euler characteristic of an ellipsoid is 2, as it is for sphere.

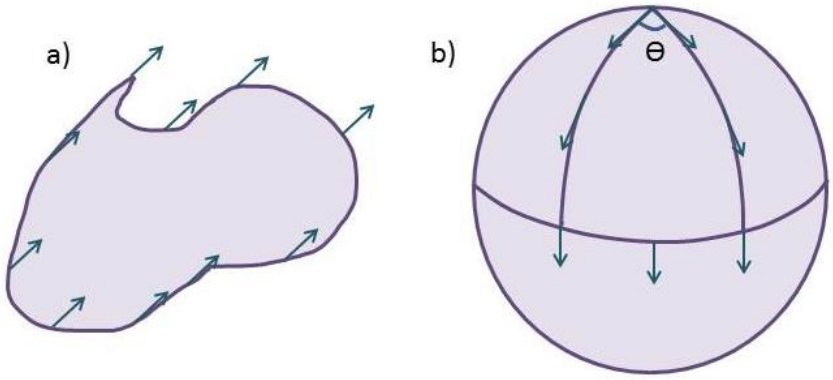


Figure 1.4: (a) Parallel transport on a flat surface and (b) on a sphere.

The Berry phase is a quantum mechanical anholonomy angle, which takes the form of an additional phase in the wave function after it is adiabatically parallel-transported about a closed loop in parameter space. The curvature of the space, also called the Berry curvature, determines the Berry phase.

In the presence of an electric and magnetic field, it is well known that the charge carrier velocity gains an $E \times H$ drift velocity term (Jackson 1999). The Berry curvature (Ω) is akin to an effective magnetic field, which leads to the anomalous velocity of KL's theory for AHE. The anomalous velocity contributes to the transverse Hall current, and is only dependent upon details of a system's band structure (independent of scattering). Given that

$$j = \rho v, \tag{1.10}$$

and

$$\hbar v = \nabla E_n - eE \times \Omega, \tag{1.11}$$

we get a transverse contribution to the current,

$$\sigma_{xy} = {ne^2}/{\hbar\langle\Omega\rangle}. \tag{1.12}$$

Since this contribution to the Hall current is independent of scattering or disorder, KL's AHE mechanism is often called the *intrinsic anomalous Hall effect*, and it is ultimately due to the effects of spin-orbit coupling on host atoms (not impurities).

An alternative to KL's anomalous velocity theory was presented by Jan Smit in 1955 in order to explain additional Hall contributions in nickel alloys (Smit 1955). According to Smit, polarized carriers could undergo anisotropic scattering processes due to spin-orbit coupling with impurities, which would lead to an additional contribution to the Hall effect. This mechanism for the AHE was called "skew scattering," and *is* dependent on the carrier scattering lifetime, τ. In short, due to SOC, the transition probabilities from one state to another (quantum number $n \to m$) are not necessarily the same in the opposite direction ($m \to n$), as one might naively expect from reciprocal transition probabilities, i.e. Fermi's Golden Rule. Thus, transitions that are right-handed relative to the H-field have different probabilities from the corresponding left-handed transition, which results in an asymmetric chiral contribution to the transverse Hall current (Nagaosa, Sinova et al. 2010).

Since the skew scattering contribution to the AHE is proportional to τ, skew scattering dominates in the clean limit ($\tau \to \infty$) where the time between scatterings is long. However, beyond impurity scattering, scattering can occur off of phonons,

magnons, and ferromagnetic critical fluctuations, meaning that it is important to consider temperature ranges when determining the applicability of skew scattering to a system. Skew scattering is also called the *extrinsic anomalous Hall effect*, as it is due to spin-orbit coupling on impurity atoms and dependence on τ. In some cases, the extrinsic AHE can dominate over the intrinsic AHE at low T, as the extrinsic AHE increases with decreased scattering, wheras the intrinsic AHE is relatively T-independent.

A third contribution to the AHE, called the "side-jump" mechanism, was proposed by Berger in 1970, and is due to the difference in delayed wavefronts experienced by electrons of opposite spins in the vicinity of an impurity (Berger 1970, Nagaosa, Sinova et al. 2010). Berger calculated that, upon scattering from a centrosymmetric potential (impurity atoms), carriers experience a discontinuous sideways translation ($\Delta y \simeq 10^{-10}$ m (Chien and Westgate 1980)) due to spin-orbit coupling. Thus, despite a sideways displacement, the particle continues parallel to its original trajectory, unlike in skew scattering, where the electron trajectory is deflected at a constant angle. Although the effect is due to the spin-orbit interaction between electrons and impurities, as in skew scattering, side-jump does not depend on τ, just as in the intrinsic case. Thus, it is experimentally difficult to separate the intrinsic KL AHE from the side-jump AHE, and can only definitively be done through calculation.

Most magnetic systems exhibit some form of intrinsic AHE, including the manganites, pyrochlore ferromagnets, dilute magnetic semiconductors, and many

more (Nagaosa, Sinova et al. 2010). Skew scattering appears to dominate in systems where impurity scattering is augmented by scattering from other effects, such as Kondo scattering (heavy fermion systems) and ferromagnetic critical fluctuations. We will briefly examine the AHE in the transition metal oxide system $BaIrO_3$.

5. Thermal transport

Thermopower ($S(T)$) and specific heat ($C_p(T)$) are two different ways in which to probe the heat or entropy of a system. The thermopower is a measure of the heat (or entropy) per carrier in the presence of a thermal gradient, and is sensitive to band structure (gap) and electron-phonon interaction effects. Meanwhile, $C(T)$ provides information on the heat (or entropy) of the entire system, which can be separated into the Fermi contribution from electrons, lattice heat, and magnetic entropy. These two measurements reveal important characteristics that will be crucial to our discussions in later chapters.

a) Specific heat

The $C(T)$ is the amount of heat required per mole to raise the material's temperature a degree

$$C(T) = \frac{Q}{\Delta T}, \tag{1.13}$$

where Q is the heat. The heat excites phonons (which lead to an increased temperature), magnetic excitations, or electrons within $k_B T$ of the Fermi energy. Thus, the itinerant Fermi liquid electron contribution is only significant in metals, where γ can range from ~0.4-16 mJ/mol-K^2 in elemental metals (Ashcroft and Mermin 1976). It can be shown that the dispersion relations of the phonons and electrons lead to a $C(T)$ of the form

$$C(T) = \gamma T + bT^3, \tag{1.14}$$

where the T-linear and T-cubic terms are due to the electronic and lattice contributions, respectively (Ashcroft and Mermin 1976). The coefficient γ is called the *Sommerfeld coefficient* and is related to the metallic density of states and particle mass via

$$\gamma = \frac{\pi^2}{3} {k_B}^2 g(\varepsilon_F),\ g(\varepsilon_F) = \frac{m k_F}{\hbar^2 \pi^2}, \tag{1.15}$$

where $g(\varepsilon_F)$ is the density of states at the Fermi energy, ε_F, and k_F is the Fermi wave vector (Ashcroft and Mermin 1976). Thus, γ is an invaluable tool for probing heavy fermion systems that have an enhanced m^*. By some estimates, m^* can reach $\sim 200 m_e$ in $CeCu_2Si_2$, UPt_3, and UBe_{13}, as indicated by very large γs in the range of 450 – 1600 mJ/mol-K^2 (Stewart 1984). The T^3 coefficient, b, characterizes the lattice contribution and yields the Debye temperature. Thus, $C(T)$ is a very useful quantity for probing the electron and phonon systems, but also for uncovering exotic

interactions or phenomena, as in the case when additional contributions to $C(T)$ are found beyond those in equation 1.14.

Beyond the linear γ-term and cubic lattice term, other features can occur in $C(T)$, such as peaks or discontinuities, which signify changes in entropy, S. To understand this, we note that $C(T)$ can also be expressed as

$$C_P = T\left(\frac{\partial S}{\partial T}\right)_P, \tag{1.16}$$

where the P subscript indicates isobaric conditions. Therefore, integrating $C(T)$ yields S. This information is important for characterizing phase transitions, where the order parameter (which quantifies the degree of symmetry breaking) fluctuates, representing additional degrees of freedom in the critical region. The entropy change is usually quite dramatic and results in a peak or discontinuity in $C(T)$.

In Chapters III and VII, we will be using such features in $C(T)$ to gain insight into magnetic phase transitions. A magnetically ordered phase is one wherein the ground state consists of an ordered arrangement of magnetic spins, such as in ferromagnets, where all spins point in the same direction, or in antiferromagnets, where neighboring spins are antialigned. Magnetic order thus breaks rotational symmetry, and the order parameter is the net magnetization (or staggered magnetization, in the case of antiferromagnets), $M = \chi H$, where χ is the magnetic susceptibility (discussed below). The peak in $C(T)$ is a result of the increased entropy as the spins flip and become ordered as T is decreased. Thus, peaks in $C(T)$ are

always a sign of magnetic order, and $\chi(T)$ is often used as a complementary experiment. We will discuss $\chi(T)$ later.

b) Thermopower

Many applications exist for the thermopower, $S(T)$, as it can lead to increased efficiency in systems with heat as a byproduct, such as in automobiles. For example, BMW's TurboSteamer system, which utilizes thermoelectric (TE) materials, might increase fuel efficiency by 15% (Vining 2009). In order to characterize the suitability of a material for TE applications, the figure of merit, ZT, is used, where

$$ZT \equiv \frac{\sigma S^2}{\kappa} T. \tag{1.17}$$

Here, σ is the electrical conductivity and κ is the thermal conductivity. Materials with a ZT (>1) are efficient enough for applications in both heating/cooling (cooling efficiency of 2-5%) and in energy efficiency (power conversion efficiency of 10-20%) (Zhang and Zhao 2015). The use of TEs is ideal as a supplementary source of electricity, or in situations when maintenance cannot be performed, due to the lack of moving parts and reliability of TEs (Tritt 2011). For example, TEs have already been implemented in large commercial trucks for increased fuel efficiency (up to 20% (Yang 2005)), cooling in desktop refrigerators, and even for powering space exploration modules in the form of radioisotope thermoelectric generators , which are powered by heat from radioactive plutonium (Rowe 1995).

Beyond technological applications, $S(T)$ can also be used to characterize materials in a more fundamental manner, such as by providing the sign of charge carriers, much like the Hall effect, or probing electron-phonon interactions. The thermopower can also be thought of as the entropy per carrier, and so can provide further insight into the density of states and carrier dynamics. Here, we will discuss properties of $S(T)$ that will be relevant to Chapter IV.

i) Metals and semiconductors

In metals, the heat carried by the electrons will be roughly equal to the electronic specific heat per charge, $\frac{c_{el}}{q} \sim {k_B}^2 T/eE_F$ (Chaikin 1990). The standard expression by Mott is (Mott and Davis 1979)

$$S = \frac{\pi^2}{3}\frac{{k_B}^2 T}{e}\left(\frac{d\ln\sigma}{dE}\right)_{E=E_F}. \tag{1.18}$$

In metals, where $E_F \gg k_B T$, this leads to an approximate upper limit on the magnitude of $S(T)$ of $|k_B/e|$ = 87 μV/K.

For commercial TE applications, a larger $S(T)$ is desirable for an enhanced ZT, and so most TE materials (with the exception of thermocouples) are semiconductors, which often feature a higher $S(T)$ than in metals due to the additional energy needed to excite carriers to the conduction band. The standard equation for $S(T)$ is (Fritzsch.H 1971)

$$S = \frac{k_B}{e}\left(\frac{E_C - E_F}{k_B T} + A\right), \tag{1.19}$$

where $E_C - E_F$ is the difference between the conduction band and Fermi level, which is therefore roughly equivalent to the heat per carrier, and A is a constant of order unity. Thus, $S(T)$ can be used to estimate the size of the gap in semiconductors, assuming the Fermi level lies in the center.

ii) Phonon drag

In the presence of a temperature gradient, charge carriers diffuse from the hot end to the cold end of the sample, and the phonons also travel in the same direction. Thus, in systems with strong electron-phonon coupling, the phonons and electrons scatter, leading to an additional effective electric current as the phonons "drag" the electrons towards the cold end. This effect is known as *phonon drag*. In order for the sample to reach thermal equilibrium under these conditions, the voltage created by the difference in chemical potential on either end of the sample must overcome this electron-phonon effect, which is similar to an additional effective electric field with a carrier drift velocity of $v = \mu E$. This leads to an additional $S(T)$ contribution of the form

$$S_{pd}(T) = \frac{x v^2 \tau_{ep}}{\mu T} \tag{1.20}$$

where x has a value of between 0 and 1 and represents the fraction of collisions that involve phonons, v is the average drift velocity of the electrons due to electron-phonon interactions, τ_{ep} is the scattering time between electron-phonon events, and μ is still the carrier mobility (Goldsmid 2010). Phonon-drag enhances $S(T)$, regardless of the sign of the carriers. This effect is most prominent at low temperatures, when optical phonon scattering is no longer relevant (thus minimizing phonon-phonon scattering) and only acoustic phonon scattering is present. Thus, a low temperature (~10 K) peak in $S(T)$ is a common indicator of phonon drag effects. As seen in equation 1.20, $S_{pd}(T)$ is inversely related to the carrier mobility. This will be an important point in Chapter IV.

6. Magnetic susceptibility

The magnetic susceptibility, $\chi(T)$, relates the magnetic polarization (magnetization) of a sample, M, to the applied magnetic field, H, through $M = \chi H$. Thus, $\chi(T)$ provides information on the type of magnetism or magnetic impurities present in a compound. All materials exhibit at least a small diamagnetism, or a negative $\chi(T)$, due to valence, or core, electrons. A positive $\chi(T)$ can indicate ferromagnetism, antiferromagnetism, or paramagnetism.

Paramagnetism is a mostly T-independent effect due to unpaired electrons, that is generally larger in magnitude than the intrinsic (core) diamagnetism. At low

temperatures, however, $\chi(T)$ can diverge in what is called a *Curie tail*, due to paramagnetic impurities. Thus, the Curie tail can be used to estimate an impurity density.

Signatures of FM and AFM order in $\chi(T)$ are more distinct (figure 1.5). As the temperature is lowered, the transition into an ordered state is often made continuously through the formation of domains, wherein spatially localized groups of spins become correlated as H is increased. In ferromagnets, the domains align as H is increased until the saturation magnetization (M_s) is reached, beyond which the magnetic response is nearly constant. In order to reverse this process, a $-H$ must be applied, and the magnitude of H required to demagnetize the sample is called the *coercivity* (H_{co}). Materials with a large coercivity ((H_{co} ~ 1-10 T) are called *hard* FMs, and hard FMs that also have a large energy product (($BH)_{max}$~300 kJ/m^3) are used as commercial permanent magnets due to their robust magnetism (Coey 2001).

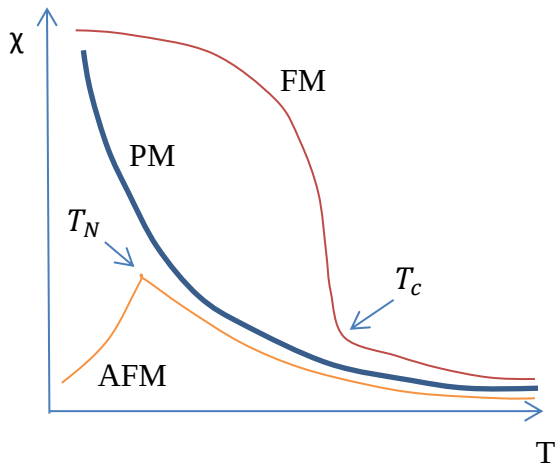


Figure 1.5: Different T-dependent signatures for various magnetic phases, where AFM = antiferromagnetic, PM = paramagnetic, and FM = ferromagnetic. T_c indicates the Curie temperature while T_N is the Néel temperature.

A measurement of $\chi(T)$ corresponds to the first term in the expansion

$$M = \chi_1 H + \frac{1}{3!}\chi_3 H^3 + \frac{1}{5!}\chi_5 H^5 + \cdots, \tag{1.21}$$

where only odd terms contribute due to the time-reversal symmetry breaking effect of the magnetic field. However, in some materials, such as rare earth systems with higher-order crystal field terms in the Hamiltonian, the leading nonlinear contribution to $\chi(T)$, χ_3 can provide important insight into the energy spectrum of the system, for example, as a probe of higher order multipolar order (multispin correlations) or exotic spin order (Chalupa 1977, Ramirez, Coleman et al. 1992). Thus, χ_3 (often referred to as the nonlinear susceptibility) is an important tool for examining the hidden order phase in URu_2Si_2, discussed in Chapter III.

Chapter II: Experimental techniques

This chapter will outline the experimental techniques used in the latter chapters of this dissertation. Measurements from T = 2 K – 300 K were performed using commercial cryostats from Quantum Design: a Physical Properties Measurement System (PPMS) for thermal and electrical transport measurements and a Magnetic Properties Measurement System (MPMS) for magnetization. From 1.5 K down to 50 mK, $C(T)$ measurements were performed in an Oxford Instruments dilution refrigerator. Although some of the measurements were enabled by hardware and software available with the cryostats, we created several key pieces of code and equipment, as outlined below.

1. Electrical transport

a) Four and five probe

The commercial cryostats that were used required us to mount our samples onto "pucks" that fit securely onto metal pins at the bottom of the sample chamber. The pins ensured electrical connection between the sample puck and commercial resistivity bridge, the output of which was read by a computer. The current and voltage for three measurement channels were read in a dc excitation mode, and measurements of $\rho(T)$ at each temperature and/or field were averaged after at least 25 readings in order to increase signal to noise.

In addition to electrical contact, it was necessary to confirm that the sample was in good thermal contact with the system thermometer. To ensure good thermal contact between the sample and the puck, samples were mounted onto the pucks using a thin layer of GE 7031 varnish on a small square of cigarette paper, a common experimental setup (Ekin 2006).

The basic $\rho(T)$ measurement consists of a four-wire setup, with two gold wires for measuring the voltage (V) and two for current (I). The four-wire setup is commonly used as a way to eliminate lead and contact resistance and therefore increase accuracy. Gold was used because it is a reliable conductor that is highly stable and resistant to corrosion (Song, Wang et al. 2012). Epo-Tek H20E silver epoxy was used to form mechanical and electrical contacts between the sample and wires due to its reliability and high thermal conductivity.

Five-probe configurations were used for our Hall measurements, as in figure 2.1. One edge of the sample has two V leads that are connected in series with a potentiometer that is used to adjust the zero-field V across the sample (due to the misalignment) to zero. This ensures that the V-difference measured in the presence of an applied H is due purely to the Hall effect and excludes longitudinally-generated voltages. Further precautions can be taken by subtracting any symmetric contributions after doing a sweep from $+H$ to $-H$, as the Hall effect should be purely antisymmetric in H.

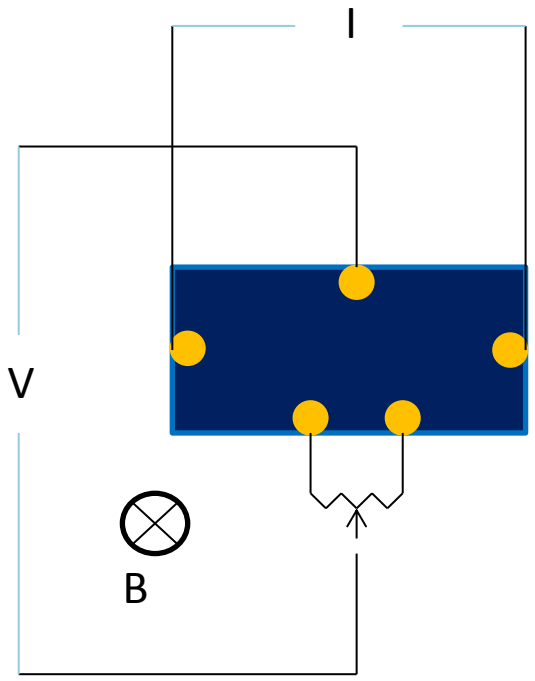


Figure 2.1: Five-probe configuration for Hall measurements.

b) Van der Pauw

The five probe configuration is suitable for samples with a proper Hall-bar shape, which is a rectangular parallelepiped with $l \gg w$. The Hall effect can be experimentally difficult to measure in samples of irregular shape. The van der Pauw (vdP) method is a modified Hall measurement that only requires four contacts and applies to flat samples of uniform thickness, with the thickness much smaller than the width of the sample. Additionally, the sample must be homogeneous and isotropic, with no holes. The vdP measurement can be performed on any sample shape, but a clover is ideal to reduce the error from contacts that may be large compared to the size of the sample (figure 2.3). The contact pads must be at least an order of

magnitude smaller than the sample, and on the edges of the sample in order to uphold the conformal equivalence of arbitrarily shaped lamella, the assumption under which the vdP equation (below) was derived (Webster 1999).

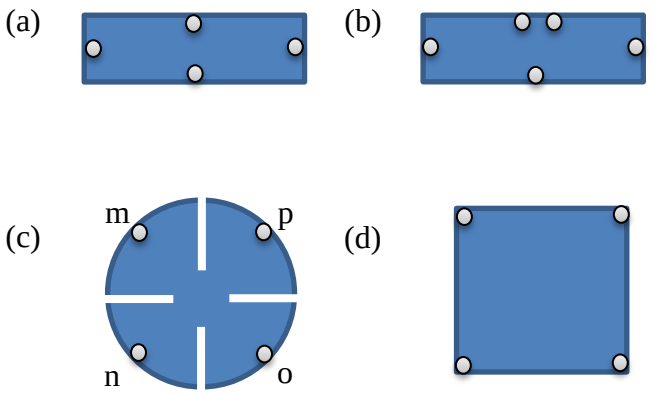


Figure 2.2: The (a) standard Hall, (b) five-probe Hall. (c) clover and (d) square van der Pauw configurations. The clover configuration contacts are labeled for reference in the discussion of the vdP measurement.

For a sample that meets the above criteria, one can measure the resistivity using the van der Pauw equation (Van der Pauw 1958),

$$e^{-\pi R_{MN,OP}/R_S} + e^{-\pi R_{NO,PM}/R_S} = 1, \tag{2.1}$$

where

$$R_{MN,OP} = \frac{V_P - V_O}{I_{MN}}, \tag{2.2}$$

with an analogous definition for $R_{NO,PM}$, and R_s is the sheet resistance, the quantity of interest.

Using the same sample contact configuration, the Hall coefficient can be measured as

$$R_H = \frac{d}{H}\Delta R_{MO,NP}, \tag{2.3}$$

where $\Delta R_{MO,NP}$ is defined as $R_{MO,NP} - R_{MO,NP}(H = 0)$. R_H can then be used to extract the carrier density and mobility, as usual. Thus, using the same four-wires, but with different combinations for I and V, one can easily extract both the resistivity and Hall coefficient. Although only a few $I - V$ combinations are needed, measuring the other equivalent combinations allows for error analysis on sample uniformity, anisotropy, differences in contact quality, etc.

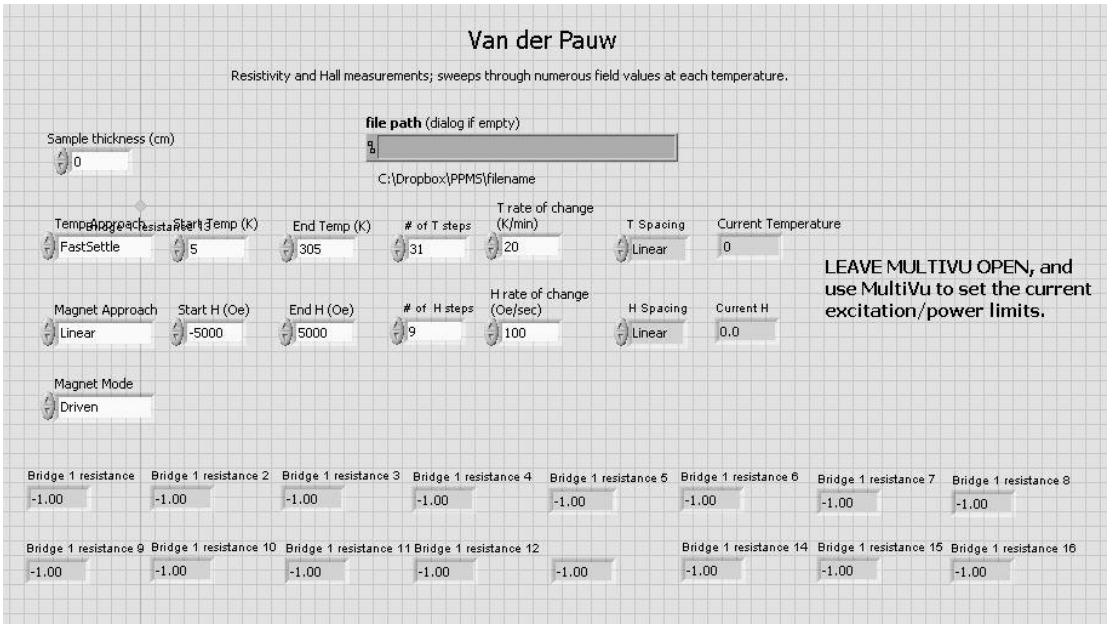


Figure 2.3: The van der Pauw program control window. The white background boxes indicate inputs, while the gray background boxes are outputs which display information about the measurement.

We automated the vdP measurement process by building a "vdP box" with 16 reed relay switches that were turned on and off by a 16-channel switchbox. Four reed relays were connected to one sample contact, thus allowing us to specify which contacts corresponded to $I+, I-, V+, V-$ for any single measurement. This process was automated through a *LabView* program (figure 2.3), which systematically measured all 16 possible $I-V$ configurations, then analyzed the resistivity and Hall coefficient. A screenshot of the *LabView* block diagram can be found in Appendix A.

2. Thermal transport

a) Thermopower

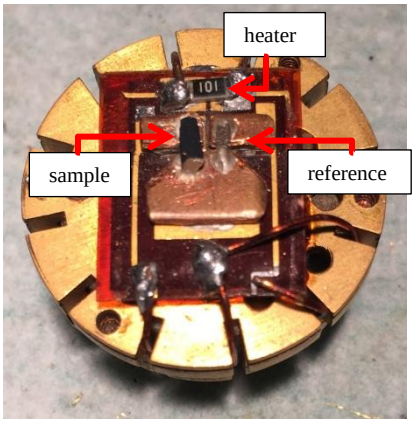


Figure 2.4: Sample puck used for thermopower measurements.

Our *S(T)* measurements made use of a standard PPMS transport puck, but with a customized Seebeck stage from MMR Technologies (figure 2.4). A Bi_2Te_3 reference standard was used (Lowhorn, Wong-Ng et al. 2011), while a 100 ohm

resistor served as a heat source. The computer code used to automate the measurement was based on a code previously written in Quick Basic, which we translated into a more modern form of Basic, Visual Basic 6.0, for the purpose of these measurements (figure 2.5, see Appendix B for code). The premise of the code is the comparative thermal bridge technique, described here:

1. Heat is supplied by means of the resistor while two multimeters read the voltage across both the sample and the reference. The amount of heat is specified via the code by the user
2. The multimeters continue to read the voltages until the voltages are constant, which indicates that the system has reached thermal equilibrium
3. The system then reads the voltage difference across the calibrated reference standard and calculates the temperature gradient, ΔT, based on a calibration table that is included in the code
4. After measuring ΔV across the sample, $S(T)$ for the sample is calculated as $\Delta V/\Delta T$
5. This process is repeated for two additional ΔT values, which are set by increasing the amount of heat supplied from the resistor, in order to ensure ohmic behavior. The temperature or field is then incremented (for $S(T, H)$) and the entire process repeated. Plots are updated to reflect the new data

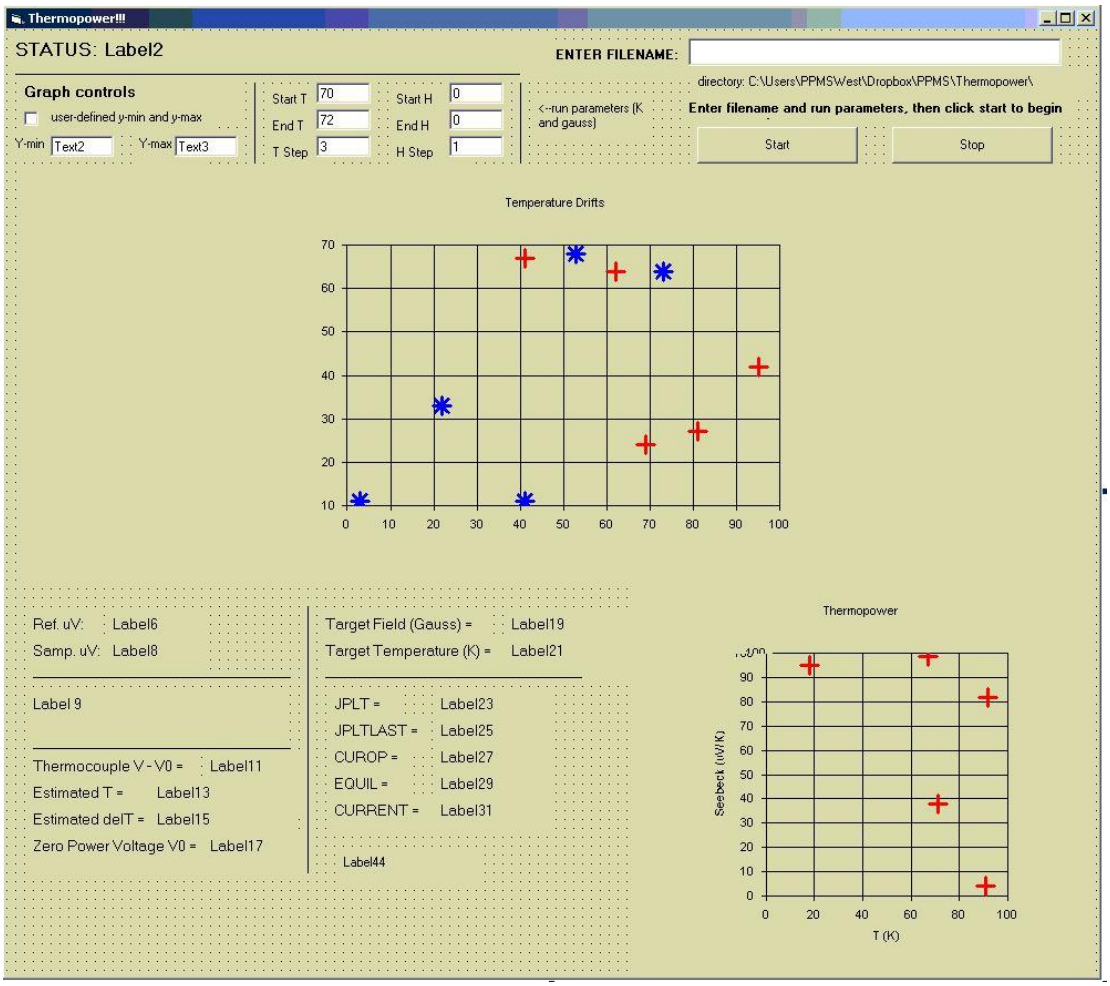


Figure 2.5: The Visual Basic 6 thermopower program control panel. The main plot window (center) displays the temperature drifts as a function of time for the sample and the reference, while thermopower data as a function of T are displayed in the plot window on the bottom right. The points on the plots in the figure are not actual data.

b) Specific heat

$C(T)$ from 2 K – 300 K was performed using a commercial Quantum Design Heat Capacity Option, but a custom $C(T)$ apparatus was prepared for use with the dilution refrigerator for temperatures down to 50 mK. A semi-adiabatic heat pulse

technique was used, meaning that, after ensuring that the sample is thermally equilibrated at a temperature T, a well-defined heat pulse of known power and duration is applied to the sample, which is then allowed to cool. The temperature of the sample as it cools is measured as a function of time, which allows for calculation of the average change in temperature of the sample, and therefore, of the specific heat (full description below). This process was automated for incrementing in field and in temperature so as to measure $C(T, H)$.

The computer code used to automate the measurement process was based on a previously written Quick Basic code that was translated to Visual Basic 6, much like the thermopower program (see Appendix C for main body of code). The control panel is seen in figure 2.5, where the center plot window displays the temperature drifts while the lower-right plot window displays the $C(T)$ data.

Each step in the measurement process requires great care, especially with regard to the temperature measurement. The sample chamber temperature is measured via a commercially-calibrated Germanium resistance thermometer, while the sample temperature is measured using a Phillips surface mount resistor, in which variable range hopping provides good temperature response below 1 K with low sensitivity to magnetic field. The thermometer and heater (manganin meander line) are bonded to a sapphire plate using Stycast 1266 epoxy for good thermal contact. Thermometer calibration tables are included in the measurement code, and are known

to high enough precision (along with better than ms time resolution) to accurately measure $C(T)$ to within 1%.

Upon starting the program, users are asked to input the amount of time to measure the temperature drift (drift length), the approximate amount of time for the sample to reach thermal equilibrium (internal time constant), current increment used to apply heat (current step), and duration of the heat pulse (heat length). The amount of heat is controlled through a heater box, which contains several resistors and reed relays that are turned on and off by a switchbox that is controlled by the program.

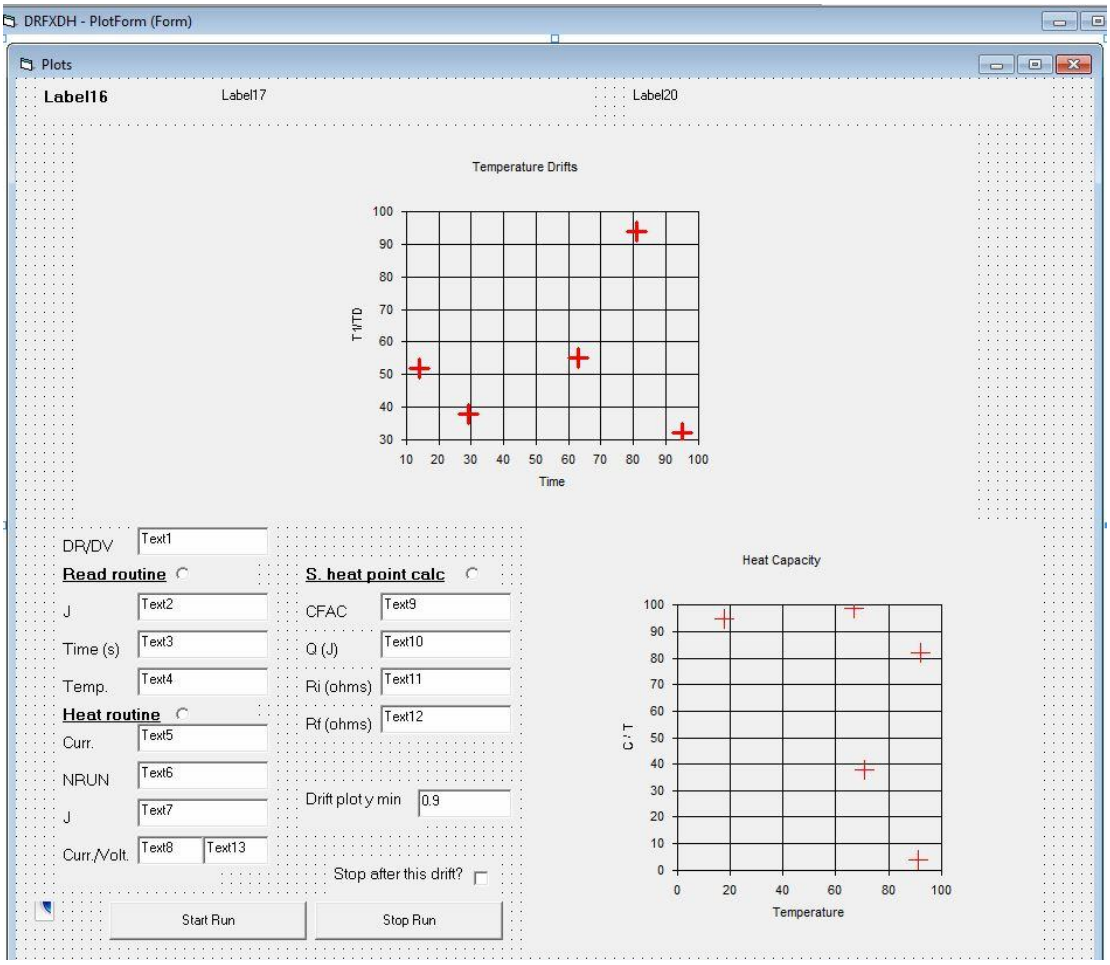


Figure 2.6: Control window for the dilution refrigerator specific heat program.

The measurement process is as follows:

1. The sample is cooled to a temperature T
2. When thermal equilibrium is achieved, a heat pulse is applied to the sample
3. After the heat pulse is applied, the sample is allowed to cool, and the temperature of the sample is measured as a function of time

4. The first two steps are repeated ten times so as to allow for averaging to reduce noise
5. Using the temperature drifts, slopes and intercepts as a function of time are calculated so as to ultimately calculate the average change in temperature. The specific heat is then given by $C(T) = Q/\Delta T$, where Q is the heat input
6. The temperature or field is then incremented, and the measurement process is repeated. Plots are updated to reflect the new data

For full details, the main body of code is included in Appendix C.

3. Magnetic susceptibility

Magnetic susceptibility (χ) was measured using a commercial Quantum Design Magnetic Properties Measurement System (MPMS). Samples were mounted in a plastic drinking straw, which was then attached to a probe rod and lowered into a measurement chamber. The MPMS raises the probe rod through a 6 cm (for example) length of the chamber in the presence of an applied H, then measures the response using a superconducting quantum interference device, or SQUID (Fagaly 2006), a sensitive voltmeter that is current-coupled to the field sensing coils.

In the experiments on URu2si2, we tested a theoretical prediction, which required us to measure M as a function of angle between H and the crystallographic

c-axis. To do this, we machined a set of Stycast 1266 epoxy wedges that range from $\theta = 0° - 90°$ in order to fix the alignment of our samples to within $\pm 2°$. Additional systematic uncertainty comes from bends in the straw and rod of order 1-2°. A measurement of the Stycast plugs revealed a negligible signal that was much smaller than the average magnetic signal from our samples.

Chapter III: Thermodynamic measurement of angular anisotropy at the hidden order transition of URu_2Si_2

1. *History of hidden order*

As introduced in Chapter 1, U compounds have been intensely studied for the past few decades due to their unconventional superconductivity and magnetism (Mydosh and Oppeneer 2011). The U-based intermetallics (as well as their Ce-based cousins) possess a strong coupling between itinerant s, p, or d electrons and localized f-electrons, an interaction termed *hybridization*, which leads to a shift of local moment spectral weight to the Fermi level, thus making the electrons "heavy." Among these heavy fermion compounds is URu_2Si_2, which exhibits two transitions: a superconducting transition at T_c = 1.0 K and a transition of unknown origin at T_{HO} = 17.5 K, where the "HO" will be made clear below. Thermodynamic measurements have shown features at T_{HO} typical of magnetic order, where a sharp peak in $C(T)$ ($\Delta C(T)$ ~ 250 mJ/mol-K^2 over ΔT~2.5 K at T_{HO}) coincides with a broad transition in the magnetization that is consistent with antiferromagnetic order (Palstra, Menovsky et al. 1985). However, neutron scattering experiments found only a small antiferromagnetic moment in the ordered phase, $(0.03 \pm 0.01)\mu_B$, which coexists with the superconducting phase below T_c (Broholm, Lin et al. 1991). The size of the moment is insufficient to account for the large change in entropy ($0.24R\ln 2$, where R is the molar gas constant) seen in the specific heat, $C(T)$ (Palstra, Menovsky et al. 1985). Thus, the exact form of the order parameter below T_{HO} has so-far eluded

description, despite numerous studies (nearly 1000 papers) devoted to this question (Harima, Miyake et al. 2010). Thus, this phase has been referred to as the *hidden order* (HO) phase.

Despite intensive theoretical and experimental efforts, the HO remains unidentified thirty years after its original discovery (Mydosh and Oppeneer 2011). The nature of the quasiparticle excitations and the broken symmetries associated with the HO phase are important questions for understanding not only HO but also the low-temperature exotic superconductivity. While URu_2Si_2 is tetragonal above the HO, torque magnetometry (Okazaki, Shibauchi et al. 2011), cyclotron resonance (Tonegawa, Hashimoto et al. 2012), x-ray diffraction (Tonegawa, Kasahara et al. 2014) and elastoresistivity measurements (Riggs, Shapiro et al. 2015) indicate fourfold symmetry-breaking in the basal plane. However nuclear magnetic resonance and nuclear quadrupole resonance studies suggest that this nematic signal decreases with increasing sample size and also depends on sample quality, suggesting that the bulk is tetragonal (Mito, Hattori et al. 2013, Kambe, Tokunaga et al. 2015).

A number of measurements on URu_2Si_2 indicate Ising anisotropy, suggesting that it is essential to understanding its HO. At the HO transition temperature, T_c, both the linear (χ_1) and nonlinear (χ_3) susceptibilities are anisotropic, with χ_3 displaying a sharp anomaly $\Delta\chi_3 = \chi_3({T_c}^-) - \chi_3({T_c}^+)$ that tracks closely with the structure of the specific heat (Miyako, Kawarazaki et al. 1991, Ramirez, Coleman et al. 1992). The non-spinflip ($\Delta J_z = 0$) magnetic excitations seen in both inelastic neutron scattering (Broholm, Lin et al. 1991) and in Raman measurements (Buhot, Measson et al. 2014)

also have Ising character, despite the absence of local moments at those temperatures and pressures. Finally, quantum oscillations measured deep within the HO region indicate a quasiparticle g-factor with strong Ising anisotropy, $g(\theta) \propto \cos(\theta)$, where θ is the angle away from the c-axis (Ohkuni, Inada et al. 1999, Altarawneh, Harrison et al. 2011). This $g(\theta)$ is confirmed by upper critical field experiments (Altarawneh, Harrison et al. 2012), that indicate that Ising quasiparticles pair to form a Pauli-limited superconductor. Below we present a *bulk thermodynamic measurement* of the Ising nature of the hidden order parameter, which shows that this Ising anisotropy is present not only deep inside the HO, but at the transition itself; it is even present in the order parameter fluctuations above T_c.

2. Hastatic order

The basis for our measurements comes from a model for the large Ising anisotropy in URu_2Si_2 called *hastatic order*, after the Latin *hasta*, meaning *spear* (Chandra, Coleman et al. 2013, Chandra, Coleman et al. 2015). In the hastatic order picture, Ising quasiparticles are formed through hybridization between conduction electrons (half integer spin) and Ising $5f^2$ states (integer spin), a non-Kramers doublet that couples only to the z-component of the field. The hybridized quasiparticles thus inherit the Ising character of the $5f^2$ states, leading to the experimental anisotropy. This phase can be described by a spinor order parameter, ψ, that breaks double time-reversal symmetry, meaning that the magnetic order seen in URu_2Si_2 is distinct from

ordinary magnetism, wherein only single time-reversal symmetry is broken (Chandra, Coleman et al. 2013).

Within Landau theory formalism, hastatic order gives rise to several predictions. One prediction from this model is that the nonlinear susceptibility anomaly, $\Delta\chi_3$, should exhibit a colossal Ising anisotropy and behave as $\Delta\chi_3 \propto \cos^4\theta$ (Chandra, Coleman et al. 2013). We test this prediction below.

3. Angular anisotropy measurement

As a rank-4 tensor, the nonlinear susceptibility χ_{3abcd},

$$M^a = \chi_{1ab}H^b + \frac{1}{3!}\chi_{3abcd}H^bH^cH^d \tag{3.1}$$

is particularly well-suited to probe symmetry-allowed anisotropies in the tetragonal crystal environment (space group I4/mmm) of URu_2Si_2; here M and H refer to the magnetization and the applied magnetic field respectively, and we use a summation convention for repeated indices. We present an angular survey of the HO transition, reporting an extensive series of nonlinear susceptibility ($\chi_3(\theta,\phi)$) measurements. Our results have important implications for the nature of the quasiparticles in the HO phase, and we also use $\chi_3(\theta,\phi)$ to probe the angular anisotropy of short-range order parameter fluctuations at temperatures above the HO transition.

The general expression for the field-dependent part of the free energy in a tetragonal crystal at fixed temperature is

$$F = -\chi_1(\theta)\frac{H^2}{2} - \chi_3(\theta,\phi)\frac{H^4}{4} \tag{3.2}$$

with

$$\chi_1(\theta) = \chi_1^a + \chi_1^b \cos^2\theta \tag{3.3}$$

and

$$\chi_3(\theta,\phi) = \chi_3^a + \chi_3^b \cos^2\theta + \chi_3^c \cos^4\theta + \chi_3^d \sin^4\theta \sin^2 2\phi, \tag{3.4}$$

where θ and ϕ refer to the angles away from the c-axis and in the basal plane respectively. The anomaly in $\Delta\chi_3$ is a known signature of HO (Ramirez, Siegrist et al. 1991). Because there is no Van Vleck contribution to the anomaly $\Delta\chi_3$, it is a direct thermodynamic probe of the g-factor at the HO transition. A key question is whether the anisotropic g-factor found in quantum oscillations persists to higher temperatures in the hidden order phase. Consistency with the low temperature $g(\theta) \propto \cos(\theta)$ results requires a large change in χ_3^c, $\Delta\chi_3^c$, and negligible $\Delta\chi_3^a$ and $\Delta\chi_3^b$.

The URu_2Si_2 crystal used in this study is of dimension 4 mm × 2.5 mm × 2 mm and has been previously described (Ramirez, Siegrist et al. 1991, Ramirez, Coleman et al. 1992). A recent measurement of $C(T)$ as well as the χ_1 and χ_3 measurements reported here show no change in these properties over time (Ramirez, Coleman et al. 1992). The narrow width of the specific heat transition, $\Delta T_{HO} = 0.35$ K is consistent with high quality samples of comparable dimensions (Matsuda, Hassinger et al. 2011, Kambe, Tokunaga et al. 2013, Niklowitz, Dunsiger et al. 2015). Additionally, the single superconducting transition indicates a single phase (Ramirez, Siegrist et al. 1991) confirming the high quality of the sample. Measurements of the

magnetization, M, were performed in a commercial superconducting quantum interference device (SQUID) magnetometer, as a function of temperature (T), magnetic field (H), and angle (θ) between the sample's c-axis and H. The variation in angle was achieved with a set of sample mounts machined from Stycast 1266 epoxy (figure 3.1). The linear and leading nonlinear (χ_3) susceptibilities were determined as in (Ramirez, Coleman et al. 1992). Multiple measurements (~1800 $M(H)$ scans) were performed with sufficient resolution in H, T and θ to resolve the angular dependence of the χ_3 discontinuity at T_c. Values for χ_3 were obtained at every θ using a straight-line construction assuming a mean-field jump at T_c.

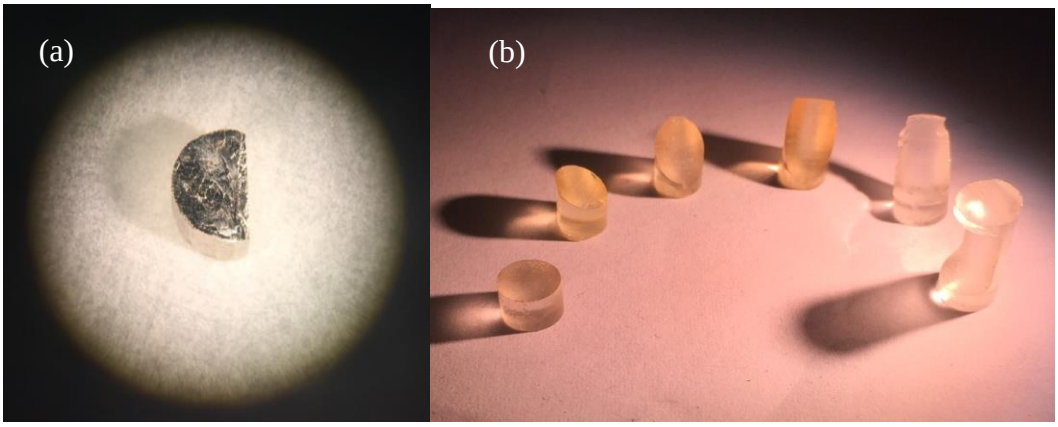


Figure 3.1: (a)The URu_2Si_2 sample used in this study. The c-axis is perpendicular to the upwards-facing plane. (b) 6 of the 19 Stycast wedges used for the angular variation between the sample's c-axis and H.

4. Results and discussion

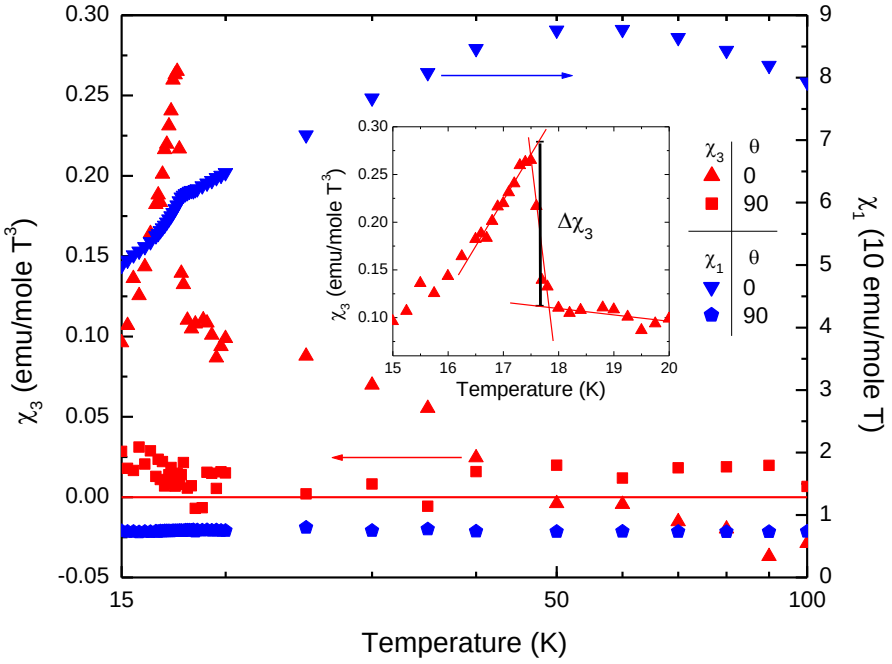


Figure 3.2: Linear and nonlinear susceptibility versus temperature for fields along the c-axis ($\theta = 0°$) and in the basal plane ($\theta = 90°$).

Figure 3.2 shows $\chi_1(T)$ and $\chi_3(T)$ as a function of temperature at $\theta = 0^{\circ}$ and 90°, data that agree well with previous reports (Ramirez, Coleman et al. 1992). We note that the nonlinear susceptibility displays a sharp anomaly at the HO transition, whereas $\chi_1(T)$ displays a corresponding discontinuity in its gradient $d\chi_1(T)/dT$; both $\chi_1(T)$ and $\chi_3(T)$ are significantly larger for $\theta = 0°$ (c-axis) than for $\theta = 90°$ (ab plane).

In figure 3.3 we show the angular dependence of $\Delta\chi_3$ and χ_1 at and just above the HO transition. The linear susceptibility displayed in figure 3.3 is characterized by the form

$$\chi_1(\theta, T) = \chi_1^{(0)} + \chi_1^{Ising}(T)\cos^2\theta, \tag{3.5}$$

where the isotropic component $\chi_1^{(0)}$ of the susceptibility displays no discernable temperature dependence. The temperature-dependent Ising component and $d\chi_1^{Ising}/dT$ displays a discontinuity at the HO transition. Whereas $\chi_1(\theta)$ varies as $\cos^2\theta$ at T = 18 K, in figure 3.3 the sharp jump in χ_3 at the transition, $\Delta\chi_3$, has a distinctive $\cos^4\theta$ dependence

$$\Delta\chi_3(\theta,\phi) = \Delta\chi_3^{Ising}\cos^4\theta \tag{3.6}$$

without any constant (Van Vleck) terms; this then indicates that $\Delta\chi_3^c \gg \Delta\chi_3^b, \Delta\chi_3^c$ in (equation 3.4) consistent with the low-temperature $g(\theta)$ measurements. We note that, within experimental resolution, no χ_3^d component was observed in the measurements, either above or at the transition.

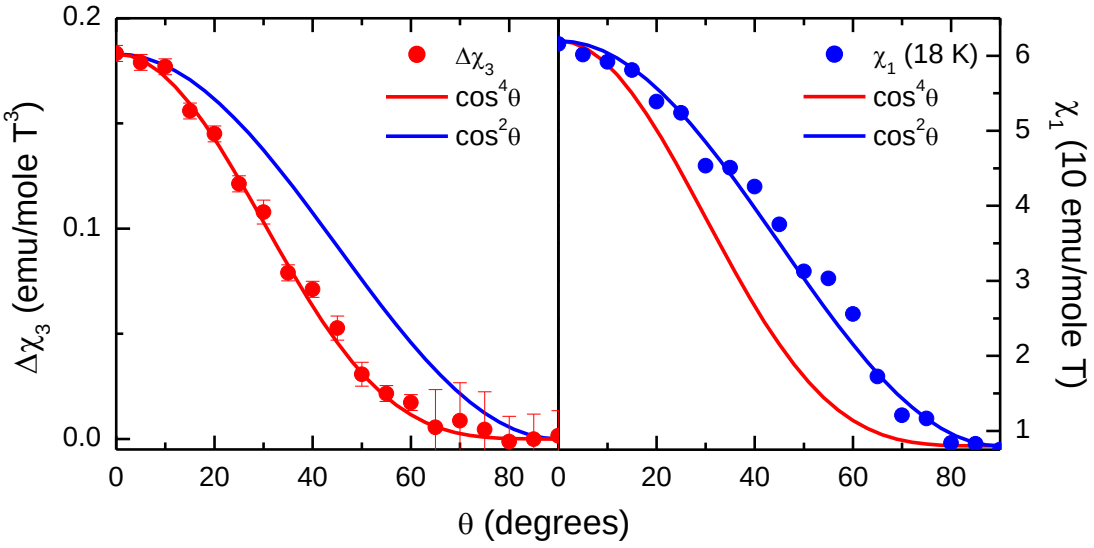


Figure 3.3: Angular dependence of (a) the jump $\Delta\chi_3 3$ in the nonlinear susceptibility at the hidden order transition and (b) the magnetic susceptibility just above the hidden order transition at 18 K.

In figure 3.4 we compare the angular dependences of $\Delta\chi_3$ with $\chi_3(18\ K)$, $\chi_3(30\ K)$ and $\chi_3(100\ K)$, just above, moderately above and well above T_c. At 18 K and 30 K, χ_3 follows $\cos^4\theta$, similar to $\Delta\chi_3$. At 100 K, the positive contribution to χ_3 associated with the HO transition has completely vanished, leaving a negative response presumably associated with single-ion dipolar physics; the signal is too small to resolve the anisotropy. At T = 18 K, χ_3 is about 1.6 times smaller than $\Delta\chi_3$, (c.f. fig. 3.2), and is well described by the form

$$\chi_3(\theta, T) = \chi_3^{(0)} + \chi_3^{Ising}(T)\cos^4\theta, \tag{3.7}$$

where the isotropic component $\chi_3^{(0)}$ is essentially temperature-independent. A $\cos^4\theta$ dependence in $\chi_3(T)$ is still observed at 30 K, and by comparing the c-axis and basal plane measurements, we estimate that around T = 60 K, $\chi_3^{Ising}(T)$ goes to zero (see fig. 3.2). Above 100 K, the $\cos^4\theta$ dependence is no longer discernable, leading us to infer that the Ising component to the non-linear susceptibility vanishes around 60 K.

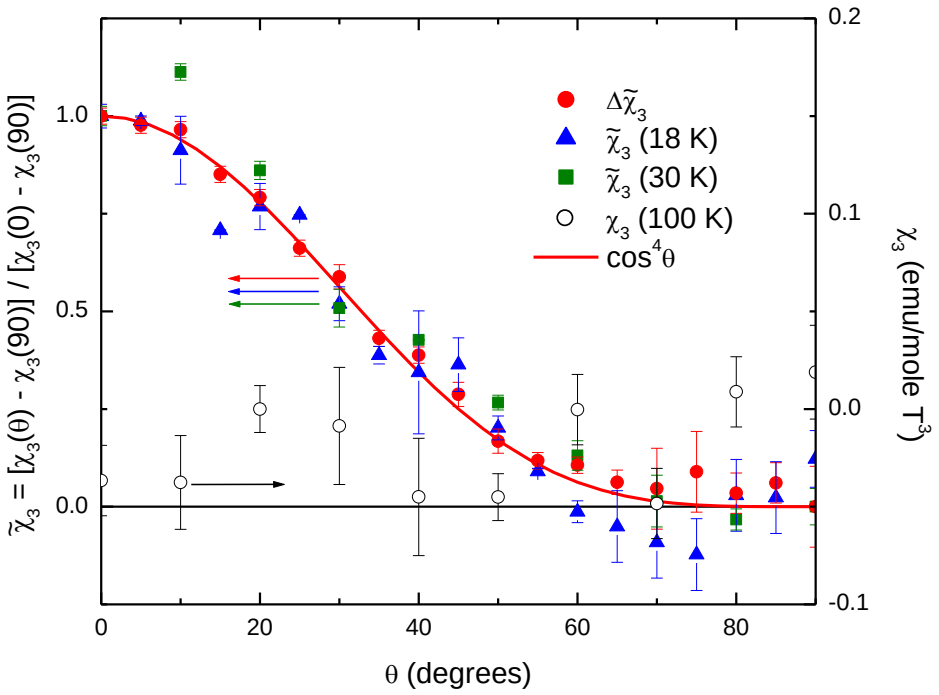


Figure 3.4: Angular dependence of $\Delta\chi_3$ and χ_3 at three different temperatures, showing the disappearance of the Ising behavior at high temperatures.

At the HO transition, our results can be analyzed within a minimal Landau free energy density of the form

$$f(T,\psi) = a\big(T - T_c(H)\big)\psi^2 + \frac{b}{2}\psi^4 \tag{3.8}$$

where we describe a domain of hidden order by a real order parameter ψ and

$$T_c(H) = T_c - \frac{1}{2}Q_{ab}H_aH_b + O(H^4) \tag{3.9}$$

defines the leading field-dependent anisotropy in the transition temperature, where Q_{ab} is a tensor capturing how the order parameter couples to the magnetic field. The quantity $\Delta\chi_{ab} = -aQ_{ab}\psi^2$ is the magnetic susceptibility associated with the hidden order. By minimizing the free energy with respect to ψ, the free energy below

T_c is then $f(T) = -(a^2/2b)[T_c(H) - T]^2$. The jump in the linear and nonlinear susceptibilities are then given by

$$\left(\Delta \frac{d\chi_1}{dT}\right)_{ab} = -\frac{a^2}{b} Q_{ab} \text{ and}$$

$$(\Delta\chi_3)_{abcd} = \frac{4a^2}{b}(Q_{ab}Q_{cd} + Q_{ac}Q_{bd} + Q_{ad}Q_{cb}). \quad (3.10)$$

In order to determine the robustness of the Ising anisotropy, by setting $Q_{xx} = Q_{yy} = \Phi Q_{zz}$, we codify our results in terms of an angle-dependent coupling between the hidden order parameter ψ and the magnetic field of the form

$$\Delta f[\psi, \theta] = -aQ_{zz}\psi^2 H^2(\cos^2\theta + \Phi\sin^2\theta)^2, \quad (3.11)$$

where Φ quantifies the fidelity of the Ising-like behavior, so that Φ = 0 and Φ = 1 correspond to Ising and isotropic behavior respectively. The corresponding jump in the nonlinear susceptibility at T_c is

$$\Delta\chi_3(\theta) \propto (\cos^2\theta + \Phi\sin^2\theta)^2. \quad (3.12)$$

Assuming a fit of this form for $\Delta\chi_3(\theta)$, we determined Φ by optimizing the goodness of fit, or by minimizing the reduced χ^2 of the fit, which is defined as

$$\chi^2_{red} = \sum_{i=1}^{n} \frac{\sigma^{-2}(\Delta\chi_{3meas}(\theta_i) - \Delta\chi_{3fit}(\theta_i))^2}{n-m}. \quad (3.13)$$

Here σ^2 is the variance, n is the number of data points and m is the number of fit parameters, which in this case is 1 since Φ is manually adjusted. Weighting against the variance allows us to incorporate the error in each $\Delta\chi_3$ measurement in our fit, while dividing by $n - m$ normalizes for the degrees of freedom. The reduced χ^2 was calculated for several values of Φ, and the results are shown in the

inset of fig. 3.5, where the minimum as determined by a quadratic fit is Φ = 0.036 ± 0.021.

The intent behind using the reduced χ^2 is not to determine the goodness of fit relative to other models, but to extract an estimate for Φ and its error given the model that we propose. Thus, it is the robustness of the *minimum* of the reduced χ^2 that we require, not its absolute value. To ensure that our value of Φ is insensitive to random error, we have examined the effect of masking various points. The removal of any one point from the data set resulted in a change in Φ of ± 0.0013 on average, less than our uncertainty in Φ of 0.021. Additionally, we compared our results with a similar analysis using other measures for goodness of fit (e.g., R^2) and found Φ-values within ± 0.0006 of 0.036, which is again within our error estimate.

Such a small value of $\Phi = 0.036 \pm 0.021$ could be accounted for by an angular offset of only one degree, via equation 3.12. X-day diffraction orientation measurements indicate an uncertainty in the c-axis of our sample of no more than $\pm 3°$. In figure 3.5, one can see that this value provides upper and lower bounds to the $\cos^4\theta$-dependence of $\Delta\chi_3$ that bracket the data symmetrically. Thus, a Φ value of 0.036 is well below the total uncertainty of the measurement. To reduce the uncertainty in Φ even further would require angular accuracy of well below 1°, which is beyond the capability of the present apparatus. Thus, the obtained Φ = 0.036 is consistent also with Φ = 0.

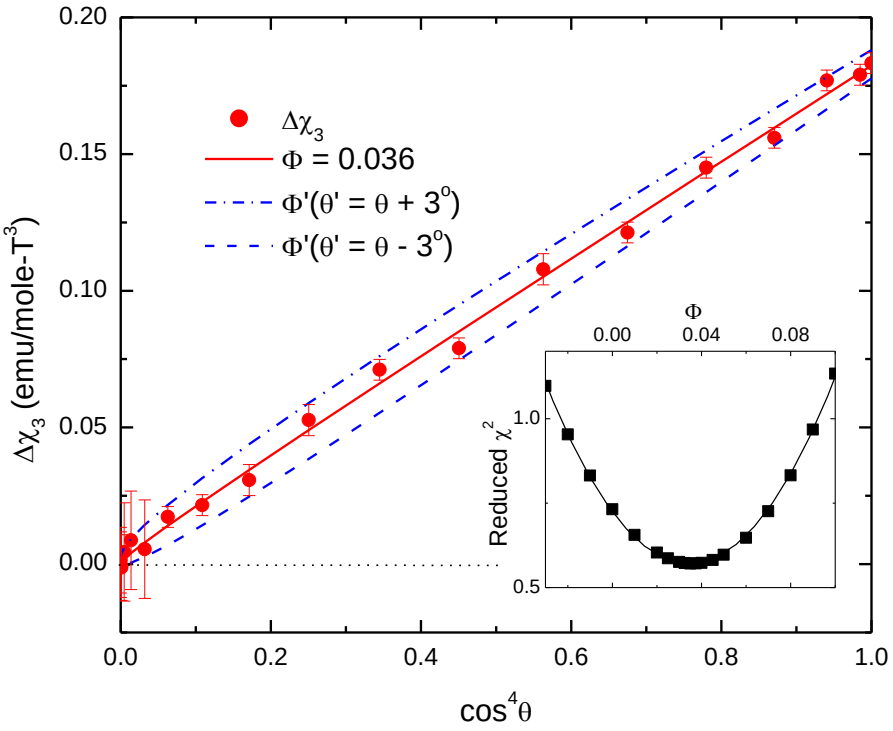


Figure 3.5: $\Delta\chi_3$ as a function of $\cos^4\theta$, fit to equation 3.12 for different values of Φ. Blue dashed lines indicate Φ-values assuming an angular offset of 3° ($\theta' = \theta \pm 3°$). Inset shows the effect of Φ on the goodness of fit, expressed as the reduced χ^2.

We now discuss the implications of these results. At the very simplest level, our results show that the free energy of URu_2Si_2 only depends on the z component of the magnetic field, i.e. $F\left[\vec{H}\right] = F[H_z]$. In particular:

- The coupling of the order parameter to the magnetic field involves an Ising coupling $F[H,\psi] = -Q_{zz}\psi^2 H_z^2$ coupling.
- In the microscopic Hamiltonian, the Zeeman coupling of the magnetic field is strongly Ising, with the field coupling to the z-component of the total angular momentum $-J_z B_z$.

The second point follows because derivatives of the free energy with respect to field are equivalent, inside the trace of the partition function, to the magnetization operator $-\delta/\delta H_z \equiv \widehat{M}_z$, so that if the free energy only depends on H_z, the partition function $Z = \mathrm{Tr} e^{-\beta H}$ and hence the Hamiltonian only depends on $\widehat{M}_z = g\hat{J}_z$.

However, these simple conclusions have implications for the microscopic physics. On the one hand, we can link the Ising anisotropy of the microscopic Hamiltonian to the single-ion properties of the U ions in URu_2Si_2, where the Zeeman coupling $-g_f \mu_B J_z B_z$ is a sign of vanishing matrix elements $\langle + | J_{\pm} | - \rangle = 0$. From a single-ion standpoint, an almost perfect Ising anisotropy is a strong indication of an integer spin $5f^2$ U^{4+} ground state with $J = 4$. High-spin Ising configurations of the alternative $5f^3$ U^{3+} ionic configurations are ruled out because the coupling of the local moment to the tetragonal environment mixes configurations by adding angular momenta in units of $\pm 4\hbar$, for example $J_z = \pm 5/2$ and $\mp 3/2$, leading almost inevitably to a non-zero transverse Zeeman coupling when the angular momentum J is half integer. Although the precise crystal-field configuration of the U ions is still uncertain, both dynamical mean-field calculations (Haule and Kotliar 2009) and high-resolution RIXS measurements (Wray, Denlinger et al. 2015) confirm the predominantly $5f^2$ picture.

Yet a single-ion picture is not enough, for the sharpness of the specific-heat anomaly, the sizable entropy and the gapping of two-thirds of the Fermi surface associated with the hidden order transition (Mydosh and Oppeneer 2011) all suggest

an underlying itinerant ordering process. The remarkable feature of our data is that the jump $\Delta\chi_3$ that reflects the itinerant ordering process exhibits a strong Ising anisotropy. This result links in with the observation of multiple spin zeroes in dHvA measurements, which detect the presence of itinerant heavy quasiparticles with an Ising g-factor $g(\theta) = g_f \cos\theta$ at low temperatures. Our new results suggest that these same quasiparticles survive all the way up to the hidden order transition. In the Landau theory, we can identify the Ising-like coupling between HO and the magnetic field in terms of the squared g-factor $Q_{zz}\psi^2\cos^2\theta \propto g(\theta)^2\psi^2$.

Reconciling the single-ion and itinerant perspectives, both supported strongly by experiment, poses a fascinating paradox. The simplest possibility is that the Ising anisotropy of the f-electrons is a one-electron effect resulting from a renormalized, spin-orbit coupled f-band that develops at temperatures well above the hidden order transition. In this purely itinerant view, the hidden order is a multipolar density wave that develops within a pre-formed band of Ising quasiparticles (Ikeda, Suzuki et al. 2012, Rau and Kee 2012). Microscopically such quasiparticles are renormalized one particle f-orbitals formed from high-spin orbitals with half-integer $|J_z|$. Provided only one $|J_z| > 1/2$ is involved, the transverse matrix elements of the angular momentum operator $\langle \pm | J_{\pm} | \pm \rangle = 0$ identically vanish, leading to a perfect Ising anisotropy. Such Ising quasiparticles have been observed in strong spin-orbit coupled systems, but only at high symmetry points in the Brillouin zone (Saito, Nakamura et al. 2016). Moreover, in a tetragonal environment, when an electron resonantly scatters off an f-state, J_z is only conserved mod(4). Thus a mobile heavy Bloch wave must actively

exchange $\pm 4\hbar$ units of angular momentum as it propagates through the lattice, leading to Bloch states composed of a mixture of J_z states, such as

$$|\boldsymbol{k} \pm\rangle = \alpha|\boldsymbol{k}, \pm 5/2\rangle + \beta|\boldsymbol{k}, \mp 3/2\rangle. \tag{3.14}$$

This inevitably gives rise to a finite transverse coupling and a finite Φ in the phenomenological Landau theory, ($\Phi \propto |\alpha\beta|^2$) that is ruled out by these experiments.

An alternative is that the itinerant f-quasiparticles carry integer angular momentum, inheriting the Ising anisotropy of a localized $5f^2$ local moment of the U atoms via a phase transition rather than a crossover. In this scenario, even though J_z is conserved mod(4), Ising anisotropy is preserved since the up-spin and down-spin configurations differ by at least two units of angular momentum. However, this picture requires that the half-integer conduction electrons hybridize with the underlying integer f-states, which can only occur in the presence of a spinorial or "hastatic" order parameter (Chandra, Coleman et al. 2013, Chandra, Coleman et al. 2014, Flint, Chandra et al. 2014, Chandra, Coleman et al. 2015). Indeed, the hastatic order scenario predicted the observed $\Delta\chi_3 \propto \cos^4\theta$ observed in this experiment, although theoretical efforts to develop a microscopic theory of hastatic order predicted a small transverse moment that has been shown to be absent in high-precision neutron scattering experiments (Das, Baumbach et al. 2013, Metoki, Sakai et al. 2013, Ross, Harriger et al. 2014). The vanishing of the anisotropy constant ($\Phi = 0$) in our nonlinear susceptibility measurements combined with the null result

reported by neutron scattering represents a fascinating challenge to our future understanding of hidden order.

The continuation of the Ising anisotropy well above T_c is also remarkable. While single-ion physics can give a negative Ising anisotropic χ_3, for an isolated Ising ground state doublet, or a positive, but more isotropic χ_3, if there are several singlets in the temperature range of interest, there is no way to explain the positive Ising anisotropic χ_3 emerging below 60 K with single-ion physics. Instead, this response indicates Ising anisotropic order parameter fluctuations extending up to more than three times T_c, an extraordinarily large fluctuation regime.

An interesting question raised by our work is whether bulk nonlinear susceptibility measurements can be used to detect microscopic broken tetragonal symmetry that has been reported in torque magnetometry measurements (Okazaki, Shibauchi et al. 2011). In principle, were the hidden order to possess domains with broken tetragonal symmetry, inter-domain fluctuations in the basal-plane susceptibility would manifest themselves through a finite value of χ_3^d below T_c. The large Ising anisotropy suppresses the precision for in-plane susceptibility measurement: our current work places an upper bound on the microscopic symmetry-breaking susceptibility $|\Delta\chi_{xy}|$ such that $|\Delta\chi_{xy}|/\chi_{xx} \leq 1$ that is two orders of magnitude larger than that measured by torque magnetometry on μm size samples (Okazaki, Shibauchi et al. 2011), and thus our results are completely consistent with their finding. However improvement in resolution in future measurements could make it possible to address this issue.

In summary, we have presented a detailed survey of the nonlinear magnetic susceptibility as a function of angle and temperature in the hidden order compound URu_2Si_2. These measurements showcase the unique Ising anisotropy, and imply that it is a key feature of the hidden order parameter. While previous quantum oscillation measurements indicated the presence of Ising quasiparticles, this Ising anisotropy persists not only to the transition temperature, but all the way up to 60 K, putting serious constraints on the theory of hidden order.

Chapter IV: Anomalous thermopower-mobility proportionality in $FeSb_2$

1. Introduction to $FeSb_2$

The narrow band-gap semiconductor $FeSb_2$ has many remarkable properties, the most notably a "colossal" thermopower ($S(T)$), the absolute magnitude of which can reach $S_{max} \equiv |S(T_{\max})|$ = 45 mV/K (Bentien, Johnsen et al. 2007). Given a high carrier mobility ($\mu(T)$) (Hu, Mitrovic et al. 2008, Takahashi, Okazaki et al. 2011), the resistivity is relatively low, thus resulting in a record power factor of ~8000 $\mu W/K^{-2}cm^{-1}$ (Jie, Hu et al. 2012). These properties have incited much interest in $FeSb_2$ as a candidate material for cryogenic thermoelectric applications, but the thermal conductivity, κ, is much too high to yield an appropriate figure of merit, $ZT = (S^2\sigma/\kappa)T$ (Bentien, Johnsen et al. 2007). Thus, while $FeSb_2$ itself is not currently suitable for cryogenic thermoelectrics, researchers hope to uncover the origin behind the large $S(T)$ in order to find or engineer other candidate materials.

While a significant effort has been made to understand the large $S(T)$ and the charge carrier dynamics in this system, important questions remain, such as the precise source of the magnitude of $S(T)$, the origin of the observed linear magnetoresistance (LMR), and the interrelationship of the transport coefficients. In our efforts to understand the underlying mechanisms governing the charge transport in this system, we have uncovered an unexpected relationship between $S(T)$ and the Hall mobility, $\mu_H(T)$. In both our own results as well as in data published from

previous studies, we find a proportionality between $S(T)$ and $\mu_H(T)$ that, to our knowledge, is unique to this system. Further, the *inverse* of this relationship is explicitly included in Herring's phonon drag model (Herring 1954), which has been suggested as a basis for understanding the large $S(T)$ in $FeSb_2$ (Takahashi, Okazaki et al. 2011, Battiato, Tomczak et al. 2015). Therefore, our finding casts doubt on a simple phonon drag picture. Additionally, the magnetoresistance, $\Delta\rho/\rho_0(T)$, features a linear contribution that also tracks $S(T)$ and $\mu_H(T)$. With these intriguing correlations among diverse properties, $FeSb_2$ provides a testing ground for the understanding of transport in small band gap semiconductors.

2. Experimental setup

High-quality single crystals of $FeSb_2$ were grown via a self-flux method from mixtures of the pure elements Fe (powder, >99.99%) and Sb (rod, >99.99%), with a molar Fe:Sb ratio of 1:10. The reactants were loaded into a quartz tube, after which a few pieces of broken quartz and quartz wool were loaded on top of the reactants as a filter for removing the excess Sb by centrifuging. The quartz tube was sealed under vacuum and heated in a furnace using the following sequence: heated to 1000 °C in 10 hours from room temperature, held at 1000 °C for 20 hours, then cooled to 740 °C in 2 hours, slowly cooled to 710 °C in 10 hours, then heated again to 725 °C in 2 hours, followed by slow cooling to 650 °C in 150 hours, and held at this temperature for centrifuging. For comparison, additional crystals were grown using chemical

vapor phase transport (CVT), with chlorine or iodine as the transport agent. For these crystals, growth was achieved in a temperature gradient from 700°C to 650°C; these temperatures prevent dissociation into competing phases and, at the cold end, prevent condensation of Sb. Although the data for the CVT samples are not shown, they exhibit the same qualitative resistivity, $\rho(T)$, as the flux-grown samples.

All transport properties in this work were determined along the crystallographic c-axis of the marcasite structure. Measurements of $S(T)$, $\rho(T)$, $\Delta\rho/\rho_0(T,H)$, and the Hall coefficient, $R_H(T)$, were performed in a commercial cryostat, and $S(T)$ was obtained using a comparative thermal bridge technique with a NIST sample of Bi_2Te_3 as the reference standard (Lowhorn, Wong-Ng et al. 2011). Silver epoxy was used for voltage/current contacts and for mounting samples onto the Seebeck stage.

3. Results and discussion

As shown in figure 4.1, $\rho(T)$ increases by over four orders of magnitude from 300 K to 2 K, which is indicative of a well-formed, but narrow, semiconducting gap. As in previous studies, two low-temperature "shoulders" emerge: one between 10 K and 30 K, and a second below 7 K (Petrovic, Kim et al. 2003, Bentien, Johnsen et al. 2007, Sun, Oeschler et al. 2009, Sun, Oeschler et al. 2009, Sun, Oeschler et al. 2010, Sun, Sondergaard et al. 2011, Takahashi, Okazaki et al. 2011, Takahashi, Yasui et al.

2011, Sun, Xu et al. 2013, Takahashi, Okazaki et al. 2013), each possibly due to exhaustion and impurity band conduction, respectively (Shklovskiĭ and Ėfros 1984). The exhaustion regime, however, should be signaled by a plateau in the carrier concentration, n, which we do not see, thus suggesting that the higher temperature shoulder in $\rho(T)$ is a result of a strongly temperature-dependent $\mu(T)$. Above and below the higher-T shoulder, one can extract an approximate value for the energy band gap, E_g, by assuming a thermally activated resistivity, $\rho(T) = \rho_0 \exp(-\Delta/k_B T)$, where ρ_0 is a constant, Δ is the activation energy, and k_B is the Boltzmann constant. For intrinsic semiconductors, $\Delta \sim E_g/2$. Thus, the Arrhenius plot shown in inset (a) of figure 4.1 yields $E_g$values of 27.9(2) meV for T > 30 K and 5.87(7) meV for 6 K > T > 10 K, which agree well with band gaps similarly extracted from previous studies (Bentien, Johnsen et al. 2007, Takahashi, Okazaki et al. 2011).

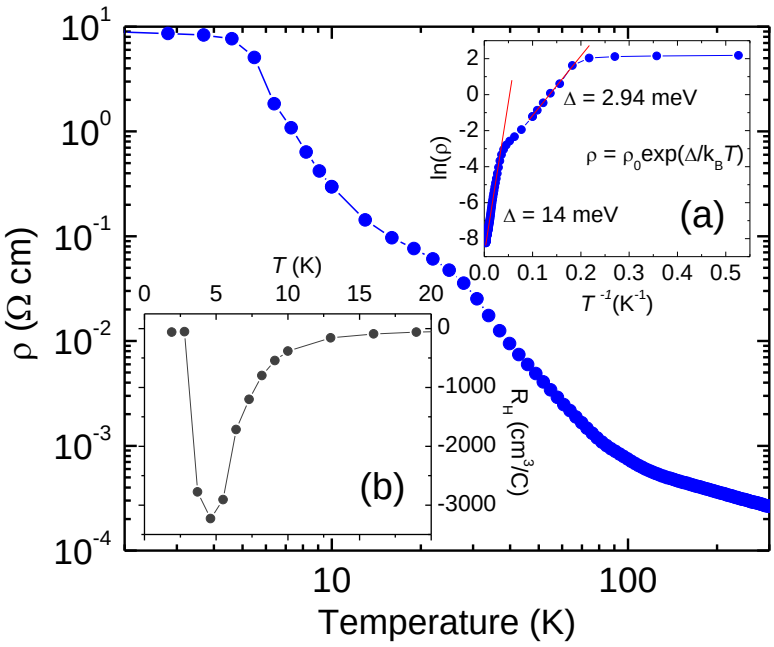


Figure 4.1: Electrical resistivity ($\rho(T)$) as a function of temperature. Inset a) shows the Arrhenius plot while inset b) displays the Hall coefficient for $FeSb_2$. $R_H(T)$ was extracted from the high-field (3 T – 6 T) slope of $\rho_{xy}(H)$.

The high-field (H > 3 T) slope of $\rho_{xy}(H)$ (figure 4.2) was used to determine $R_H(T)$. The sign of $R_H(T)$ (figure 1, inset (b)) indicates n-type carriers in the intermediate temperature region (ITR: 7 K – 40 K), consistent with the sign of S. Using a single carrier model with $R_H = 1/ne$, we find that $n \sim 10^{16}$ cm^{-3} around 10 K, and that $\mu_H(T)$ (inset of figure 4.2) rapidly increases from less than 20 cm^2/Vs above 40 K up to a maximum of 1300 cm^2/Vs at 10 K, behavior that obeys a $T^{-9.3}$ temperature dependence above 30 K. This increase on cooling is more rapid than the $T^{-1.5}$ dependence expected from acoustic phonon scattering. Below 30 K, $\mu_H(T)$ behaves as $T^{-1.1}$. These temperature-dependences are consistent with previous

measurements of $\mu_H(T)$ derived in a single-band picture (Sun, Oeschler et al. 2010, Sun, Xu et al. 2013).

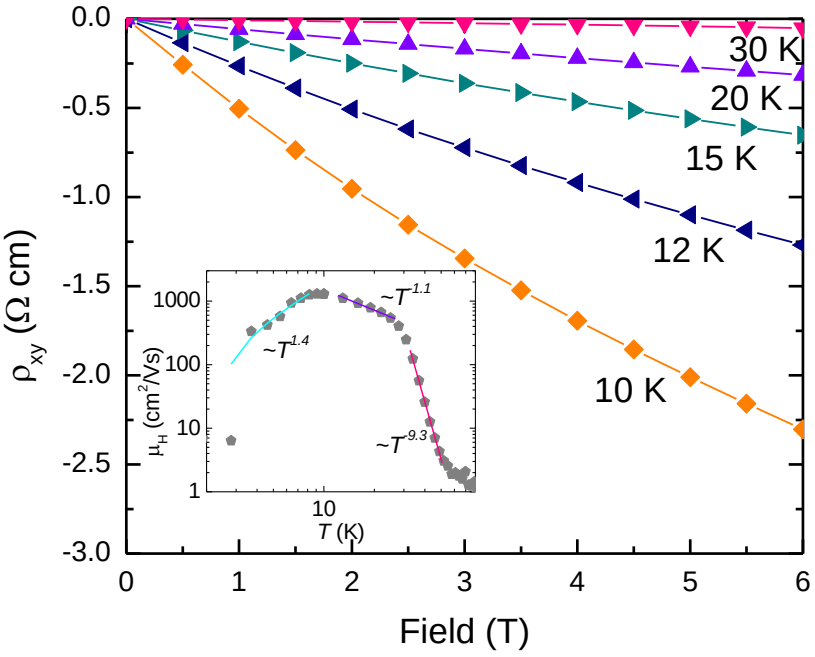


Figure 4.2: Hall resistivity, $\rho_{xy}(H)$, as a function of field at select temperatures between 10 K – 30 K. Fits to the Hall mobility, $\mu_H(T)$, are shown in the inset.

The validity of the single-band picture holds in the ITR, but not at other temperatures. Non-linearity in $\rho_{xy}(H)$ and sign changes in the high-field slope of $\rho_{xy}(H)$ above and below the ITR, both in our data and across sample studies (Takahashi, Okazaki et al. 2011, Sun, Xu et al. 2013), suggest the presence of multiple bands (fig. 4.2). A two-band analysis of our data as outlined in reference 3 yields a maximum μ_{2b}= 4,500 cm^2/Vs at 8 K. The factor of 3.5 difference between our maximum μ_{2b} and μ_H is small enough to suggest that a large difference exists between the high and low mobility bands in the two-band model. Thus, the

assumption of a dominant single band is valid, and further discussion will refer only to $\mu_H(T)$, which also allows for comparison across different studies.

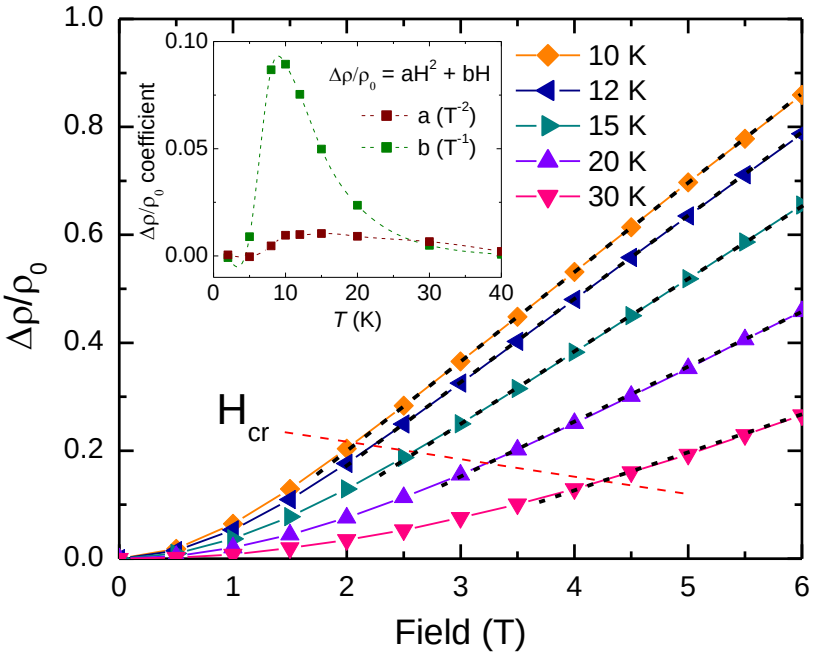


Figure 4.3: Magnetoresistance, $\Delta\rho/\rho_0(H)$, as a function of field. The dashed lines are to help guide the eye, showing the onset of the linear magnetoresistance, LMR, at the crossover field, H_{cr}. Inset shows quadratic ($a(T)$) and linear ($b(T)$) coefficients from a fit to $\Delta\rho/\rho_0(T,H) = a(T)H^2 + b(T)H$.

The longitudinal response of $\rho(T)$ to a field provides further insight into carrier dynamics. The ordinary $\Delta\rho/\rho_0$, due to the Lorentz force, exhibits a quadratic field-dependence at low fields and sublinear dependence at high fields (Olsen 1962), a description that does not fully characterize our data (figure 4.3). As T decreases below 30 K, $\Delta\rho/\rho_0(H)$ changes from quadratic to linear above $H \sim 2$ T, similar to behavior seen in other studies (Petrovic, Kim et al. 2003, Takahashi, Okazaki et al. 2011). The precise crossover field (H_{cr}) separating quadratic and linear regions varies

linearly with temperature (figure 3). Thus, $\Delta\rho/\rho_0(T,H)$ is well-parameterized by $\Delta\rho/\rho_0(T,H) = a(T)H^2 + b(T)H$, the linear and quadratic coefficient of which are also shown (fig. 4.3 inset). We see that the linear contribution dominates the response below T = 20 K. In figure 4.4 are shown $\mu_H(T)$ and $\Delta\rho/\rho_0(T, H = 6\ T)$ for T < 60 K. Note that $\Delta\rho/\rho_0(T, H = 6\ \mathrm{T})$ exhibits a peak at 10.0 ± 0.1 K, which is very close to the T_{max} of $\mu_H(T)$, 9.8 ± 0.2 K. This is the precise T-range where $S(T)$ also exhibits its maximum, as discussed below. While this agreement in T_{max} among $\Delta\rho/\rho_0(T)$, $S(T)$, and $\mu_H(T)$ has been seen in samples (Sun, Xu et al. 2013) deemed very clean by the residual resistivity ratio (RRR = $\rho(4\ \mathrm{K})/\rho(300\ \mathrm{K}) \sim 10^4$) criterion (Blatt 1968), it is not evident in samples grown differently from the present study, and where the RRR is either less well-defined or $\rho(T)$ exhibits a metal-insulator (MI) transition (Petrovic, Kim et al. 2003).

The phenomenon of linear $\Delta\rho/\rho_0(H)$ (LMR) has two prevailing explanations. In the first, LMR arises due to quantum fluctuations in the extreme quantum limit, when $n \ll n_q = (eH/\hbar c)^{3/2}$ and $T \ll T_q = eH\hbar/m^*c$, where the effective mass, m^*, is assumed to be the free electron mass (Abrikosov 2000). In our experiments, n_q = 10^{17} cm^{-3} and T_q = 6 K for H = 6 T, which are to be compared with the single band R_H-determined $n \sim 10^{17}$ cm^{-3} and the region where LMR dominates, T < 30 K. Thus, the experiments are on the boundary of the quantum regime. In the second explanation, LMR results from meso-scale disorder modeled as a random resistor network (Parish and Littlewood 2005). This model predicts a crossover from

quadratic to linear field dependence, where $H_{cr}(T)$ varies as ${\mu_H}^{-1}(T)$. We see this behavior in our data. As seen in figure 4.4a, $\mu_H(T)$ and $\Delta\rho/\rho_0(T)$ exhibit the same T-dependence. Therefore, in our data, the condition $H_{cr}(T)\sim{\mu_H}^{-1}(T)$ is equivalent to $H_{cr}(T)\sim(\Delta\rho/\rho_0(T))^{-1}$. This behavior is indicated in figure 4.3, which shows that H_{cr} does, in fact, vary inversely with $\mu_H(T)$. This result is surprising since the present samples possess low disorder by the RRR metric. The proximity to the quantum regime, however, suggests a possible explanation in terms of quantum corrections to the disorder model.

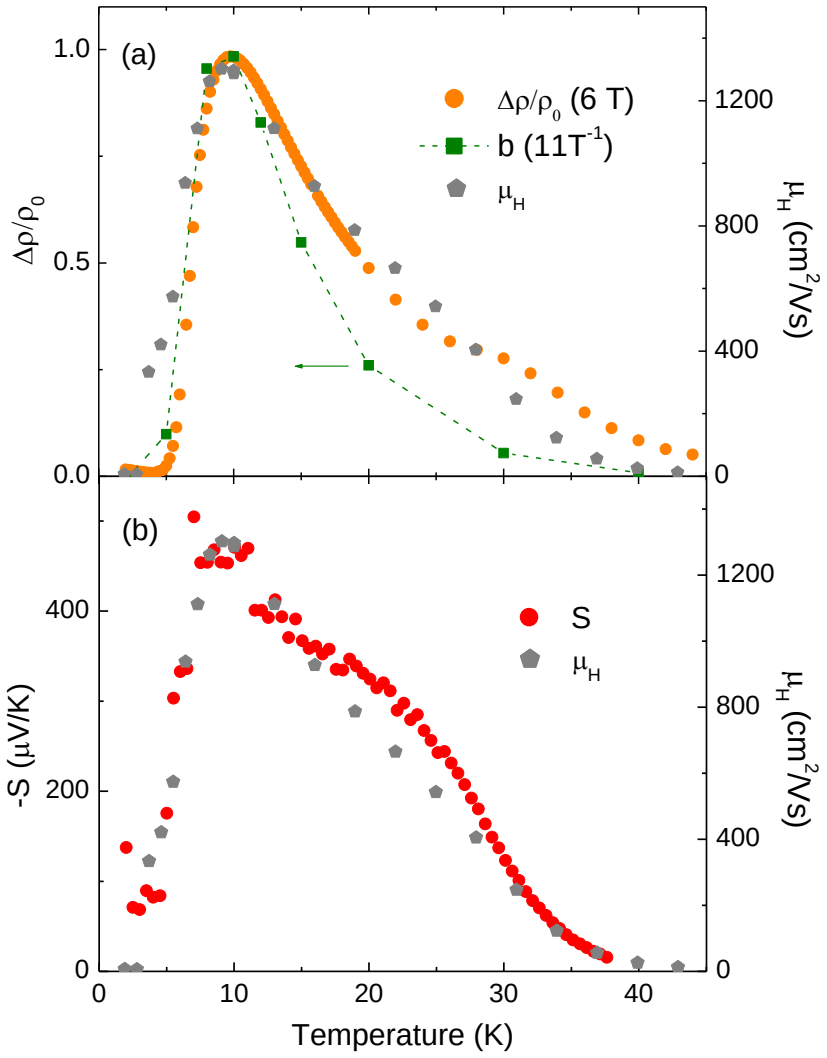


Figure 4.4: (a) Magnetoresistance $\Delta\rho/\rho_0(T)$, and Hall mobility, $\mu_H(T)$, as a function of temperature, as compared to the linear MR coefficient from the inset of figure 2, scaled ($11b(T)$, corresponding to the left axis in units of T^{-1}). (b) The thermopower, $S(T)$, and Hall mobility, $\mu_H(T)$, as a function of temperature.

The measured $S(T)$, shown in figure 4.4b, exhibits a maximum at $T_{max} = 10.0 \pm 0.3$ K, with S_{max} = 500 μV/K. Our value of T_{max} is in agreement with that seen in several other studies (Bentien, Johnsen et al. 2007, Jie, Hu et al. 2012, Sun, Xu et al. 2013). While the T_{max} variation among samples is small, S_{max} variation is

large, with our S_{max} significantly lower than in other studies. This discrepancy suggests an extrinsic origin for S_{max}, a viewpoint advanced earlier with models based on defect states (Battiato, Tomczak et al. 2015). It is notable that, despite this prevailing view, S_{max} values do not correlate with RRR values, suggesting different defect origins for these quantities (Bentien, Johnsen et al. 2007, Takahashi, Yasui et al. 2011). This suggests further that, while a strong interaction may exist between itinerant carriers and localized defects, the defects do not serve as deep charge traps that would decrease the carrier density proportional to their own density. Thus we view the magnitude of S_{max} as related to a density of shallow defects, whose separation in energy below the conduction band, as indicated by the concurring T_{max} values, is the same among different samples.

The energy scale that controls $S(T)$ has surprising implications. Using the expression for electron diffusion in a semiconductor, $S_d = -(k_B/e)[(E_c - E_F)/k_BT + A]$, where E_C and E_F are the conduction band edge and the Fermi level, respectively, and A is a constant of order unity, we obtain a value of 22.3 meV for $|E_C - E_F|$ above 25 K (Mott and Davis 1979). Assuming that E_F lies in the middle of the band gap, this leads to E_g = 44.6 meV, nearly twice the size of the band gap acquired from $\rho(T)$ (28 meV). This result is notable since the activation gap derived from $S(T)$ measurements is usually smaller than that derived from $\rho(T)$, except in the case of highly amorphous materials (Moustakas, Weiser et al. 1975). Similar analyses for $FeSb_2$ have suggested that an $S(T)$ due to a purely electronic origin is

limited by the size of the band gap (Tomczak, Haule et al. 2010). Further, the variation in S_{max} among samples suggests that $S(T)$ cannot be accounted for by E_g alone, given the good agreement (within $\pm$6 meV) in E_g across transport studies (Bentien, Johnsen et al. 2007, Takahashi, Yasui et al. 2011). Thus, an additional source of entropy is needed to augment $S(T)$ in $FeSb_2$.

Recently, a variant of the simple phonon-drag mechanism has been proposed as the source of this entropy (Battiato, Tomczak et al. 2015). In this particular scenario, the charge carriers emanating from impurity bands within 20 meV of the conduction band gain lattice entropy through strong phonon coupling. While this model reproduces the temperature-dependent features in $S(T)$, $\rho(T)$, and $R_H(T)$, and suggests an origin for defect levels, the phonon-drag coefficient is adjusted ad hoc to fit the data, thus leaving open the question of why $S(T)$ is particularly large in $FeSb_2$. Additionally, in their model, the T-dependence of the features in the transport coefficients were directly linked to the positions of impurity bands in the energy gap. Thus, the agreement in T_{max} among studies (Sun, Oeschler et al. 2010, Sun, Xu et al. 2013) would imply the presence of an impurity band at the same energy among different samples, as discussed above. Reconciling the implication of a fixed impurity band and common mechanism (phonon-drag) for $S(T)$ with the extreme variability of nearly two orders of magnitude in S_{max} among different samples may require a more fundamental effect, especially in light of the recurring proportionality between $S(T)$ and $\mu_H(T)$.

4. Discussion of proportionality between $S(T)$ and $\mu_H(T)$

The proportionality between $S(T)$ and $\mu_H(T)$ in $FeSb_2$ is puzzling. We emphasize that it is a direct proportionality and not just a similarity. In intrinsic semiconductors, both quantities increase with decreasing temperatures as $S(T) \sim T^{-1}$ and $\mu_H(T) \sim T^{-1.5}$. Each can exhibit a peak at low temperature, but the temperature at which each peak occurs does not often coincide, since the peak is determined by the carrier compensation (or doping) and band gap for $S(T)$ (Gibbs, Kim et al. 2015) and the carrier scattering mechanisms for $\mu_H(T)$ (Blatt 1968). Even when they do coincide, $S(T)$ and $\mu_H(T)$ may share a rough resemblance in *T*-dependence at most, not a proportionality. Indeed, in simple systems with elastic phonon scattering, these two quantities should be *inversely* related, a notion that is explicitly incorporated into the phonon-drag model (Blatt 1968). Contrary to the inverse relationship expected in the single-band phonon-drag picture, a comparison between $S(T)$ and μ_H(T) (figure 4.4b) shows that they are almost *directly proportional* in $FeSb_2$. With the exception of temperatures below 7 K, the data can be scaled almost exactly, for both our own experimental data and data from previous studies. We compared our results to published data sets that included both S(T) and the single-band Hall mobility on the same single-crystal samples. (Sun, Oeschler et al. 2010, Sun, Xu et al. 2013), despite drastic differences in S_{max}. Figure 4.5 shows that the proportionality constant, $S(T)/\mu_H(T)$, for a cross-section of data points in these studies is nearly constant in the ITR. To our knowledge, this direct proportionality across the entire temperature

range of the peak has not been seen in other compounds, including the isostructural homologue $FeAs_2$. In $FeAs_2$, $S(T)$ and $\mu_H(T)$ can be scaled and shown to be very nearly inversely proportional above 10 K (Sun, Xu et al. 2013). This indicates that, while $S(T)$ in $FeSb_2$ is incompatible with a simple phonon drag picture, such a model qualitatively describes $S(T)$ in $FeAs_2$. Other key differences between $FeAs_2$ and $FeSb_2$ have been discussed elsewhere (Tomczak, Haule et al. 2010, Sun, Xu et al. 2013).

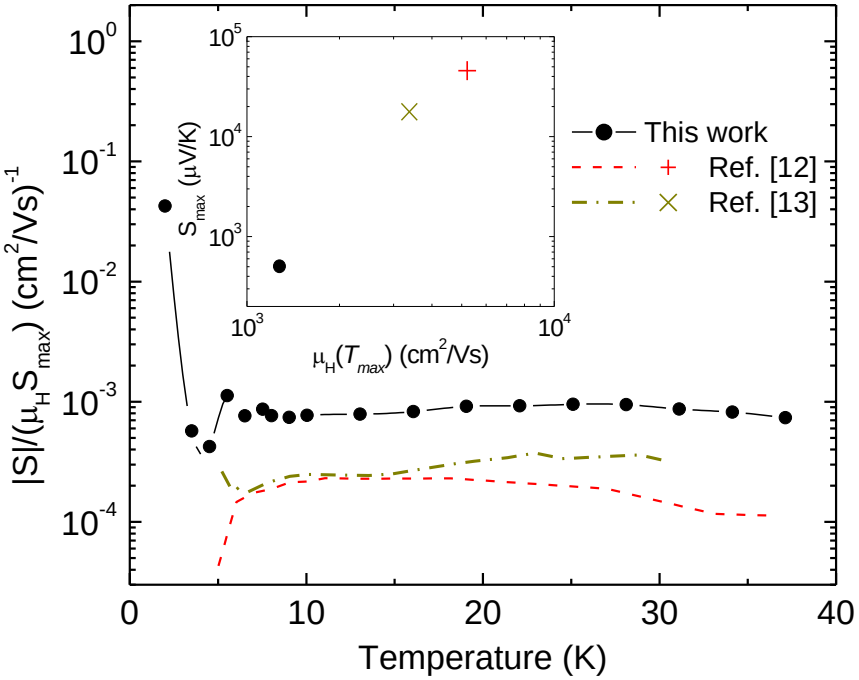


Figure 4.5: Proportionality constant, $|S(T)|/\mu_H(T)$, scaled by ${S_{max}}^{-1}$, versus temperature for this work and two others. Inset shows S_{max} as a function of $\mu_H(T_{max})$.

Comparisons to compounds such as FeSi and $FeGa_3$, which have similar band structure and magnetic excitation spectra, provide contrast for the interrelationships discussed here for $FeSb_2$. In addition, due to a possible connection between these

compounds and Kondo insulators (Tomczak, Haule et al. 2013), we also consider SmB_6. While $FeGa_3$ does demonstrate a rough similarity in temperature profile between $S(T)$ and $\mu_H(T)$, the magnitude of $\mu_H(T)$ is much smaller (only a few cm^2/Vs) than in $FeSb_2$, and the agreement near T_{max} = 13 - 16 K is less striking (Wagner-Reetz, Kasinathan et al. 2014). This suggests that $S(T)$ and $\mu_H(T)$ in $FeGa_3$ have different origins. The same qualitative statements also hold true for SmB_6, where the rough agreement in $S(T)$ and $\mu_H(T)$ is thought to occur due to a crossover from bulk to topological surface conduction (Luo, Chen et al. 2015), and where S_{max} does not violate the upper bound set by the band gap (Sluchanko, Glushkov et al. 2001), unlike in $FeSb_2$. Meanwhile, $S(T)$ and $\mu_H(T)$ in FeSi display no proportionality, and on the contrary, appear to be inversely related for T > 50 K (where S_{max} occurs), hinting that phonon-drag may be at play (Sun, Wei et al. 2014). This is consistent with the fact that FeSi does not demonstrate the same degree of sample-dependence and variability in S_{max} shown by $FeSb_2$, $FeGa_3$, or SmB_6.

To our knowledge, such a direct proportionality between $S(T)$ and $\mu_H(T)$ has not been experimentally observed or directly discussed. In one study that compared the thermal and charge mobilities of $FeSb_2$ and sought an explanation of the large $S(T)$ through a dispersive relaxation time, a relationship between $S(T)$ and $\mu_H(T)$ was alluded to, but the proportionality not explicitly discussed (Sun, Xu et al. 2013). Studies on other systems may show an $S(T)$ and $\mu_H(T)$ with T-dependences that bear a resemblance, but not a strict proportionality in the vicinity of a peak. As mentioned

above, $S(T)$ and $\mu_H(T)$ can have a similar functional dependence on T (T^{-1} and $T^{-1.5}$) at low temperatures, but for unrelated reasons. One theoretical model for which a near proportionality incidentally appears is that of heavily doped semiconductors with parabolic conduction and valence bands, with the additional effect of randomly distributed point scatterers (Fischbeck 1975). In this numerical model, parameters are chosen so as to simulate a uniform distribution of impurity states in the gap, each of which is treated as an individual point scatterer with δ-like potentials. These parameters, as well as a large difference in the density of states between bands, determine the location of the Fermi level and the relative magnitudes of the Hall and longitudinal conductivity, leading to an $S(T)$ and $\mu_H(T)$ of the same carrier type and similar T-dependence near room temperature. As with the LMR, however, we see no obvious indication of strong disorder in $FeSb_2$. With so many features shared with models for disordered systems, $FeSb_2$ seems to possess something akin to "hidden disorder" that unexpectedly connects these various transport quantities.

Given the degree of variability among different samples of $FeSb_2$, the reproducibility of the effect across multiple studies precludes coincidence. Further, figure 4.5 (inset) demonstrates that S_{max} and μ_{Hmax} are clearly correlated, but it is unclear whether or not the relationship is *causal*. If causal, this could possibly hint at an entirely new type of scattering, for instance, one where entropy is *shed* rather than gained.

An alternative possibility is that $S(T)$ and $\mu_H(T)$ are governed by proximity to a quantum critical point. A common indicator of quantum criticality in heavy fermion systems and high-T_c superconductors is a T-linear $\rho(T)$, which is due to the T-dependence of the relaxation time, given by $\tau \propto \hbar/k_B T$ (Phillips and Chamon 2005). This relationship would therefore result in $\mu_H(T)$ proportional to T^{-1}, the same as in $S(T)$, thus leading to a shared T-dependence. Quantum criticality might also account for the linear magnetoresistance, as the magnetic field may play a similar role to the temperature in setting the energy scale in the quantum critical regime (Hayes, McDonald et al. 2016), thus also providing a possible explanation for why $H_{cr}(T)$ is linear. Furthermore, quantum criticality can lead to an enhanced $S(T)$ (Paul and Kotliar 2001, Limelette, Saulquin et al. 2010), which may help account for the large $S(T)$ in $FeSb_2$. Given the magnetism and metal-insulator transition seen in lightly doped-$FeSb_2$ (Hu, Mitrovic et al. 2009, Hu, Wang et al. 2012), quantum criticality seems possible, warranting further theoretical studies.

In conclusion, the remarkable proportionality between $S(T)$ and $\mu_H(T)$ is a unique property of $FeSb_2$ that merits further examination. Understanding this proportionality may lead to the discovery of other candidate materials for thermoelectric cooling applications that have a high power factor, or possibly even to new physics. Here, we have found a significant clue that brings us one step closer to a complete picture for $FeSb_2$.

Chapter V: Positive linear magnetoresistance in $BaIrO_3$

1. Background on $BaIrO_3$

The Ir oxides offer the potential for exotic phases, including topological insulators, quantum spin liquids, and magnetic insulators, among others (Witczak-Krempa, Chen et al. 2014). These phases arise due to the comparable energy scales of the Coulomb repulsion (U), energy bandwidth (W), and large spin-orbit coupling (SOC), which compete to yield ground states that are often not metallic, despite the extended 5d orbitals, which often overcome the localizing effects of U and SOC. Studies on Sr_2IrO_4, for example, show an unexpected band gap due to the interplay of strong SOC and U, thus resulting in a novel Mott ground state with effective total angular momentum $J_{eff} = 1/2$, as opposed to the conventional Mott insulator which can be fully described by $S = 1/2$ (Kim, Jin et al. 2008). This phase has been called a spin-orbit Mott insulator (SOMI), since the large spin-orbit coupling splits the wide 5d t_{2g} band into $J_{eff} = 1/2$ and $J_{eff} = 3/2$ bands, the former of which is narrow enough to allow the Coulomb interaction to open a Mott gap (fig. 5.1). Phases of similar origin occur in the pyrochlore iridates (R_2IrO_7) and the Ruddleston-Popper series ($Sr_{n+1}Ir_nO_{3n+1}$ for n =1, 2, ∞), all in part because of the large SOC of Ir, which in these systems is estimated to be ~0.4 eV (Witczak-Krempa, Chen et al. 2014).

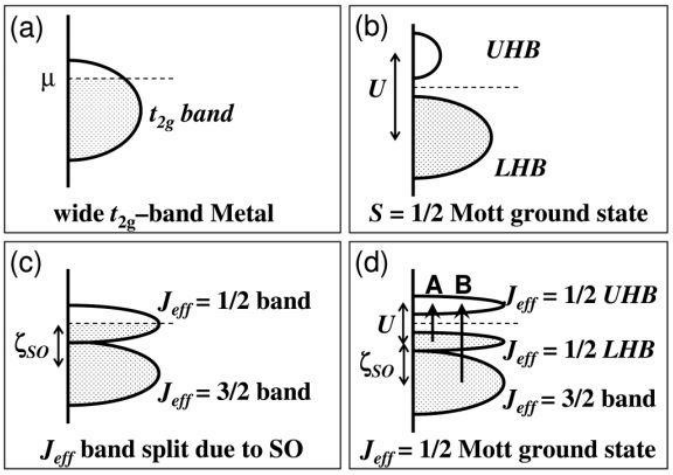


Figure 5.1: Schematic band diagrams showing various energy scales involved in the formation of a J^{eff} = ½ Mott insulator: (a) without SOC or U, (b) with an unrealistically large U that results in the canonical S = ½ Mott state, (c) with SOC only, (d) with both SOC and U. Adapted from (Kim, Jin et al. 2008).

Based on density functional theory calculations in a local spin density approximation, $BaIrO_3$ is also thought to be a J_{eff} = ½ SOMI (Ju, Liu et al. 2013), and correspondingly exhibits weak ferromagnetism and a gap, despite wide (5d) bands. Photoemission and thermopower studies find a small gap (25 - 50 meV) below the ferromagnetic transition at the Curie temperature, $T_c \sim 180$ K (Maiti, Singh et al. 2005, Cheng, Zhou et al. 2009). While $d\rho/dT < 0$ for $T > T_c$, a clear gap in that temperature range has not been deduced due to a sublinear Arrhenius form, and band structure calculations yield only a metallic phase above T_c (Whangbo and Koo 2001, Maiti 2006). At T_c, $BaIrO_3$ also exhibits simultaneous charge ordering, and at even lower temperatures (T < 30 K) displays a large non-linear optical conductivity (Cao, Crow et al. 2000, Nakano and Terasaki 2006). Although the nature of the charge ordering remains unclear, analyses of the non-linear optical conductivity and x-ray

diffraction measurements have ruled against a charge density wave (Nakano and Terasaki 2006, Terasaki, Ito et al. 2016). The combined presence of these many interesting properties has incited much interest in $BaIrO_3$.

To further understand the relationship between the magnetic order and charge carrier dynamics, we have measured the Hall coefficient ($R_H(T)$) and magnetoresistance, $\Delta\rho/\rho_0(T,H)$, of $BaIrO_3$ below $T_c = 165$ K and uncovered a *positive* linear magnetoresistance (PLMR) that is non-saturating in fields of up to 8 T. The positive sign of $\Delta\rho/\rho_0(T,H)$ indicates that increasing the field leads to greater scattering, counter to the negative field-dependence expected for ferromagnetically ordered materials, where spin-scattering is reduced with increasing field. Additionally, LMR has been of great interest recently due to its prevalence in topological systems (Wang and Lei 2012), and more generally as a harbinger of interesting transport phenomena, often mediated by quantum effects or disorder (Hu and Rosenbaum 2008). Thus, in light of its many other intriguing attributes, $BaIrO_3$ is an attractive test bed for studying PLMR.

2. Experimental setup

The 9R polytype of $BaIrO_3$ crystallizes in a monoclinic structure, with Ir_3O_{12} trimers vertex linked along the crystallographic c-axis to form a quasi-one-dimensional structure (figure 5.2) (Siegrist and Chamberland 1991). Our single

crystals were synthesized using $IrCl_3 \cdot xH_2O$ in a $BaCl_2$ flux. The starting material and flux were ground together via mortar and pestle. The mixture was heated at 1000-1025 °C for 3 hours in an alumina crucible and then cooled at a rate of 2 °C/hr to 900 °C, then allowed to cool to room temperature. The excess $BaCl_2$ was dissolved with water and the crystals were then filtered and collected. Silver epoxy was used for current/voltage contacts in all transport measurements, which were performed in a commercial cryostat in a standard dc four probe configuration with the current, I, parallel to the c-axis.

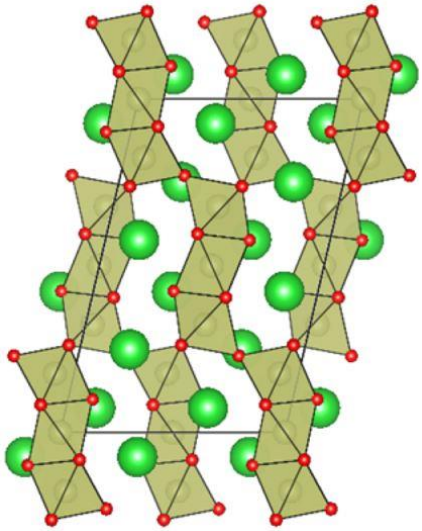


Figure 5.2: Monoclinic 9R polytype $BaIrO_3$ (green = Ba, brown = Ir, red = O). From (Flynn, Li et al. 2016).

3. Results and discussion

Resistivity ($\rho(T)$) data are shown in figure 5.3, where the sudden upturn at T_c = 150 K indicates that our sample is of reasonable quality to those used in previous

studies (Cao, Crow et al. 2000). The hump-like behavior of $\rho(T)$ in this temperature range has been attributed to the onset of charge order and opening of a small gap (Cao, Crow et al. 2000, Kini, Bentien et al. 2005). The derivative of the resistivity, $-d\log\rho/d(1/T)$, is shown in the inset of figure 5.3, and exhibits a negative peak at T_c, likely a result of short-range spin-fluctuations due to the onset of ferromagnetic order. Peaks in $d\rho/dT$ near T_c are known to occur in ferromagnets for this reason, but are usually positive in sign due to the metallic T-dependence (Fisher and Langer 1968).

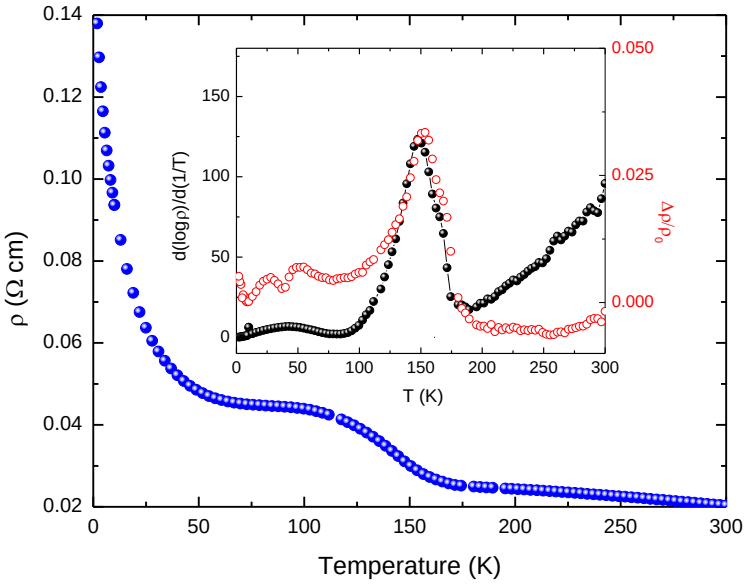


Figure 5.3: Resistivity as a function of temperature. Inset shows $d\log\rho/dT$ (black, left axis) and $\Delta\rho/\rho_0$(red, right axis) versus temperature.

Weak ferromagnetism in $BaIrO_3$ has been established in previous studies, where a small magnetic moment, $\mu \approx 0.04\ \mu_B$/Ir, was found (Cao, Crow et al. 2000). Muon-spin relaxation (μSR) measurements have ruled against canting of antiferromagnetic spins as the origin of the ferromagnetism (Brooks, Blundell et al.

2005). As mentioned above, $\Delta\rho/\rho_0$ is expected to be negative due to the ferromagnetic order. We find, however, that $\Delta\rho/\rho_0(T, H = 6\text{ T})$ (figure 5.3 inset) is *positive*, and exhibits a peak at T_c, mirroring $-d\rho/dT$. Peaks in $\Delta\rho/\rho_0(T)$ near T_c have previously been seen in ferromagnetic metals, such as $La_{0.7}Sr_{0.3}MO_3$ (Yin, Zhang et al. 2015) and $Pr_{0.5}Sr_{0.5}CoO_3$ (Mahendiran and Schiffer 2003), but were *negative* in sign, as expected. Even in so-called "magnetic semiconductors," such as EuO and $CdCr_2Se_4$, $\Delta\rho/\rho_0$(T) was negative (Haas 1968, Oliver, Mcwhorte.Al et al. 1972). Thus, the full picture for $\Delta\rho/\rho_0$(T) goes beyond simple spin fluctuations.

The field dependence, $\Delta\rho/\rho_0(H)$, similarly hints at an additional scattering mechanism. Within $\pm$30 K of T_c, $\Delta\rho/\rho_0(H)$ is positive with a strong linear component, as shown in figure 5.4a for the transverse configuration ($\Delta\rho_\perp/\rho_0$, with $H \perp I$). Thus, the PLMR is present even for $T > T_c$. We discuss the implications of this below. Although the data are not shown, the longitudinal configuration ($\Delta\rho_\parallel/\rho_0$, with $H \parallel I$) yields a similar PLMR temperature profile.

For $T < T_c$, the magnetic order leads to a domain effect not seen in $\Delta\rho/\rho_0(H)$ at higher T that is sensitive to small differences in sample geometry, and therefore leads to a hysteretic butterfly-shaped $\Delta\rho/\rho_0(H)$ that is slightly off-center from $(\Delta\rho/\rho_0, H) = (0,0)$ (Segal, Shaya et al. 2009). We therefore subtracted the antisymmetric (Hall) component from our data in order to obtain the longitudinal signal. In this low-T range, $\Delta\rho_\perp/\rho_0(H)$ exhibits positive hysteretic butterfly shapes (fig. 5.4b), which are a common indication of domain effects in magnetic materials

(Coey, Venkatesan et al. 2001). Subtracting the linear slopes from the data yield hysteretic curves that are related to M, where the minima in $\Delta\rho_{\perp}/\rho_0(H)$ roughly correspond to the coercive field, H_c, as seen in data at 1.5 K from a previous study (Kida, Yoshii et al. 2009), as well as in other ferromagnets (Rautama, Boullay et al. 2008, Zhang, Feng et al. 2014). Our $\Delta\rho_{\parallel}/\rho_0(H)$ data exhibit similar hysteretic butterfly shapes of a smaller magnitude ($\lesssim 20\%$ difference). The difference can be accounted for through the anisotropic magnetoresistance (AMR) effect, where changes in configuration lead to different scattering cross-sections due to spin-orbit coupling (Mcguire and Potter 1975). Regardless, the shape and relative T-dependence of both $\Delta\rho_{\perp}/\rho_0(H)$ and $\Delta\rho_{\parallel}/\rho_0(H)$ is the same. Further discussion can be generalized to either, and so we refer hereafter only to $\Delta\rho/\rho_0(H)$ without distinction.

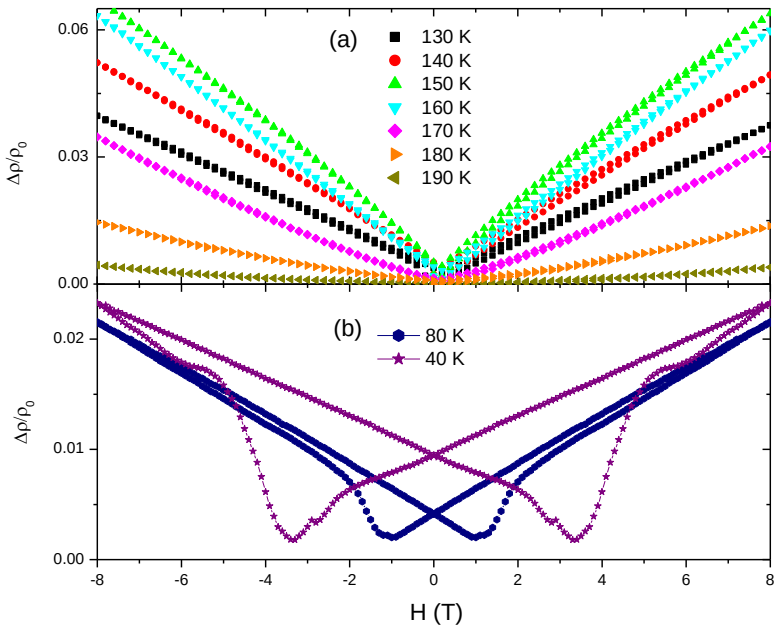


Figure 5.4: (a) Magnetoresistance as a function of field at multiple temperatures near T_c = 163 K and (b) well below T_c.

Isotropic, positive, and hysteretic $\Delta\rho/\rho_0(H)$ has previously been seen in melt-spun ribbons of $Nd_2Fe_{14}B$ with 50 wt% Fe (Idzikowski, Wolf et al. 1997), where the $\Delta\rho/\rho_0(H)$ behavior was attributed to the "inverse giant magnetoresistance" (IGMR) effect found in magnetic multilayer systems (Renard, Bruno et al. 1996). A similar explanation was invoked for $(Ni_{80}Fe_{20})_{0.75}Mn_{0.25}$ films, where the butterfly shapes of $\Delta\rho/\rho_0(H)$ were inverted, but still overall negative in sign (Kim, Lim et al. 2003). Previous measurements on $BaIrO_3$ at T = 1.5 K were analyzed using a nanoscale spin-valve model assuming nonequivalent interaction strengths among Ir atoms at different positions within the lattice structure (Kida, Yoshii et al. 2009). The model qualitatively described the low-field (butterfly) portion of the symmetric $\Delta\rho/\rho_0(H)$, but did not address the overall positive sign and behavior of $\Delta\rho/\rho_0(H)$ for $H > H_c$.

For $T < T_c$ and $H > H_c$, the positive, linear, and non-saturating $\Delta\rho/\rho_0(T,H)$ evinces that the PLMR found for $T > T_c$ continues into the ordered phase. We disentangled the LMR from the ordinary ($\propto H^2$) component by fitting the data to a quadratic equation, $\Delta\rho/\rho_0(T,H) = a(T)H^2 + b(T)H + c$ (fig. 5.5), where the constant c accounts for the additional offset mentioned above. The $a(T)$ behavior can be understood within the framework of spin-fluctuations in the vicinity of T_c. Above T_c, as spins begin to align, spin-scattering increases, whereas the opposite is true below T_c, when the spins are spontaneously aligned and spin-scattering is reduced. The $b(T)$ curve, however, exhibits a large peak just below T_c. This tracks the overall

$\Delta\rho/\rho_0(T, H = 6\ \mathrm{T})$ (fig. 5.4b), thus indicating that the LMR is the predominant contribution near the peak.

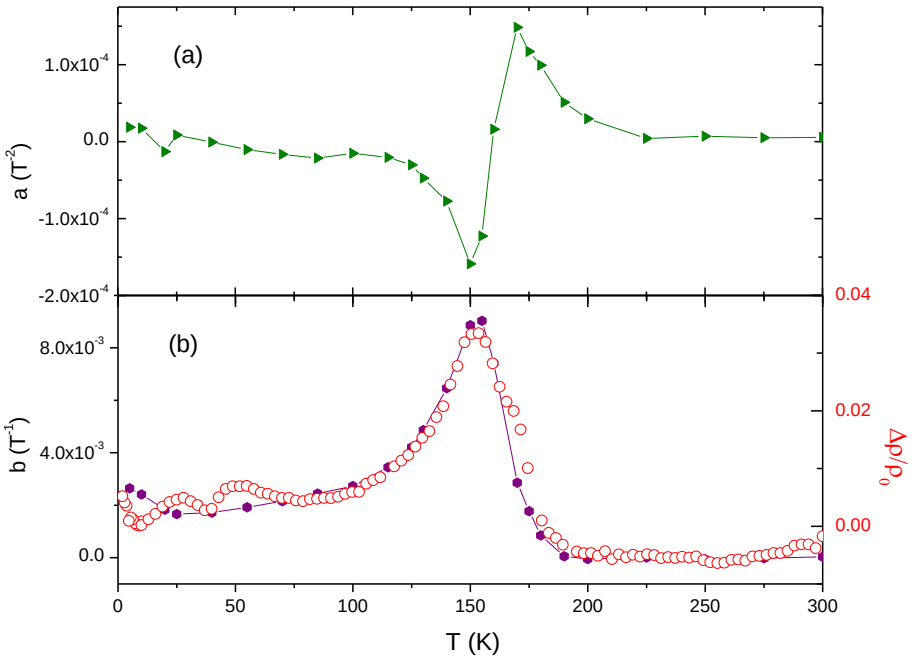


Figure 5.5: Quadratic (a) and linear (b, left axis) coefficients of the magnetoresistance field dependence, as a function of temperature, compared to the full magnetoresistance ((b) right axis, red).

PLMR has been shown to occur in ferromagnets in systems with low carrier densities and strong disorder (Manyala, Sidis et al. 2000), as well as in geometrically constrained thin films (Gerber, Kishon et al. 2007). In each of these cases, the PLMR is similar in magnitude for both transverse and longitudinal configurations and shows no signs of saturating, even at high temperatures ($T \sim 100$ K), as in our data, thus suggesting a similar mechanism for PLMR in $BaIrO_3$. Both the low carrier density/strong disorder and thin geometrically constrained models also attribute the PLMR to quantum interference effects. In the disordered ferromagnet model,

electrons scatter off of each other, and their scattering amplitudes interfere coherently and lead to PLMR, an effect that is enhanced by disorder (Manyala, Sidis et al. 2000). Geometrically constrained ferromagnets have a field-induced correction to the resistivity that is positive and linear in H (Gerber, Kishon et al. 2007). $BaIrO_3$ does not fit the sample profile of either model perfectly, as Hall measurements on our samples (discussed below) yield a relatively large single-band carrier density of 10^{22} cm^{-3}, and our measurements were performed using single crystals, not thin films. We speculate that the quasi-one-dimensionality contributes to quantum interference effects by rendering $BaIrO_3$ more susceptible to disorder, an effect that might be amplified near T_C due to fluctuations. We therefore tentatively attribute our findings to these quantum interference effects.

One remaining mystery concerns $\Delta\rho/\rho_0(T)$, which appears near T_c, thus implying a relationship to the charge or magnetic order where the spin or charge fluctuations associated with the low-T ordering might augment the quantum effects. Future studies that clarify the nature of the charge order in this system, and its relation to the magnetic order, may help us further comprehend the PLMR in $BaIrO_3$.

In addition to the PLMR, $BaIrO_3$ exhibits the anomalous Hall effect (AHE) commonly found in ferromagnets (figure 5.6), which can be related to the field-dependent transverse resistivity through $\rho_{xy}(H) = R_H H + R_{AHE} M$, where M is the magnetization and R_{AHE} is the anomalous Hall coefficient (Nagaosa, Sinova et al. 2010). The AHE is intimately related to SOC effects, as discussed in Chapter 1.

Future measurements of M will allow us to analyze the AHE further, but for now, we focus on the ordinary Hall effect. Since R_{AHE} dominates $\rho_{xy}(T)$ at low fields, we examine the data for $H > H_S$, where H_S is the field at which M saturates, in order to extract data on the sign and density of charge carriers (figure 5.6 inset). As in previous thermopower studies, the primary sign of the carriers is found to be positive (Kini, Bentien et al. 2005, Nakano and Terasaki 2006). The sign of R_H changes from positive to negative, and then positive again around T_c. This behavior could be attributed to either an anisotropic scattering time, τ, as seen in quasi-one-dimensional metals (Wakeham and Hussey 2012), or on a depletion of carriers upon opening of the gap, as seen in transition metal dichalcogenides upon opening of the charge density wave gap (Evtushinsky, Kordyuk et al. 2008). Thus, future studies on the charge ordering in $BaIrO_3$ may help clarify this double sign change by shedding light on the behavior near T_c.

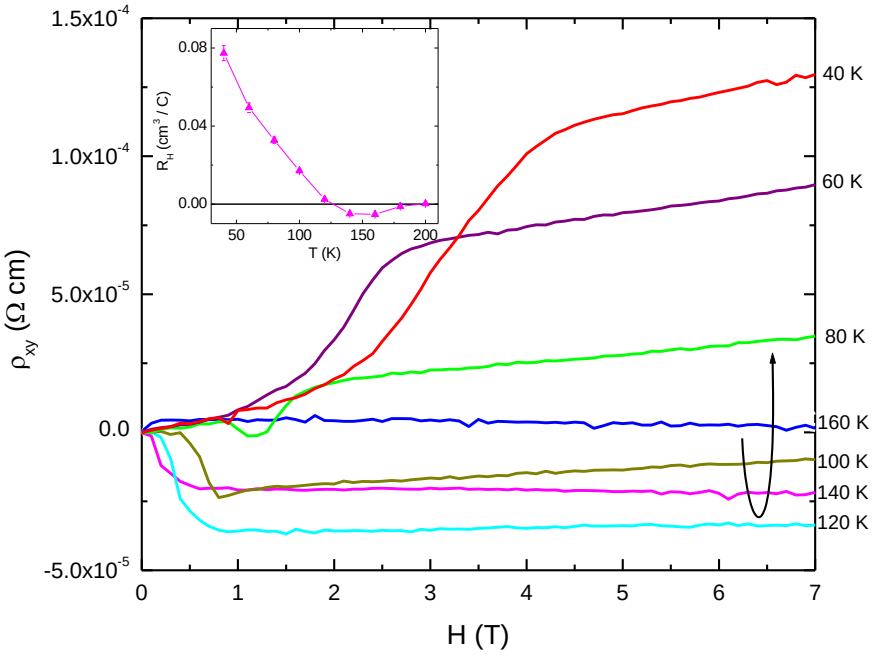


Figure 5.6: Transverse resistivity as a function of field at several temperatures. The black arrow points in the direction of decreasing temperature. Inset shows the Hall coefficient as a function of temperature, as calculated from the high field (linear) portions of the transverse resistivity curves.

In summary, $BaIrO_3$ exhibits an AHE and unexpected PLMR, the latter of which we attribute to quantum interference effect. These properties arise in part due to the large SOC, competing energy scales, and possibly the quasi-one-dimensionality. Future studies on polycrystalline samples, which have a cleaner gap (Zhao, Yang et al. 2008), may provide further insight into the effects of disorder, as well as into the significance of the quasi-one-dimensionality, which will no longer be in play.

Chapter VI: Low-temperature effects of In doping in $CoSb_3$/$RhSb_3$

1. Background

Materials from the skutterudite structural family (figure 6.1) have been extensively studied for their potential as thermoelectric (TE) materials (Caillat 1993, Slack and Tsoukala 1994). Systems such as Co_4Sb_{12} and Rh_4Sb_{12} are of particular interest due to their large high-temperature $S(T)$ and electrical conductivity, $\sigma(T)$ (Kurmaev, Moewes et al. 2004), which suggests the possibility of a high thermoelectric figure of merit, ZT. Their skutterudite cage-like structure allows for the introduction of so-called "rattler" atoms that act as strong phonon scattering sites, thus lowering the thermal conductivity (Rowe 1995, Sales, Mandrus et al. 1996) and further enhancing ZT by nearly tenfold (He, Chen et al. 2006, Mallik, Stiewe et al. 2009, Eilertsen, Li et al. 2011). Previously studied filler atoms include several rare earths (La, Ce), alkaline earth metals (Ba, Sr, Ca), and post-transition metals (Sn, Pb, Tl) for the Co_4Sb_{12} system, as discussed in (He, Chen et al. 2006) and (Shi, Yang et al. 2011). Studies of partially filled Rh_4Sb_{12} , include La, Y and I filler atoms examined at low temperatures (< 300 K), and In at high temperatures (300 K – 600 K) (Eilertsen, Li et al. 2011). In light of the possibility of large ZT (> 1) in these compounds, researchers continue to search for the optimal blend of rattler atom and host skutterudite.

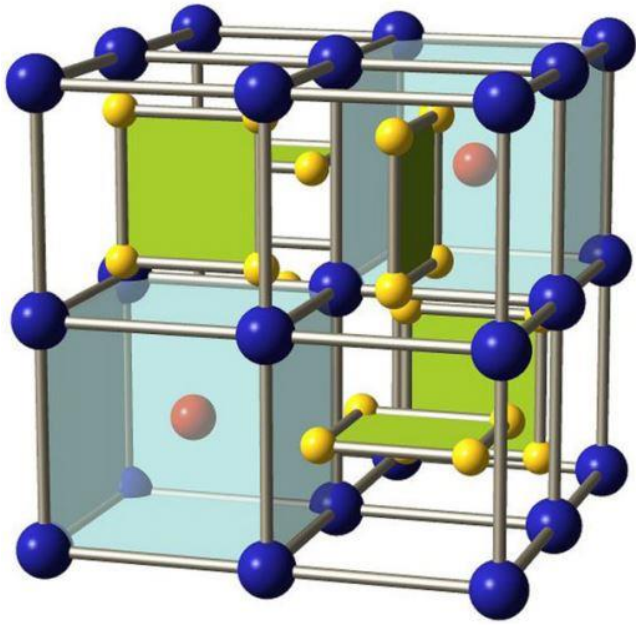


Figure 6.1: Crystal structure of $In_x(Co_4,Rh_4)Sb_{12}$, where the cubic sublattice is formed by the Co (Rh) atoms (blue), with Sb_4 (yellow) planar rings (green) and interstitial voids (turquoise) filled with In rattlers (red). From (Eilertsen, Li et al. 2011).

Additionally, materials that are of interest for thermoelectrics may also be pertinent to topological insulators (TIs), due to the mutual desirability of heavy atoms and a narrow band gap. Heavy atoms more effectively scatter thermal phonons in TEs and are required for strong spin-orbit coupling in TIs, while a narrow band gap leads to increased $\sigma(T)$ in TEs and facilitates band inversion in TIs. For example, two canonical TI systems, Bi_2Se_3 and Bi_2Te_3, were first studied in the context of TEs (Champnes.Ch, Muir et al. 1967, Xia, Qian et al. 2009, Zhang, Liu et al. 2009). After the revelation that TIs and TEs have similar material requirements, several other TEs have since been re-evaluated for TI-ness. Thus, eighteen years after the linear bands in Co_4Sb_{12} were first commented upon (Singh and Pickett 1994), it has been predicted

that Co_4Sb_{12} may be close to a topological transition and that Rh_4Sb_{12} is a zero-gap topological semimetal (Pardo, Smith et al. 2012).

In this study, we measured the low-temperature properties of the unfilled skutterudite compounds Co_4Sb_{12} and Rh_4Sb_{12}, along with their partially indium-filled counterparts ($In_{0.1}Co_4Sb_{12}$ and $In_{0.1}Rh_4Sb_{12}$) in order to understand the electronic effect of rattlers, beyond their role as phonon scatterers, at energy scales lower than previously explored in the context of room temperature thermoelectric cooling (He, Chen et al. 2006, Mallik, Stiewe et al. 2009, Wang, Cai et al. 2009, Eilertsen, Li et al. 2011, Eilertsen, Rouvimov et al. 2012). We have measured the low-temperature thermopower ($S(T)$), specific heat ($C(T)$), magnetic susceptibility ($\chi(T)$), and resistivity ($\rho(T)$) of each of our samples at low temperatures (2 K – 300 K) in order to shed light on the efficacy of In as a rattler and donor as compared to other filler atoms, as well as on differences between Co_4Sb_{12} and Rh_4Sb_{12}.

We also attempted to use the low-temperature $C(T)$ measurement to probe the possible topological behavior of Rh_4Sb_{12}, and will briefly discuss these results.

Unfortunately, metastability of the samples might be an issue. The In-doped samples have been shown to be metastable at temperatures well below 600 ℃, as the In atoms diffuse out of their cages and form InSb nanoinclusions (Eilertsen, Rouvimov et al. 2012). Thus, some of the results below might be affected by a possible variation in In content.

2. Experimental methods

Polycrystalline samples of Co_4S_{12} ($CoSb_3$), $In_{0.1}Co_4Sb_{12}$, Rh_4Sb_{12} ($RhSb_3$), and $In_{0.1}Rh_4Sb_{12}$ were prepared via solid-state reaction, described elsewhere (He, Chen et al. 2006, Eilertsen, Li et al. 2011). Indium was chosen as the rattler atom due to its small size relative to the cage structures of the parent compounds (covalent radius of r = 1.08 Å for In^{3+}, relative to lattice constants of 9.0357 Å and 9.2294 Å for $CoSb_3$ and $RhSb_3$, respectively), which allows for weak bonding to the lattice (Eilertsen, Li et al. 2011, Eilertsen, Rouvimov et al. 2012). The compounds were partially filled at 0.1 In atoms per unit cell due to limitations on thermodynamic stability in phases with higher filling, with an upper limit in Co_4Sb_{12} of 0.22 and of 0.15 in Rh_4Sb_{12}. Measurements were performed as described earlier.

3. Results and discussion

The $C(T)$ of each sample was measured as a function of temperature and plotted as $C(T)/T$ versus T^2 (figure 6.2). All samples behaved nearly linearly as a function of T^2, thus indicating a dominant lattice contribution in $C(T)$, except for $In_{0.1}Rh_4Sb_{12}$, which exhibited an upturn below ~4 K (discussed below). For the zero-field measurements, the partially filled samples exhibit a noticeable γ-term, unlike in the unfilled samples, where the γ is insignificant.

We considered a $C(T)$ of the form

$$C(T) = \gamma T + aT^3 \ln(T) + bT^3, \tag{6.1}$$

where the first term arises from electronic contributions, the second term from spin fluctuations, and the third from the lattice (Lederer and Mills 1968, Tari 2003). The addition of In donors introduced a γ in the filled compounds, while only the $In_{0.1}Rh_4Sb_{12}$ exhibited a significant $T^3\ln(T)$ term (upward turn below 10 K). The specific heat for $In_{0.1}Rh_4Sb_{12}$ was subsequently measured in fields of 3 T and 6 T, where it was found that in a 3 T field, the upturn was slightly less pronounced, and by 6 T was noticeably flatter (figure 6.2 inset), thus pointing to paramagnetic spin fluctuations as an origin for the low-T upturn (Ikeda, Dhar et al. 1991).

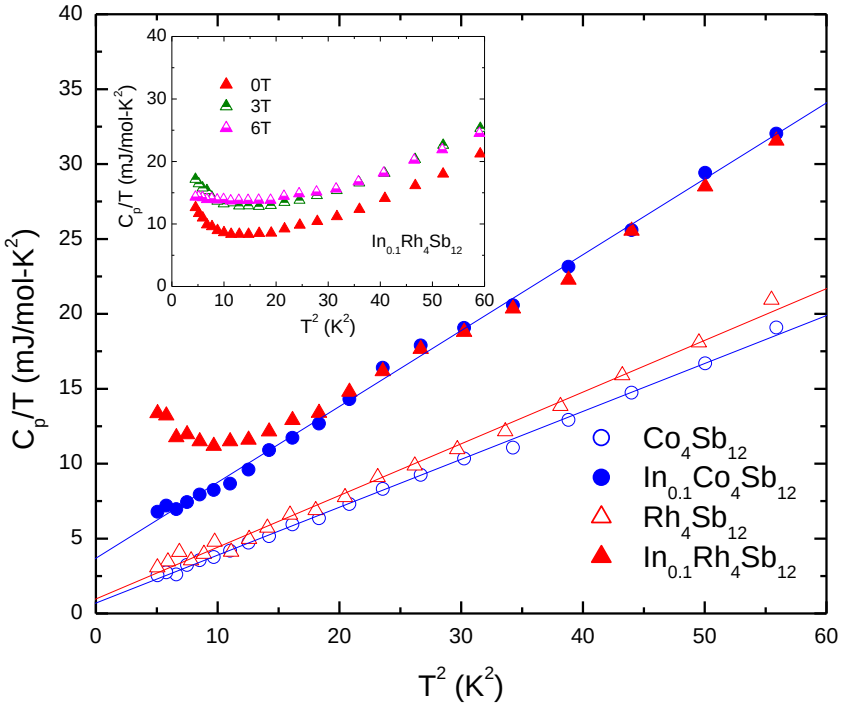


Figure 6.2. Specific heat as a function of temperature squared, per mole of Co or Rh. Inset shows field dependence of $In_{0.1}Rh_4Sb_{12}$.

Measurements of $C(T)$ may also provide a test for a topological band structure. The linear dispersion relationship in TIs is reminiscent of the energy dispersion of phonons – thus, contributions from each should have the same T-dependence in $C(T)$ (Ashby and Carbotte 2014). The presence of Dirac or Weyl points should therefore lead to an enhanced T^3 term in $C(T)$. In order to separate the electronic contribution from that of the lattice, however, an external magnetic field must be applied that is much larger in energy than the thermal energy scale ($k_B T$). In such a regime, the electronic contribution has been predicted to become linear in T (Ashby and Carbotte 2014). We found a slight difference between the data at

$H = 0\ T$ up to $H = 6\ T$ (figure 6.3), which implies a possible topological effect. Higher field studies may shed further light.

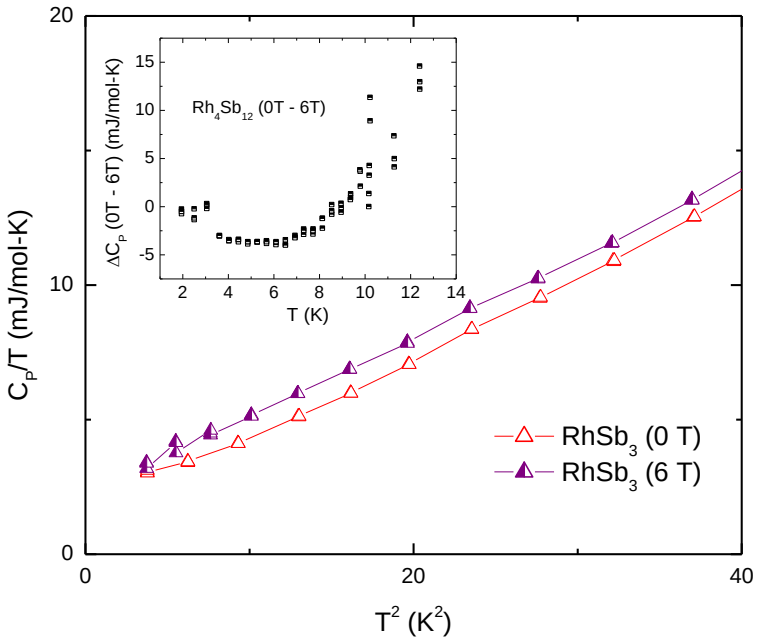


Figure 6.3: Specific heat divided by temperature as a function of T^2 for $RhSb_3$ at $H = 0$ T and 6 T. Inset shows the difference between the two $C(T)$ data sets as a function of T.

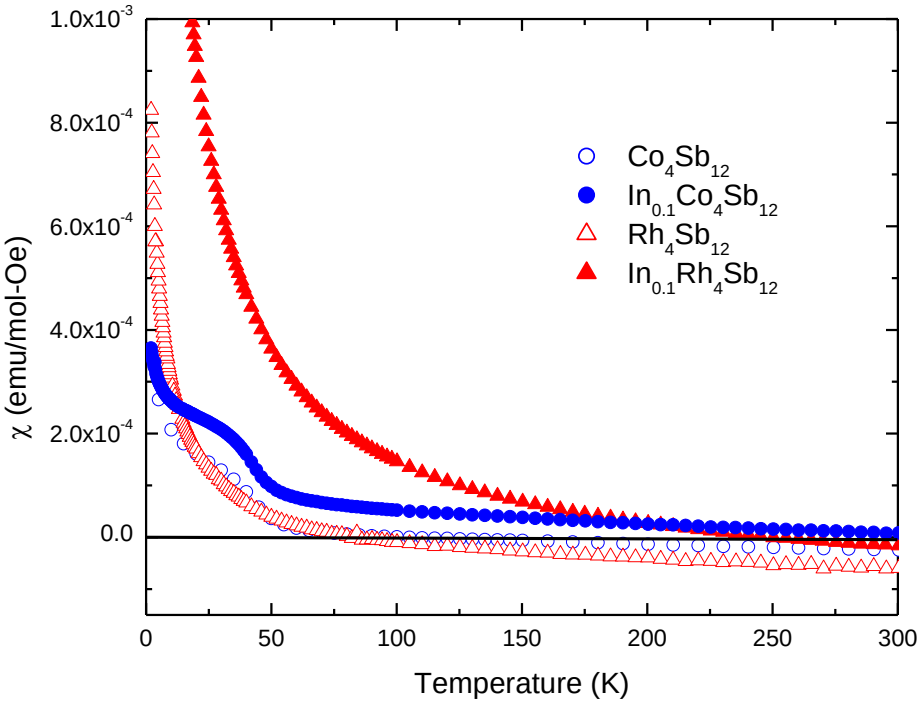


Figure 6.4: Magnetic susceptibility as a function of temperature.

For all of the samples, $\chi(T)$ (figure 6.4) is small and nearly temperature independent over most of the range above 50 K. The pure samples are mostly diamagnetic, in agreement with previous low-temperature studies on Rh_4Sb_{12} and p-type single crystal samples of Co_4Sb_{12} (Ackermann and Wold 1977, Morelli, Caillat et al. 1995, Wojciechowski 2007). We note that our data in figure 6.4 have been corrected for core diamagnetism, which may account for the small discrepancy in magnitude among studies. In all samples, a small Curie tail was observed. This can be due to small (~572 ppm) inclusions of free spin ½ ions arising from defect Co or Rh ions. As shown in figure 6.4, the addition of In to the Co_4Sb_{12} and Rh_4Sb_{12} increases the temperature independent susceptibility. Adding In leads to a T-

independent shift in $\chi(T)$ in the Co system of ~0.00003 emu/mol-Co and ~0.00004 emu/mol-Rh in the Rh system.

If we assume that the change in the temperature-independent $\chi(T)$ is due purely to a change in the density of electronic states upon doping with In, then $\Delta\chi$ (doped – undoped χ) is equal to the Pauli susceptibility, χ_{Pauli}. The γ-term from $C(T)$ and χ_{Pauli} are related by the density of states, whence the relation

$$\gamma = \frac{\pi^2 {k_B}^2}{3{\mu_B}^2}\chi_{Pauli}. \quad (6.2)$$

Given our χ(T) data, one would expect a γ of 2.395 mJ/mol-K^2 for the Co system and of 3.176 mJ/mol-K^2 for the Rh system. These values are somewhat consistent with our measured γ-value for 3.691 mJ/mol-K^2 for $In_{0.1}Co_4Sb_{12}$, but much less than the 11.154 mJ/mol-K^2 for $In_{0.1}Rh_4Sb_{12}$. The large discrepancy between the result of eqn. 6.2 and our measured result for the latter compound may stem from a γ-term enhancement from spin fluctuations, as mentioned above.

Measurements of $S(T)$ and $\rho(T)$ were also performed on the samples. Previous studies have shown that Co_4Sb_{12} is a narrow-gap semiconductor while Rh_4Sb_{12} is a semi-metal, also known as a zero-gap semiconductor (Wojciechowski 2007, Pardo, Smith et al. 2012). While the former may have either p- or n-type carriers, depending on the synthesis method, the latter is generally p-type (Morelli, Caillat et al. 1995, Wojciechowski 2007). Because our samples were hot-pressed, however, our Co_4Sb_{12} samples are n-type (Sharp, Jones et al. 1995). From the $\rho(T)$

and $S(T)$ curves (figures 6.5 & 6.6), the behavior of Co_4Sb_{12} is consistent with gapped transport mediated by electrons. Rh_4Sb_{12}, however, demonstrates a weak increase in $\rho(T)$ with lowered temperatures, suggesting zero-gap behavior, in agreement with previous band structure calculations (Takegahara and Harima 2003, Pardo, Smith et al. 2012). Filling Co_4Sb_{12} with In appears to close the gap, as $d\rho/dT$ becomes positive.

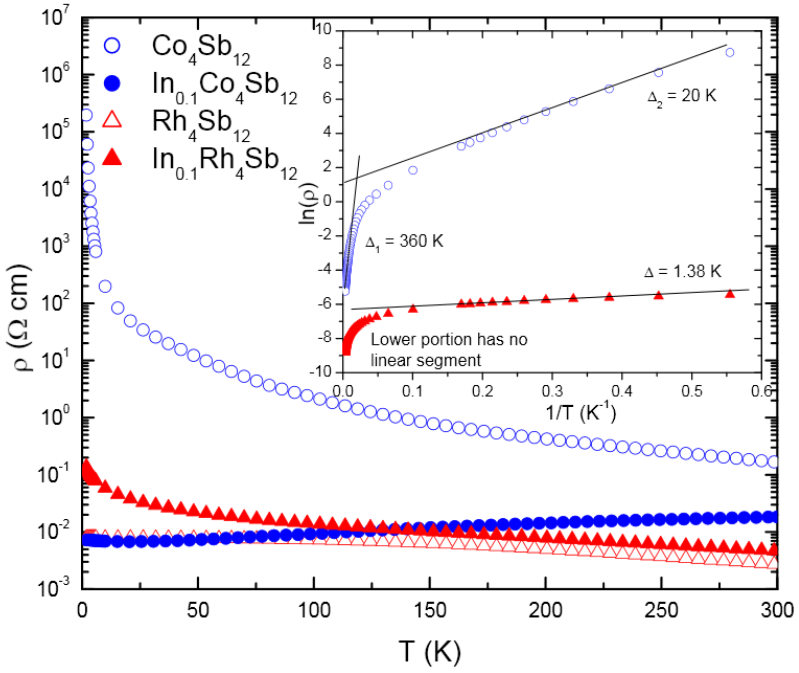


Figure 6.5: Temperature dependence of the sample resistivities. The inset shows and Arrhenius plot of the two semiconducting samples, Co_4Sb_{12} and $In_{0.1}Rh_4Sb_{12}$, from which the activation energies can be extracted.

Meanwhile, the opposite occurs for In-doping in Rh_4Sb_{12}. As shown in figure 6.5, $\rho(T)$ for Rh_4Sb_{12} has a weak temperature dependence that nearly plateaus below 150 K, but generally shows a negative $d\rho/dT$. The plateau may be related to Weyl-

semimetal behavior, as seen in other purported topological materials, and could clarified by future magnetoresistance measurements (Tafti, Gibson et al. 2016). Upon incorporation of In, this plateau is replaced with a slight semiconducting divergence, thus indicating that additional n-type carriers from the In inclusions alters the band structure by allowing a gap to form and raises the fermi level into the gap.

The change in behavior seen in $\rho(T)$ is also reflected in $S(T)$, where the addition of In in Rh_4Sb_{12} induces a sign change from p-type to n-type, as seen in previous studies (Eilertsen, Li et al. 2011). In both $In_{0.1}Co_4Sb_{12}$ and $In_{0.1}Rh_4Sb_{12}$, the In filler atoms act as electron donors, which leads to a decreased $\rho(T)$ in Co_4Sb_{12} and n-type activated behavior in Rh_4Sb_{12}. The Arrhenius law was used to determine the activation energies of the two semiconducting materials, Co_4Sb_{12} and $In_{0.1}Rh_4Sb_{12}$. The Co_4Sb_{12} curve yields Δ-values of 20 K and 360 K, while the $In_{0.1}Rh_4Sb_{12}$ plot yields only one low-T Δ-value (1.38 K) due to the small size of the gap relative to the thermal energy for T > 5 K. Additionally, the $In_{0.1}Rh_4Sb_{12}$ is more resistive than the Rh_4Sb_{12} due to impurity scattering effects from the introduction of In (Eilertsen, Li et al. 2011).

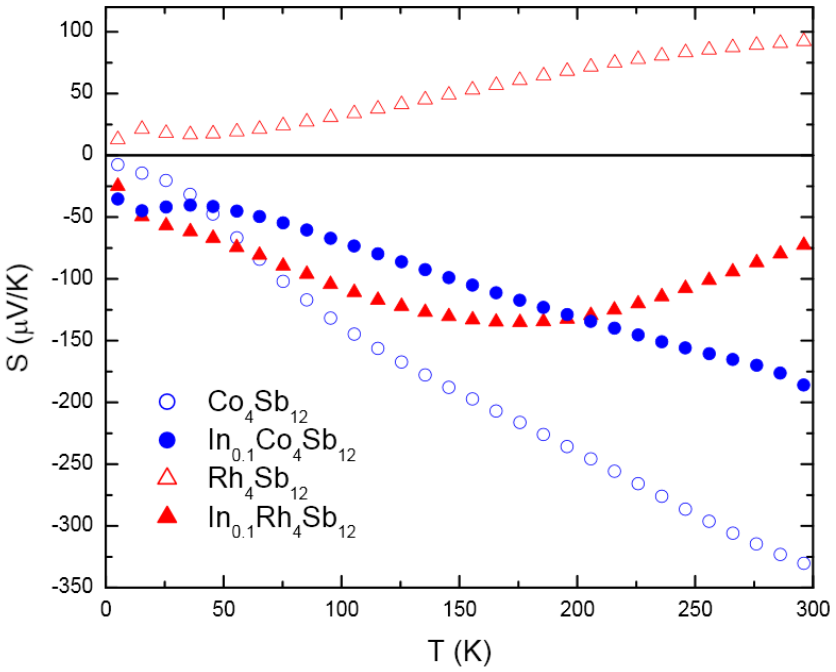


Figure 6.6. Seebeck coefficients as a function of temperature.

From figure 6.6, it can be seen that $S(T)$ in Co_4Sb_{12} is roughly linear and increasing with temperature, a behavior that is generally associated with metallic character, but has previously been attributed to its unique linear band structure (Singh and Pickett 1994). The $In_{0.1}Co_4Sb_{12}$ behaves similarly, but is smaller in magnitude and remains monotonically increasing with temperature. The change in sign of the derivative for the $In_{0.1}Rh_4Sb_{12}$ curve indicates the decrease of n-type carriers with increasing temperature, as $S(T)$ approaches positive values, and eventually reaches the same value as unfilled Rh_4Sb_{12} (Eilertsen, Li et al. 2011). Thus, the effects of the In dopants are most pronounced at low-T.

4. Conclusion

In summary, we have measured transport and magnetic properties of In-filled Co_4Sb_{12} and Rh_4Sb_{12}. While Co_4Sb_{12} is a narrow-gap semiconductor, $In_{0.1}Co_4Sb_{12}$ seems to behave as a zero-gap semiconductor, indicating that the In acts as an electron donor, while the inclusion of In in Rh_4Sb_{12} opens a gap. This information may prove useful in future studies of doped skutterudites, especially for low-T TEC applications. Additionally, these materials have been predicted to be nearly topological (Pardo, Smith et al. 2012), and we have seen hints of the linear bands in our $C(T,H)$ and $\rho(T)$ measurements.

Chapter VII: Magnetic ground states of the rare earth tripod kagome lattice

1. Introduction

The two-dimensional kagome lattice magnet (KLM) has been a favorite in the theoretical condensed matter community since the experimental work on SCGO (Ramirez, Espinosa et al. 1990), due to the strong frustration associated with its network of corner-shared triangles. Many exotic states are predicted, such as the quantum spin liquid (QSL) state (Lecheminant, Bernu et al. 1997, Wen 2004, Balents 2010), the spin-orbital liquid state (Schaffer, Bhattacharjee et al. 2013), the kagome spin ice (KSI) state (Wills, Ballou et al. 2002), dipolar spin order (Maksymenko, Chandra et al. 2015), the Kosterlitz-Thouless (KT) transition (Zhao, Li et al. 2013), quantum order by disorder (Sachdev 1992), nematicity, and supernematicity (Picot and Poilblanc 2015). The large variety of exotic states predicted lies in contrast to a paucity of experimental systems. Early efforts include the exploration of langasites $RE_3Ga_5SiO_{14}$ (Bordet, Gelard et al. 2006, Zhou, Vogt et al. 2007, Zorko, Bert et al. 2008), which possess distorted kagome lattices. Recent attention has been paid to vesignieite $BaCu_3V_2O_8(OH)_2$ (Okamoto, Yoshida et al. 2009) and herbertsmithite $ZnCu_3(OH)_6C_{l2}$ (Han, Helton et al. 2012), the latter of which shows intriguing signs of QSL behavior. From a materials standpoint, however, these two systems are limited by (i) known defect-prone structures (Lee, Kikuchi et al. 2007, Okamoto, Yoshida et al. 2009) and (ii) the inability to substitute facilely on the magnetic site (e.g., with non-Heisenberg spins) to realize states other than the QSL.

Clearly then, finding new KLM-containing compounds with spin-type variability is a challenge of the highest order.

Intriguingly, a 2D KLM is naturally contained in the frustrated 3D pyrochlore structure. In pyrochlores $RE_2X_2O_7$ (RE=rare earth element, X=transition metal element), both the RE^{3+} and X^{4+} sublattices form alternating kagome and triangular layers along the [111] axis as a result of corner-shared tetrahedrons (fig. 7.1a) (Tabata, Kadowaki et al. 2006). However, the strong interlayer interaction enforces three dimensionality. An exception is found in studies of $Dy_2Ti_2O_7$ in a [111] magnetic field, which polarizes the triangular layer spins, effectively decoupling the kagome planes, leading to a KSI state (Tabata, Kadowaki et al. 2006).

Obviously, if one can remove the magnetic moment of the triangular layers in the pyrochlore lattice, a RE-kagome-only lattice might be realized, enabling the study of intrinsic kagome physics. Because of various spin and spin anisotropies of different RE^{3+} ions, exotic and rich magnetic properties should be immediately available via the complex interplay among the spin-orbital coupling, dipolar and exchange interactions. In pyrochlores, for example, this interplay leads to multi-*k* ordering (Champion, Wills et al. 2001) with multiple field-induced transitions (Ramirez, Shastry et al. 2002) for Heisenberg spins in $Gd_2Ti_2O_7$, spin ice state (Bramwell and Gingras 2001) for Ising spins in $Ho_2Ti_2O_7$ (Harris, Bramwell et al. 1997) and $Dy_2Ti_2O_7$ (Ramirez, Hayashi et al. 1999), and quantum order by disorder

physics in the XY spin system $Er_2Ti_2O_7$ (Savary, Ross et al. 2012). Then, what will be the magnetic ground states in the RE-based KLMs?

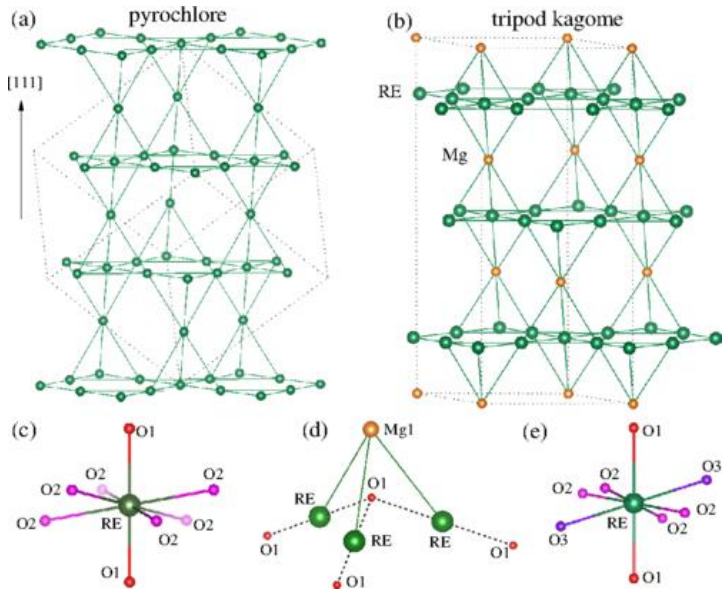


Figure 7.1: (a) Alternating kagome and triangular layers in a pyrochlore lattice. (b) Alternating RE-kagome and Mg-triangular layers in a TKL. Dashed lines indicate a single unit cell. Local oxygen environments around RE^{3+} for (c) pyrochlore and (e) TKL. (d) A single "tripod." Dashed lines represent Ising axes.

We have created such a KLM: $Mg_2RE_3Sb_3O_{14}$ based on partial ion substitution in the pyrochlore lattice. Here, the triangular layers in the pyrochlore structure are occupied by nonmagnetic Mg^{2+} ions, leaving the RE^{3+}-kagome layer well isolated from neighboring layers. We studied three representative systems (RE=Gd,Dy,Er) by dc and ac susceptibility (χ_{dc}, χ_{ac}) and specific heat ($C(T)$) measurements. We present a spin Hamiltonian and show the fundamental differences in collective behavior between the 2D KLMs and their 3D pyrochlore cousins.

2. Experimental methods

Polycrystalline samples of tripod kagome lattice (TKL) compounds $Mg_2RE_3Sb_3O_{14}$ (RE = Gd, Dy, Er) were synthesized by solid state reactions. Stoichiometric ratios of RE_2O_3 (RE = Gd, Dy, Er), MgO, and Sb_2O_3 powder were carefully ground and reacted at a temperature of 1573 K for 60 hours with several intermediate grindings. Performing the reaction at temperatures above 1623 K will introduce site-disorder between the RE site and the Mg site, which is evidenced by the cubic pyrochlore phase in X-ray diffraction (XRD) patterns. The room temperature XRD patterns were measured with a HUBER X-ray powder diffractometer with the structural refinements performed using software package *Fullprof-suite*.

The dc susceptibility measurements were performed using a commercial superconducting interference device (SQUID) magnetometer with a magnetic field of 200 Oe. The ac susceptibility was measured via the conventional mutual inductance technique at frequencies between 80 Hz and 700 Hz. The low temperature specific heat measurements were performed in a He_3-He_4 dilution refrigerator using the semi-adiabatic heat pulse technique. The powder samples were cold-sintered with Ag powder, the contribution of which was measured separately and subtracted from the data. For all the specific heat data shown below, the magnetic contribution (C_{mag}) was obtained by subtracting a lattice contribution estimated from the results of a separate measurement of the non-magnetic isomorph $Zn_2La_3Sb_3O_{14}$.

3. Structure

$Mg_2RE_3Sb_3O_{14}$ (RE=Gd,Dy,Er) has a rhombohedral structure with R-3m space group. Compared with the pyrochlore lattice, the triangular layers of both RE^{3+} and Sb^{5+} sublattices in the KLM structure are occupied by Mg^{2+} (the Mg^{2+} site can be replaced by Co^{2+} (Li, Hu et al. 2014), Mn^{2+} (Fu and Ijdo 2014), Zn^{2+} (Sanders, Krizan et al. 2016)). Thus, the chemical formula can also be written as $(Mg_{0.25}RE_{0.75})_2(Mg_{0.25}Sb_{0.75})_2O_7$, which is a pyrochlore ($RE_2X_2O_7$) with ¼ RE^{3+} and X^{4+} ions substituted in an ordered manner (fig. 7.1b). It is noteworthy that for the x-ray diffraction pattern of $Mg_2RE_3Sb_3O_{14}$ (see supplementary material in (Dun, Trinh et al. 2016)), the strongest peak for pyrochlore at $2\theta\sim30°$ disappears completely and splits into two peaks, providing evidence for the absence of Mg-RE or Mg-Sb site disorder (Fu and Ijdo 2014). As shown below, the $C(T)$ peaks at their phase transitions are very sharp, further underscoring the high degree of site order in the kagome layers. This good kagome layer separation is likely due to the large ion size difference between Mg^{2+} and RE^{3+}. In this structure, the nearest-neighbor distance between the RE^{3+} ions within a kagome layer remains similar to that of its pyrochlore cousin, and the RE^{3+}-kagome layers are well isolated from each other by the nonmagnetic Mg^{2+}, Sb^{5+} layers. Take $Mg_2Gd_3Sb_3O_{14}$, for example. The nearest Gd-Gd distance within a kagome layer (3.678 Å) is similar to that in $Gd_2Ti_2O_7$ (3.600 Å), and much smaller than that between different planes (6.162 Å). Since the dipolar

energy goes as $1/r^3$, this leads to interlayer energies an order of magnitude smaller than intralayer energies. Thus, the kagome lattice in $Mg_2RE_3Sb_3O_{14}$ is seemingly free of structural defects.

In pyrochlore $RE_2X_2O_7$, one important structural feature is that each RE^{3+} ion is surrounded by eight oxygens (fig. 7.1c) with two shorter RE-O1 bonds lying along the local-[111] axis and six longer RE-O2 bonds forming a puckered ring. This feature defines the crystal electric field (CEF) and the gfactor, which determines the ionic anisotropy for the RE^{3+} spins. In $Mg_2RE_3Sb_3O_{14}$, this local oxygen coordination is largely preserved. The RE ion is still surrounded by eight oxygens with the two shortest RE-O1 bonds that remain lying along the local-[111] axis (fig. 7.1e). The difference is that the longer six RE-O bonds are divided into two sets: four longest RE-O2 bonds and two intermediate RE-O3 bonds (Dun, Trinh et al. 2016). Since the CEF degeneracy has already been lifted by the pyrochlore-like anisotropy for an effective spin- 1/2 system, the dominant anisotropy remains the one distinguishing the puckered ring from the local-[111] oxygens, making this in-plane anisotropy most likely irrelevant for the ground state degeneracy.

Given the high degree of site order, the large difference in separation between intraplane and interplane RE ions, it is appropriate to consider this a well-formed kagome structure. In addition, the CEF-driven single ion anisotropy, which is vestigial from the parent pyrochlore structure, defines directions for either the Ising spins or the XY-spin normal vectors that are neither uniaxial nor uniplanar. This

particular situation of three distinct axes with specific interaxes angles will be important for understanding ordered spin configurations, as we show below. Given the uniqueness of this structure and the need to distinguish it from KLMs with undefined local anisotropy, we call this the "tripod kagome lattice" (TKL), inspired by a "tripod" formed by three RE^{3+} and one Mg^{2+} ion (fig. 7.1d).

4. Magnetic properties

For $Mg_2Gd_3Sb_3O_{14}$, a Curie-Weiss (CW) fit from 50–300 K of $1/\chi_{dc}$ (fig. 7.2a) yields a Weiss temperature, $\theta_W = -7.35$ K, and an effective magnetic moment, $\mu_{eff} = 7.91\ \mu_B$. The negative θ_W is close to that of $Gd_2Ti_2O_7$ (θ_W = -11.7 K) (Bramwell, Field et al. 2000). The μ_B value is consistent with $\mu_{eff} = 7.94\ \mu_B$ expected for Gd^{3+} ($^8S_{7/2}$). With measurement frequencies ranging from 80 to 700 Hz, χ_{ac} shows a sharp and frequency-independent peak at T_N = 1.65 K (fig. 7.2b), indicating a long-ranged order (LRO) transition. This transition is further confirmed by a sharp peak at the same temperature in magnetic specific heat $C_{mag}(T)$ (fig. 7.2c). The magnetic entropy below 6 K is 17.16 J/(mol Gd) K (Dun, Trinh et al. 2016). This value is close to $R\ln(2S+1) = 17.29$ J/mol K for a S = 7/2, indicating a complete LRO among the Gd^{3+} spins.

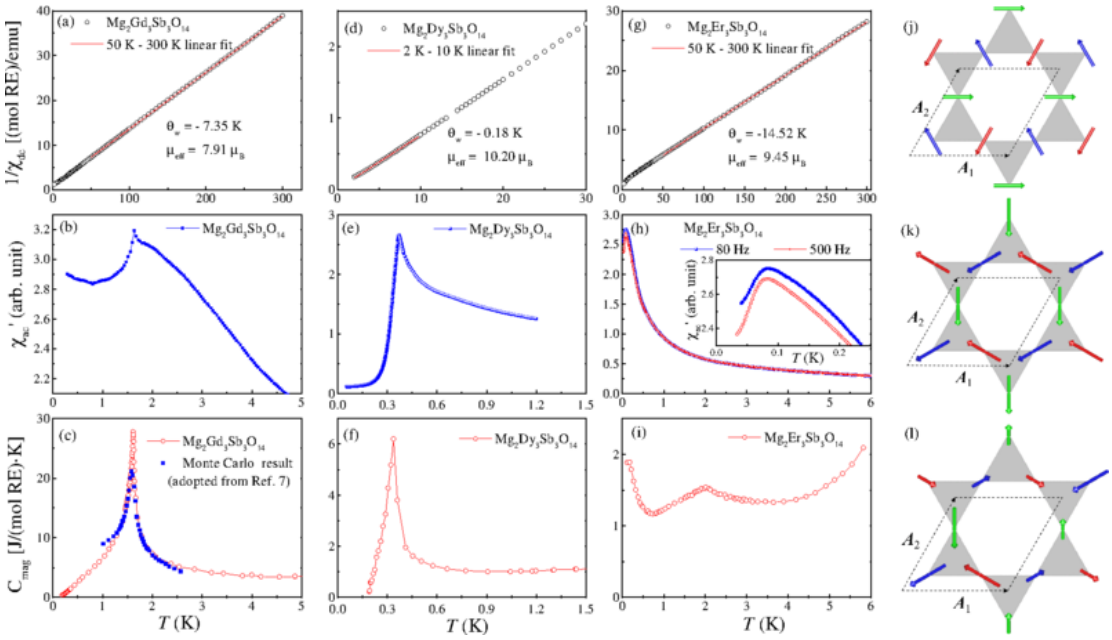


Figure 7.2: (a)-(i) Temperature dependence of the inverse χ_{dc}, real part of the χ_{ac}, and magnetic specific heat C_{mag} for $Mg_2RE_3Sb_3O_{14}$. The blue dot in (c) is the Monte Carlo simulation result adopted from (Maksymenko, Chandra et al. 2015) with scaling. (j) the 120° LRO state for $Mg_2Gd_3Sb_3O_{14}$ and $Mg_2Er_3Sb_3O_{14}$. The dashed lines represent a unit cell. (k) The $\boldsymbol{k} = 0$ LRO state and (l) the $\boldsymbol{k} = (1/3,2/3)$ spin-density-wave-like state for $Mg_2Dy_3Sb_3O_{14}$.

For $Mg_2Dy_3Sb_3O_{14}$, the CW fit below 10 K yields $\theta_W = 0.18\ K$ and μ_{eff}=10.20 μ_B (fig. 7.2d), consistent with the free ion moment of 10.63 μ_B for Dy^{3+} ($^6H_{15/2}$). In $Dy_2Ti_2O_7$ (Bramwell, Field et al. 2000), the small θ_W (-0.20 K) is due to competition between the dipolar interaction and superexchange couplings of Dy ions. Here, the similarity in local structure translates into similar-size coupling to the pyrochlore case, since the total spin-spin coupling is dominated by the dipolar interaction. With the ferromagnetic dipolar interaction, the negative θ_W again shows the antiferromagnetic nature of the exchange interactions in $Mg_2Dy_3Sb_3O_{14}$. A

transition to LRO at T_N = 0.37 K is observed in both the χ_{ac} (fig. 7.2e) and $C_{mag}(T)$ (fig. 7.2f). The integrated magnetic entropy below 6 K is 5.38 J/(mol Dy)K (Dun, Trinh et al. 2016), which is close to $R\ln 2 = 5.76$ J/(mol Dy) K, as expected for a Kramers doublet. This suggests that the Dy^{3+} spins fully order below 0.37 K.

For $Mg_2Er_3Sb_3O_{14}$, the CW fit above 50 K yields $\theta_W = -14.25$ K, and μ_{eff} = 9.45 μ_B (fig. 7.2g), consistent with the free ion moment of μ = 9.58 μ_B for Er^{3+} ($^4I_{15/2}$). The value for θ_W is close to that of the pyrochlore $Er_2Ti_2O_7$ (θ_W = -15.93 K (Bramwell, Field et al. 2000)). The χ_{ac} was measured down to 30 mK with a broad peak observed around 80 mK (fig. 7.2h), which shows weak frequency dependence. The $C_{mag}(T)$ was measured down to 120 mK and exhibits a weak and broad peak around 2 K (fig. 7.2i). At this temperature, no anomaly is observed in χ_{ac}, while an extremely weak anomaly (2×10^{-8} emu/(mol Er)) was seen in χ_{dc} at 2.1 K, which is perhaps related to the weak $C_{mag}(T)$ peak.

5. Theoretical investigation and discussion

The three systems discussed here, Gd, Dy, Er, are likely representatives of the three different spin types, Heisenberg, Ising, and XY, respectively, as evidenced by similar low temperature magnetization curves compared with their pyrochlore

cousins (Dun, Trinh et al. 2016). In the pyrochlore systems discussed above, each spin type yields significantly different behavior. To uncover the possible differences among the spin types in the TKLs, we have used a Luttinger-Tisza-type theory (Onsager 1939, Luttinger and Tisza 1946) and studied the eigenvalues and eigenfunctions of the interaction matrix in wave vector space. We construct a 2D kagome lattice with $\boldsymbol{A}_1$ and $\boldsymbol{A}_2$ as basis vectors of the triangular Bravais lattice where there are three basis sites in a unit cell, labeled as blue, red, and green (fig. 7.2j). Thus, the general Hamiltonian for the TKL can be written as (Dun, Trinh et al. 2016)

$$H = \frac{1}{2}\sum_{k,\alpha,\beta,a,b} S^{\alpha,a}(k)\, S^{\beta,b}(-k) V_{ab}^{\alpha\beta}(k), \tag{7.1}$$

where V is the sum of a dipolar part, exchange part, and a single ion anisotropy part dictated by the CEF effects. Here, α and β are the Cartesian indices of the spins and a, b run over the three basis sites in unit cell. The spin vector is the Fourier component of the real space object, and k runs over the Brillouin zone of the triangular lattice. Thus, for a given value of k, V is a 9×9 matrix that can be easily diagonalized. The dipolar part (D_{nn}) is fixed exactly by the effective moment of spin and RE-RE distances, while the exchange (J_{ex}) and single ion terms are found from the θ_W and the CEF splitting of the RE^{3+} in the given environment (Dun, Trinh et al. 2016).

The $Mg_2Gd_3Sb_3O_{14}$ has Heisenberg spins ($J = 7/2,\ L = 0$) and therefore no single ion term. The θ_W of -7.35 K leads to an estimate of the exchange constant J_{ex}

~ 6.10 K, while the dipolar energy scale of nearest-neighbor spins $D_{nn} \sim 0.79$ K (Dun, Trinh et al. 2016). We found that the minimum eigenvalue of V is at the Brillouin zone (BZ) center with $k = 0$, and the corresponding eigenvector represents a 120° state where the three spins in the unit cell lie in the plane pointing along three axes at angles $2\pi/3$ to each other (fig.7.2j). Here, the large dipolar term breaks the rotation invariance, lifts the frustration of a kagome lattice, and helps defeat the Mermin-Wagner theorem for a 2D Heisenberg lattice. It is known that higher values of spin than 1/2 releases the frustration somewhat like soft spins would (Nagai, Miyashita et al. 1993), and the case here has $S = 7/2$. This seems to enable a 2D-Ising-like transition with a logarithmic heat capacity in the style of Onsager. Actually, similar spin structure was predicted by Maksymenko *et al.* by considering classical dipoles on a kagome lattice (Maksymenko, Chandra et al. 2015). Their calculated specific heat agrees well with our experiment in the critical region by proper scaling (fig. 7.2c). Thus, we conclude $Mg_2Gd_3Sb_3O_{14}$ to be a rare example of dipolar interaction mandated spin ordering on a kagome lattice.

The Dy^{3+} ion is an effective spin- 1/2 Kramers ion with Ising anisotropy in an eight-oxygen-surrounding environment. Similar to the spin ice system, the Ising axis in the $Mg_2Dy_3Sb_3O_{14}$ variant is along the lines joining each Dy to O1 (dashed lines in fig. 7.1d). For the three sites in our Bravais lattice, the Ising directions are $\vec{\eta}_{blue} = \frac{1}{\sqrt{5}}[\sqrt{3}, 1, 1]$, $\vec{\eta}_{red} = \frac{1}{\sqrt{5}}[-\sqrt{3}, 1, 1]$, and $\vec{\eta}_{green} = \frac{1}{\sqrt{5}}[0, -2, 1]$ in the global Cartesian frame. The small θ_W of -0.18 K corresponds to $J_{ex} \sim 1.12$ K, while the dipolar

energy scale $D_{nn} \sim 1.31$ K (Dun, Trinh et al. 2016). It is known that ferromagnetic spins with tripod-like anisotropy on a kagome lattice are highly frustrated, which will lead to the KSI state (Wills, Ballou et al. 2002). Similar to that of the pyrochlore spin ice (Ramirez, Hayashi et al. 1999, Bramwell and Gingras 2001), the ice rule (spins with either two-in–one-out or one-in–two-out with respect to the center of each triangle) of KSI will also result in a large number of ground state degeneracy and zero-point entropy (Wills, Ballou et al. 2002).

With the TKL and strong dipolar interaction, it is tempting to view $Mg_2Dy_3Sb_3O_{14}$ as a realization of a dipolar ferromagnet where the KSI physics could be realized. Our Luttinger-Tisza method yields a metastable state at the BZ center, which is an ordered KSI state. The corresponding spin structure (fig. 7.2k) can be viewed as a three-sublattices ferromagnetic order with $k = 0$. This spin structure also resembles the theoretically predicted LRO state (Siddharthan, Shastry et al. 1999, Melko, den Hertog et al. 2001, Siddharthan, Shastry et al. 2001) for the 3D pyrochlore spin ice observed in $Tb_2Sn_2O_7$ (Mirebeau, Apetrei et al. 2005). However, this $k = 0$ state is *not* a global ground state. The lowest eigenvalue of the exchange matrix is found to be at the six K points of BZ corners, whose energy is somewhat lower than that of the zone center. Such an eigenvalue corresponds to a LRO state with a 3×3tripled magnetic unit cell. In addition, the magnitude of the moment differs in space, as prescribed by a commensurate spin density wave state. Unlike the $k = 0$ state where the KSI ice rule is preserved for every Mg-Dy tetrahedron (gray triangle

in fig. 7.2k), here, one out of six tetrahedrons violates the local ice rule. Note that the Luttinger-Tisza method used here is more akin to the mean-field theory when applied away from the zone center or the M point of the BZ. This is a nontrivial and complex problem (see, e.g., refs. (Takagi and Mekata 1993, Takagi and Mekata 1995)) and requires further theoretical investigation. Regardless of the exact nature of ordering, our TKL system then appears to enable the spin dynamics to be much more efficient, as compared to the 3D $Dy_2Ti_2O_7$ compound. This interesting contrast therefore provides a strong impetus to the study of the underlying dynamics. Along with the observed LRO at 0.37 K, the Dy-Ising TKL provides a rare example exhibiting a LRO state that breaks the KSI degeneracy.

The Er^{3+} ion in $Mg_2Er_3Sb_3O_{14}$ has a large angular momentum $J = 15/2$. At low temperatures, it reduces to an effective spin- 1/2 as a result of the Kramers doublet. The high temperature $\theta_W \sim -14.52$ K implies a large exchange energy $J_{ex} \sim 11.0$ K, while the dipolar energy scale is $D_{nn} \sim 0.11$ K by assuming a moment of 3 μ_B (Dun, Trinh et al. 2016) (similar to that in the Er pyrochlore). This implies that below ~10 K the spins are locked up into the state preferred by the exchange. The CEF in this case gives rise to a local XY model, where the Er^{3+} are energetically favorable to lie in the local XY plane perpendicular to the Ising axis discussed above. In the Er pyrochlore, such an XY model will give rise to a $U(1)$ degeneracy in the spin Hamiltonian at the mean-field level that allows the Er^{3+} spins to rotate continuously in the XY plane (Savary, Ross et al. 2012). In Er TKL,

similar XY degeneracy is preserved for the exchange part of the Hamiltonian. However, an arbitrarily small long-range dipolar interaction will break the degeneracy. By diagonalizing the interacting matrix, a lowest energy eigenvalue is found at the BZ center whose eigenvector, by a curious coincidence, corresponds to the coplanar model exactly the same as that of the Gd compound (fig. 7.2j).

Regarding the experimental observations for the Er TKL, since the 2.1 K anomaly in $C(T)$ is extremely weak in terms of the entropy under the peak, and χ_{dc} shows a similarly weak anomaly, the order parameter might be one that still allows significant fluctuations below its T_c, reminiscent of a KT transition (Kosterlitz and Thouless 1973) where spin vortices form and bind. Then the 80 mK transition shown on χ_{ac} is likely related to the predicted 120° coplanar antiferromagnetic ordering. If so, such a low ordering temperature (frustration index $f = (\theta_W/T_N) \sim 180$) suggests the importance of quantum spin fluctuations in terms of suppressing the ordering temperature and selecting the ordered state. The weak frequency dependence on χ_{ac} around the peak might indicate an increasing spin lattice relaxation time as temperature is decreased. The importance of thermal coupling between a coherent spin system and the lattice needs to be understood for both identifying and potentially using quantum materials (Schmidt, Silevitch et al. 2014). Future experiments including neutron scattering and muon spin spectroscopy will be useful to identify the nature of the two transitions at 80 mK and 2.1 K.

6. Summary

We discovered a new 2D rare-earth TKL $Mg_2RE_3Sb_3O_{14}$ by partially substituting the ions in the cubic pyrochlore lattice. Our studies on three samples with RE=Gd,Dy,Er have already related their magnetism to various exotic states including the dipolar spin order, the KSI, and the KT transition. Because of the large variability of the spin sets in the rare-earth family and the possibility of tuning the lattice parameters via chemical pressures, other exotic physics might also be realized. Future exploration of the whole TKL family members is expected to open a new field in condensed matter physics and materials science studies for coming years, such as the pyrochlore did during the past two decades.

Chapter VIII: Concluding remarks and outlook

In studies of collective behavior in compounds with only light elements, the effects of SOC are relegated to small corrections. As we know from rare earth magnetism, heavy fermion physics, and the development of TIs and SOMIs, SOC can play a pivotal role in physical property determination. Recent developments in topological Dirac materials have brought SOC to the forefront of materials design elements, on par with the Coulomb interaction, bandwidth, and exchange coupling. A wealth of phenomena exist in regions of "materials phase-space" where these energy scales overlap.

In this dissertation, we have explored a variety of novel effects that are ultimately related to large SOC, including:

- The angular-dependent magnetic susceptibility in URu_2Si_2, where the near-perfectly Ising g-factor supports the hastatic order scenario, wherein strong spin-orbit coupling gives rise to U $5f^2$ states that pass on their Ising-like character to the hybridized quasiparticles;
- The transport properties of $FeSb_2$, where an anomalous proportionality between $S(T)$ and $\mu_H(T)$, as seen in multiple studies, argues against a simple phonon drag picture, and instead suggests a more fundamental mechanism;
- The positive linear magnetoresistance in $BaIrO_3$, which we attribute to quantum interference effects related to the quasi-one-dimensional structure and competing energy scales;

- The effects of In-doping on the transport properties of $CoSb_3$ and $RhSb_3$, which have both been predicted to be close to a topological transition;
- The novel rare earth tripod kagome materials, which will allow for the study of intrinsic kagome lattice behavior, and for which we have already shown a host of interesting magnetic states.

As indicated by this work, materials with strong SOC will continue to be a hotbed of new physics for the foreseeable future, both fundamentally and for technological applications.

Appendices

A. Van der Pauw LabVIEW program

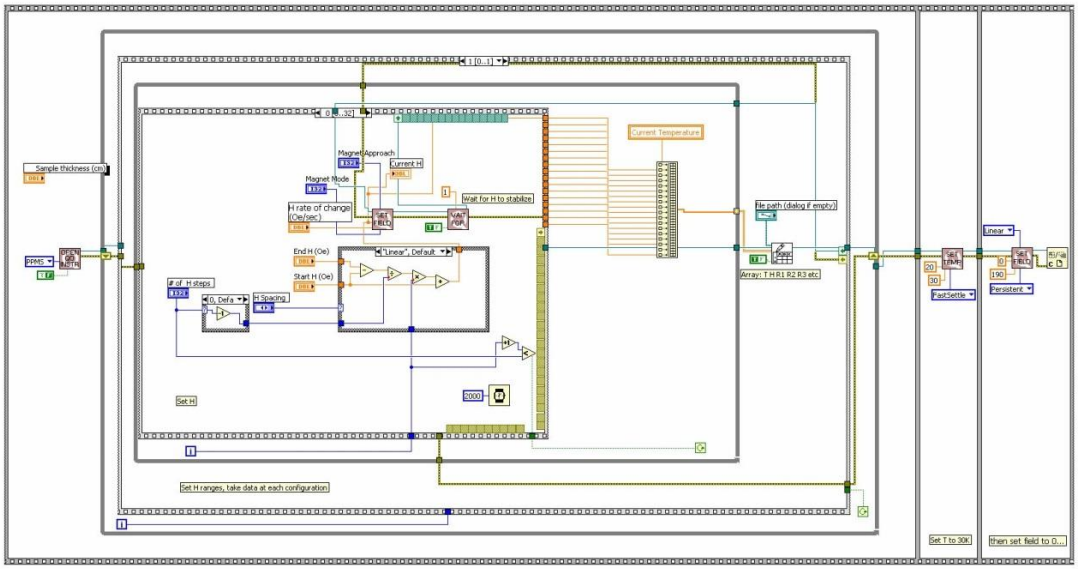


Figure A.1: LabVIEW block diagram for the vdP automation program corresponding to figure 2.3 and the discussion in Chapter 2.1.b.

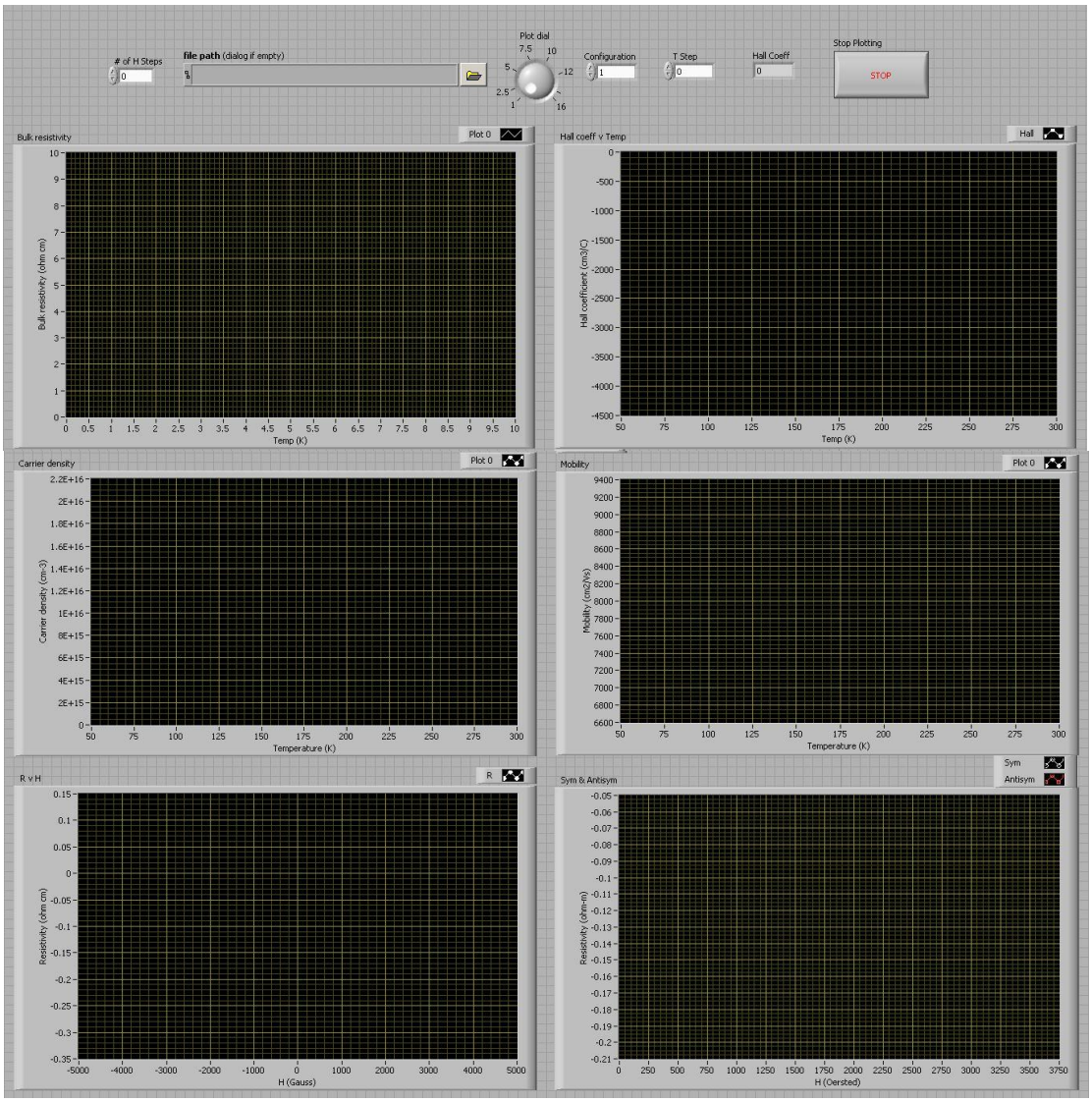


Figure A.2: Main window for the vdP analysis program. A data file from the vdP automation program (figure A.1) is loaded and the data are analyzed via the vdP equation.

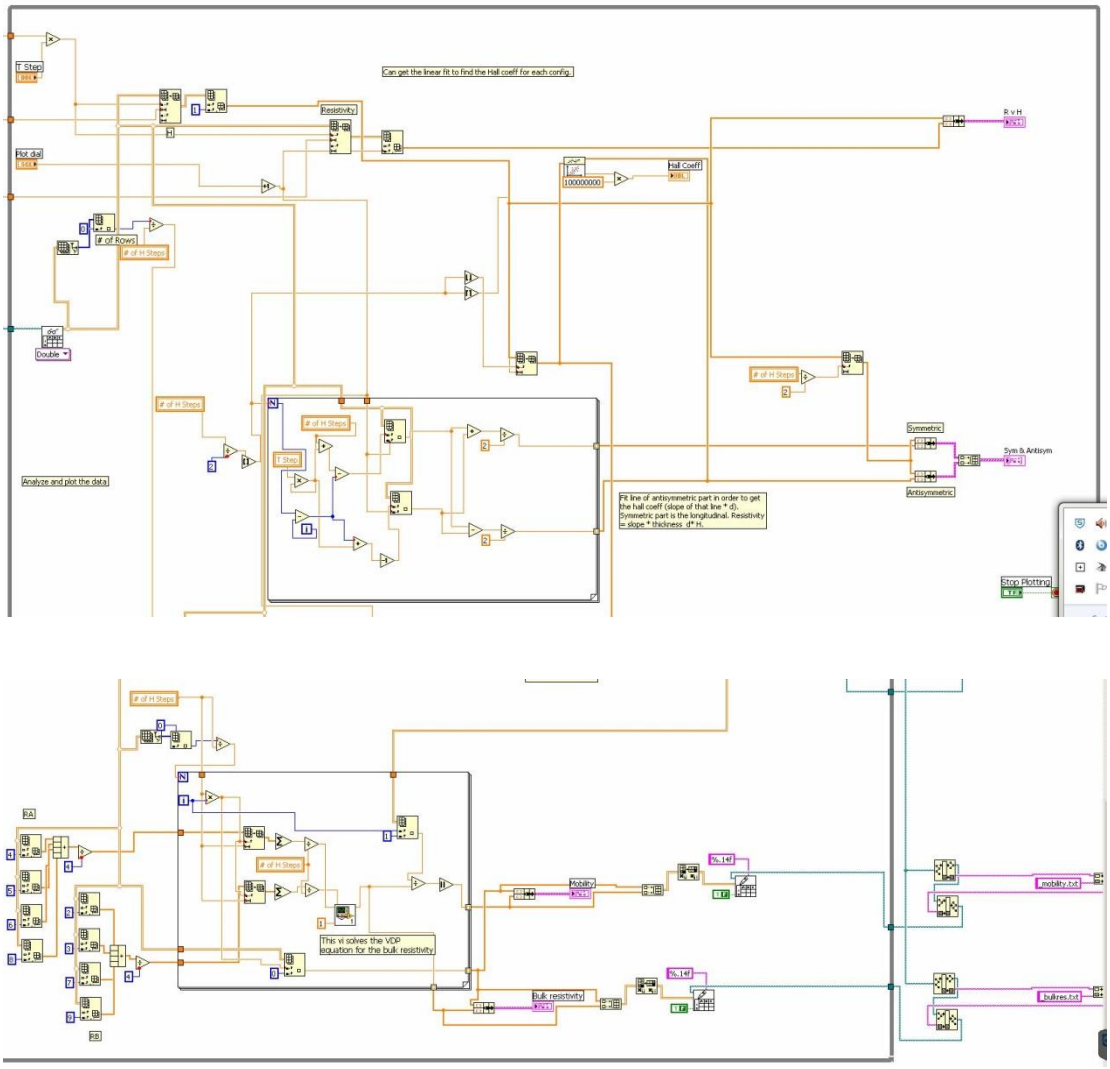


Figure A.3: Block diagram for the vdP analysis program (figure A.2)

B. Thermopower Visual Basic 6 program

```
'Thermopower Program (TPBT11)
'Original code modified from THCOND2 by D.W. Visser & A.P. Ramirez, June 1996
'Translated into VB6 by J. Trinh, Jan. 2015

‘Subroutines:
'POLYEVAL - evaluates a polynomial and its derivative at x (xx)

'Functions -
'TEMPDIFF(TEMP, dv) - given T in K and dv in μV, returns temperature difference
'ALPHA(TEMP) - returns Seebeck coefficient at T (in μV/K)

'Variable List:
'DEV10$ thru DEV16$ - GPIB device addresses
'AA() -  data array, differential thermocouple voltage
'ALAST() - 10 most recent data (for slope check)
'ANTLAST() - 10 next most recent (for slope check)
'ISPEED - time constant for LR700 autorange
'CURT, CURT$ - current values for Keithley in Amps
'CUROP - counter 0,1,2,... for output powers
'JPLT - plot index
'CURINC - multiplier value for current at succ. temps.
'CUROPLIM - number of power values per temperature
'STARTTEMP, ENDTEMP, DELTEMP - initial, final, delta temperature
'TEMP - setpoint temperature for PPMS
'EQUIL$ - contains "Y" resistors in equilibrium, "N" if not
'MES$ - message strings for GPIB built in this variable
'X$ - contains a carriage return to terminate some GPIB calls
'ICURSTRT - starting current in microAmps
'END$ - changes to "Y" when ENDTEMP is exceeded by TEMP

'*****************************************************************

Option Explicit
Dim mes As String, x As String, SCurt As String, XNAM As String
Dim h As Single, t As Single, t0 As Single, EQUIL As String
Dim dev10 As Integer, dev11 As Integer, dev12 As Integer, dev15 As Integer
Dim aa(600) As Single, ALAST(10) As Double, bb(600) As Single
Dim Curt As Double, curop As Integer, heatres As Integer
Dim c(1 To 10) As Single                    'Fit parameters for Seebeck coefficient
Dim P As Single, DP As Single, xx As Single, n As Integer        'PolyEval variables
```

```
Dim v As Single, temptol As Single, aprime As Single
Dim delv As Single, POWER As Single, yzero As Single, ybar As Single
Dim byzero As Single, bybar As Single, errzero As Single, sd As Single
Dim a As String * 16, b As String * 18
Dim dta As String * 44, tester As String, commaflag As Integer
Dim field As Single, TEMP As Single, Seebeck() As Single, counter As Integer,
Drifts() As Single
Dim temp1(500, 1), temp2(5000, 3)
Dim st As SYSTEMTIME, tm As Double, sleeptime As Integer, jplt As Integer,
JPLTLAST As Integer
Dim DriftA As String, DriftB As String, J As Integer
Dim curoplim As Integer, icurstrt As Long, icurend As Long, icurdel As Long
Dim STARTEMP As Single, endtemp As Single, deltemp As Single
Dim tcstart As Single, tcend As Single, tcdel As Single, i As Integer
Dim startfield As Integer, endfield As Long, delfield As Long
Dim trange1 As Integer, trange2 As Integer, vtol0 As Single, vtol1 As Single
Dim vtol2 As Single, tole0 As Single, tole1 As Single, tole2 As Single, v1 As Single,
v2 As Single
Dim fields As String, TEMPs As String, K As Single, L As Single
Dim BFLG As Integer, HFIELD As Long, tx As Single, delT As Single
Dim VTOL As Single, vmax As Single, xcurt As Single, averr As Single
Dim sx As Single, sy As Single, sxoss As Single, anzx As Single
Dim st2 As Single, chi2 As Single, SampS As Single
Dim doneflag As Integer, fieldtol As Integer, relaxloop As Integer
Dim fielder As Single, temper As Single, NMINUTES As Integer
Dim NREMAIN As Integer, t1 As Single, t2 As Single

Private Type SYSTEMTIME
 wYear As Integer
 wMonth As Integer
 wDayOfWeek As Integer
 wDay As Integer
 wHour As Integer
 wMinute As Integer
 wSecond As Integer
 wMilliseconds As Integer
End Type

Private Declare Sub GetSystemTime Lib "kernel32.dll" (lpSystemTime As
SYSTEMTIME)
Private Declare Sub GetLocalTime Lib "kernel32.dll" (lpSystemTime As
SYSTEMTIME)
```

```
Private Declare Function Beep Lib "kernel32.dll" (ByVal dwFreq As Long, ByVal
dwDuration As Long) As Long

'*********************************************************************
'Set Parameters of Measurements
'*********************************************************************
Private Sub Command1_Click()

'Initialize GPIB devices and assign unit descriptors
   Call ibdev(0, 10, 0, 13, 1, 0, dev10)   'HP3478, (Sample; pins 13,14)
   Call ibdev(0, 11, 0, 13, 1, 0, dev11)   'SYSTEM DVM, HP3457 (34401A)
‘(Reference Bi2Te3; pins 3,4 )
   Call ibdev(0, 12, 0, 13, 1, 0, dev12)   'KEITHLEY 220, HEATER CURRENT
‘SOURCE (resistor heater, pins 7,8)
   Call ibdev(0, 15, 0, 13, 1, 0, dev15)   'PPMS

'Initialize HP3457 for reading differential thermocouple (Reference Bi2Te3)
   mes = "*RST": Call ibwrt(dev11, mes) 'Reset
   mes = "*CLS": Call ibwrt(dev11, mes) 'Clear dmm status registers
   mes = "CONF:VOLT:DC .0005, 6.0": Call ibwrt(dev11, mes)
   mes = "VOLT:DC:NPLC 10": Call ibwrt(dev11, mes)
   mes = "DISP 1": Call ibwrt(dev11, mes)

'Setup Keithley 220 Current Source
   Curt = 0!: SCurt = CStr(Curt): curop = 0
   x = CStr(Chr(13))          'Carriage return
   mes = "F0X" & x            'Set to standby mode
   Call ibwrt(dev12, mes)
   mes = "B1L1D0X" & x        'Set buffer address and memory location; set display
to current source
   Call ibwrt(dev12, mes)
   mes = "I" & CStr(Curt) & "V20X" & x      'Set current source, voltage limit
   Call ibwrt(dev12, mes)
   Sleep 1000
   jplt = 0       ' PLOT INDEX

'Setup files for saving data
   XNAM = "C:\Users\PPMSWest\Dropbox\PPMS\Thermopower\" &
CStr(Text1.Text) & ".txt"
   DriftA = "C:\Users\PPMSWest\Desktop\VB6\Drifts\DriftA.txt"
   DriftB = "C:\Users\PPMSWest\Desktop\VB6\Drifts\DriftB.txt"
   Open DriftA For Output As #2
   Open DriftB For Output As #3
```

```
'Set parameters for measurement
   heatres = 100                                          'Heater resistance in ohms

'Number of Runs for each (T,H) value
   curoplim = 3       'No. of power values per temperature, >= 2!
   icurstrt = 4000    'In µA, only used for first test measurement
   icurend = 6000    'If curoplim = 1, then Delta V = 0.5*vtol

'Temperatures and Magnetic Fields
   STARTEMP = Text4.Text        'In K, startemp < endtemp required!
   endtemp = Text5.Text
   deltemp = Text6.Text       'Sign has to match with startemp and endtemp

   tcstart = Text4.Text
   tcend = Text5.Text
   tcdel = Text6.Text         'Sign has to match with tcstart and tcend

   startfield = Text7.Text
   endfield = Text8.Text
   delfield = Text9.Text   'Value <> 0 required, sign has to match with startfield and
endfield

'Extra Delay after establishing new temperature
   sleeptime = 2      ' time in Minutes

'Tolerance values:
'K variation allowed in temp, used in checkth
   'temptol = 0.1
   temptol = 0.05

'Maximum Delta V allowed on thermocouple with respect to V=alpha*T
   trange1 = 60
   trange2 = 40

   vtol0 = 0.01                 'For all other temperatures
   'vtol1 = 0.03                'For trange2 <= T < trange1
   'vtol2 = 0.06                'For T < trange2
   vtol1 = 0.01
   vtol2 = 0.01

'Maximum slope allowed on thermocouple voltage with respect to absolute
'value of this voltage
```

```
'Slope <= noise level is also regarded as equilibrium state
   tole0 = 0.0001                ' For all other temperatures
   'tole1 = 0.005                ' For trange2 <= T < trange1
   'tole2 = 0.05                 ' For T < trange2
   tole1 = 0.001
   tole2 = 0.001

For J = 1 To 60
  Sleep 1000
  Label2.Caption = CStr(60 - J) & " seconds until run begins"
  DoEvents
Next J

counter = 0

ControlLoop

End Sub


'*********************************************************************
'Start of Control Loop
'*********************************************************************
Private Sub ControlLoop()
'Debug.Print "ControlLoop"
  EQUIL = "N"
  BFLG = 0
  TEMP = STARTEMP
Do
    Call TEMPSET(TEMP)
    BFLG = 1
    If TEMP = STARTEMP Then BFLG = 0
  For HFIELD = startfield To endfield Step delfield
  Call FieldSet(HFIELD)

  VTOL = vtol0
    If TEMP < trange1 Then VTOL = vtol1
    If TEMP < trange2 Then VTOL = vtol2

    Call alpha2(TEMP, a, aprime)
    v1 = VTOL * a * TEMP              'Scales the vmax value based on
    v2 = VTOL * a ^ 2 / aprime        'tolerance value provided and the
    Debug.Print "v1 = " & CStr(v1) & "v2 = " & CStr(v2)
```

```
                                        ‘List of Seebeck coefficients (a)
   If v1 > v2 Then                      'provided from the fits below.
   vmax = v2
   Else
   vmax = v1
   End If

   Label9.Caption = "Max. Tc voltage allowed =" & CStr(vmax) & " uV,
corresponding to delT =" & CStr(vmax / a) & "K"

   Call checkth(TEMP, HFIELD, 1, temptol, BFLG)
   BFLG = 0

heatloop:
   For curop = 0 To curoplim
setheat:
      SetHeater1
      SetHeater2

takereading:

      ReadRefDVM
      ReadSampDVM
      UpdatePlot

      If jplt > (JPLTLAST + 19) Then ThermEquil

      If curop > 0 Then
      Call gettemps(TEMP, Abs(yzero - aa(jplt)), tx, delT)
      Label11.Caption = CStr(aa(jplt) - yzero) & " uV"
      Label13.Caption = CStr(tx) & " K"
      Label15.Caption = CStr(delT) & " K"
      Label17.Caption = CStr(yzero) & " uV"
      DoEvents
      End If

    v = Abs(yzero - ybar)
    Debug.Print "v = " & CStr(v)

   If EQUIL = "Y" Then
      If curop = 1 And Abs(0.5 - v / vmax) > 0.05 Then
         Label44.Caption = Abs(0.5 - v / vmax)
```

```
            Label44.Refresh
            icurstrt = icurstrt * Sqr(0.5 * Abs(vmax / v))
            icurdel = 1 / (curoplim + 1) * icurstrt
            icurend = Sqr(2.1) * icurstrt
            GoTo setheat
        End If
        icurdel = 0.25 * icurstrt
        icurend = Sqr(2.1) * icurstrt
        Save
        GoTo NEXTMEAS
    Else
        GoTo updatelabels       'Take another reading
    End If

updatelabels:
    jplt = jplt + 1
    Label23.Caption = CStr(jplt)
    Label25.Caption = CStr(JPLTLAST)
    Label27.Caption = CStr(curop)
    Label29.Caption = CStr(EQUIL)
    xcurt = Curt * 1000
    Label31.Caption = CStr(xcurt) & " mAMPS"
    DoEvents

    GoTo takereading

NEXTMEAS:

    Next curop

    jplt = 0
    Curt = 0: SetHeater2  ' Power to zero for temperature, field change
    Next HFIELD
    If TEMP >= tcstart And TEMP < tcend Then
      TEMP = TEMP + tcdel
    Else
      TEMP = TEMP + deltemp
    End If

Loop Until TEMP > endtemp

  Terminate
```

```
End Sub

'*********************************************************************


Private Sub FieldSet(h)
'Sets the PPMS field in Gauss

Sleep 2000
mes = "FIELD " & CStr(h) & " 200 0 0"
Call ibwrt(dev15, mes)

End Sub


'*********************************************************************

Private Sub ReadRefDVM()          'Reads ref. DVM
'Debug.Print "ReadRefDVM"
   mes = "MEASURE:VOLT:DC? 0.05 MV,0.0001 MV"
   Call ibwrt(dev11, mes)
   Call ibrd(dev11, a)
   aa(jplt) = 1000000 * Val(a)
   Label6.Caption = aa(jplt)
   Write #2, aa(jplt)
End Sub

'*********************************************************************

Private Sub ReadSampDVM()         'Reads sample DVM
'Debug.Print "ReadSampDVM"
   Call ibrd(dev10, b)
   Call ibrd(dev10, b)
   bb(jplt) = 1000000 * Val(b)
   Label8.Caption = bb(jplt)
   Write #3, bb(jplt)
End Sub

'*********************************************************************
'Set Heater Power
'*********************************************************************
Private Sub SetHeater1()
```

```
    If curop = 0 Then
       Curt = 0
    Else
       Curt = (curop - 1) * (icurend - icurstrt) / (curoplim - 1) + icurstrt
    End If
    Curt = 0.000001 * Curt
 End Sub

Private Sub SetHeater2()
    SCurt = CStr(Curt)
    mes = "I" & SCurt & "V20X" & x
    Call ibwrt(dev12, mes)
    mes = "F1X" & x
    Call ibwrt(dev12, mes)
    Beep 1700, 300
    EQUIL = "N"
    JPLTLAST = jplt
End Sub

'*****************************************************************

Private Function ALPHA(temperature)
'Used in calculating delT, but the alpha2 subroutine
'is also used in places. They are basically the same,
'but alpha2 was implemented when the reference
'was switched from Constantan to Bi2Te3.
'given T in K, returns Seebeck coeff in uv/K

c(1) = -15.29075
c(2) = -0.62695              'Fit for Bi2Te3 NIST-calibrated reference standard
c(3) = 0.00474
c(4) = -0.000188788
c(5) = 0.00000228849
c(6) = -0.0000000146375
c(7) = 5.53862E-11
c(8) = -1.24477E-13
c(9) = 1.54379E-16
c(10) = -8.1643E-20

Call polyeval(10, temperature, P, DP)
'DP = -DP        'Use for the Bi2Te3 fit, sign switch
ALPHA = P
'P = -P          'Use for Bi2Te3 fit, sign switch
```

```
End Function

'*****************************************************************

Private Sub checkth(SETTEMP, SETFIELD, TEMPCHANGED, temptol, BFLG)
'Checks T and H every 5 secconds. When the system has reached the target values for
two consecutive minutes, the sub is exited. tempchanged = 1 indicates an extra
minute of waiting after the temperature has been reached


Label19.Caption = CStr(SETFIELD)
Label21.Caption = CStr(SETTEMP)
DoEvents

doneflag = 0
fieldtol = 40           ‘Gauss variation allowed in field
relaxloop = 25          'Loop through 25 times to let relax

Do While doneflag < relaxloop
   commaflag = 0
   fields = ""
   TEMPs = ""
   i = 0

   mes = "GETDAT? 6 0"
   Call ibwrt(dev15, mes)
   For J = 1 To 1000
   Next J


   Call ibrd(dev15, dta)
   For J = 1 To 4000
   Next J

   Do While commaflag <> 1000 And i < 1000
      i = i + 1
      tester = Mid(dta, i, 1)
      If tester <> "," And tester <> ";" Then
         If commaflag = 3 Then fields = fields & tester
         If commaflag = 2 Then TEMPs = TEMPs & tester
      End If
```

```
        If tester = ";" Then commaflag = 1000
        If tester = "," Then commaflag = 1 + commaflag


    Loop

    If i > 990 Then Label2.Caption = "Error reading PPMS"

    fielder = Abs(Val(fields) - SETFIELD)
    temper = Abs(Val(TEMPs) - SETTEMP)

    Label2.Caption = CStr(fielder) & ", " & CStr(temper) & ", " & CStr(doneflag)
    DoEvents

    If (temper < temptol) And (fielder < fieldtol) Then
       doneflag = doneflag + 1
    Else
'      doneflag = 0
    End If

Loop

If BFLG = 0 Then GoTo blank
If TEMPCHANGED = 1 Then
       For J = 1 To 120
          Sleep 1000
          Label2.Caption = "Temp. relax time = " & CStr(121 - J) & " seconds"
          Label2.Refresh
       Next J
End If

blank:
Label2.Caption = " "

DoEvents
End Sub

'*********************************************************************

Private Sub alpha2(t, a, aprime)
'Given temperature in K, returns Seebeck coeff and
'its derivative in uV/K and uV/K^2, respectively
```

```
c(1) = -15.29075
c(2) = -0.62695            'Fit for Bi2Te3 NIST-calibrated reference standard
c(3) = 0.00474
c(4) = -0.000188788
c(5) = 0.00000228849
c(6) = -0.0000000146375
c(7) = 5.53862E-11
c(8) = -1.24477E-13
c(9) = 1.54379E-16
c(10) = -8.1643E-20


Call polyeval(10, t, a, aprime)
a = Abs(a)
'aprime = -aprime  ' use for Bi2Te3 fit          'Some code above assumes positive alpha
for the reference.
                'Bi2Te3 has negative alpha, so the sign is flipped here
aprime = Abs(aprime)
End Sub

'*********************************************************************

Private Sub gettemps(t0, delv, tx, delT)
'Debug.Print "gettemps"
Dim epsilon As Single, maxit As Integer
Dim dtold As Single, df As Single, dt As Single, f As Single
'the function in froot is called
'bisection method is used to make
'a best estimate of the average temperature
'and delT
epsilon = 0.0001
maxit = 100

'get initial bisection guesses

t1 = t0
t2 = t0 + 2 * Abs(delv / ALPHA(t0))        'ABS (absolute values) are used to keep
delT and V-V0 positive.
tx = 0.5 * (t1 + t2)
dtold = Abs(t2 - t1)
dt = dtold
Call froot(tx, delv, t0, f, df)
```

```
For i = 1 To maxit
   Call froot(tx, delv, t0, f, df)
   dt = f / df
   tx = tx - dt
   If ((t1 - tx) * (tx - t2) < 0) Then     't1 is a lower bound and t2 an upper
      Label2.Caption = "Out of Brackets!" 'bound. Do not want tx outside of t1,t2.
      GoTo subend
   End If
   If (Abs(dt) < epsilon) Then
      GoTo subend           'Convergence
   End If
Next i

Label2.Caption = "Exceeded " & CStr(maxit) & " iterations!"

subend:
delT = Abs(delv / ALPHA(tx))

DoEvents
End Sub

'*********************************************************************

Private Sub ThermEquil()
'Debug.Print "ThermEquil"
Dim tole As Single, IEQUIL As Integer, a1 As Single, a2 As Single
Dim b1 As Single, b2 As Single, sigdat As Single, bsigdat As Single
Dim amat As Variant, bmat As Variant

   Label2.Caption = "CHECKING FOR THERMAL EQUILIBRATION"
   Label2.Refresh
   If jplt < 29 Then GoTo doit

   tole = tole0
   If TEMP < trange1 Then tole = tole1
   If TEMP < trange2 Then tole = tole2

   IEQUIL = 0

   Sleep 2000

   amat = aa()
   bmat = bb()
```

```
   Call linreg2(amat, jplt - 20, jplt, a1, a2, sigdat)
   Call linreg2(bmat, jplt - 20, jplt, b1, b2, bsigdat)
   averr = a2 * 10 / (v1 / 2)
   ybar = a1 + 10 * a2
   'Debug.Print "ybar= " & CStr(ybar)
   bybar = b1 + 10 * b2
   If sigdat / (v1 / 2) > tole Then tole = sigdat / (v1 / 2)
   If Abs(averr) > tole Then IEQUIL = IEQUIL + 1
   If IEQUIL > 0 Then GoTo doit
   EQUIL = "Y"
   Label2.Caption = "EQUILIBRATED"
   Label2.Refresh
   Beep 1700, 300

   Sleep 500
doit:
   DoEvents
End Sub

'*********************************************************************

Private Sub polyeval(n, xx, P, DP)
'Given N coeffs for (N-1)th order polynomial stored in A(1)..A(N)
'Given xx point of evaluation
'Evaluates P(xx) and P'(xx) and stores in P and DP
   'DP = c(1)
   DP = 0
   P = c(n)
   For i = (n - 1) To 1 Step -1
      DP = DP * xx + P
      P = P * xx + c(i)
   Next i

   'For i = 1 To n - 2
   '    DP = DP + (i + 1) * c(i + 2) * xx ^ i
   'Next i

End Sub


'*********************************************************************

Private Sub TEMPSET(t)
```

```
'Sets PPMS temperature in K

Sleep 2000
mes = "TEMP " & CStr(t) & " 10 0"
Call ibwrt(dev15, mes)

End Sub

'*********************************************************************

Private Sub froot(t, delv, t0, f, df)
'Evaluation goes in f
'Derivative goes in df

Call alpha2(t, a, aprime)
f = t0 + 0.5 * delv / a - t
df = 0.5 * aprime * delv / a ^ 2 - 1
'df = Abs(0.5 * aprime * delv / a ^ 2 - 1)

End Sub

'*********************************************************************

Private Sub setcurrent(i)
' i current in uA

x = CStr(Chr(13))
Curt = CStr(i * 0.000001)
mes = "I" & CStr(Curt) & "V20X" & x
Call ibwrt(dev12, mes)
mes = "F1X" & x
Call ibwrt(dev12, mes)

End Sub

'*********************************************************************

Private Sub linreg2(yy, firstx, lastx, K, L, sigdat)
'Fits y=K+L*i  to yy with i between firstx and lastx
sx = 0
sy = 0
st2 = 0
L = 0
```

```
chi2 = 0

anzx = Abs(lastx - firstx)
Debug.Print anzx

For i = 1 To anzx
sx = sx + i
sy = sy + yy(firstx + i)
Debug.Print sy, yy(firstx + i)
Next i

sxoss = sx / anzx

For i = 1 To anzx
t = i - sxoss
st2 = st2 + t * t
L = L + t * yy(firstx + i)
Next i

L = L / st2
K = (sy - sx * L) / anzx

For i = 1 To anzx
chi2 = chi2 + (yy(firstx + i) - K - L * i) ^ 2
Next i
sigdat = Sqr(chi2 / (anzx - 2))



End Sub

'*********************************************************************


Private Sub UpdatePlot()
   If jplt < 417 Then
   temp2(jplt, 0) = jplt
   temp2(jplt, 1) = aa(jplt)
   temp2(jplt, 2) = jplt
   temp2(jplt, 3) = bb(jplt)
   ReDim Drifts(jplt, 3)
   For i = 0 To jplt
   Drifts(i, 0) = temp2(i, 0)
```

```
Drifts(i, 1) = temp2(i, 1)
Drifts(i, 2) = temp2(i, 2)
Drifts(i, 3) = temp2(i, 3)
Next i
Else
For i = 0 To 300
aa(i) = aa(i + 117)
bb(i) = bb(i + 117)
Next i
jplt = 301
For i = 0 To 300
temp2(i, 0) = i
temp2(i, 1) = aa(i)
temp2(i, 2) = i
temp2(i, 3) = bb(i)
Next i

ReDim Drifts(jplt, 3)
For i = 0 To jplt - 1
Drifts(i, 0) = temp2(i, 0)
Drifts(i, 1) = temp2(i, 1)
Drifts(i, 2) = temp2(i, 2)
Drifts(i, 3) = temp2(i, 3)
Next i

JPLTLAST = JPLTLAST - 116
End If

With MSChart1                          'Temp drifts plot parameters, plot is called
"MSChart1"
.Plot.UniformAxis = False              'Makes the axis change dynamically
.ColumnCount = 4                       '# columns of data
.RowCount = jplt + 1                   '# rows of data
.ChartData = Drifts                    'Data array name
.Plot.Axis(VtChAxisIdX).ValueScale.Auto = False
.Plot.Axis(VtChAxisIdX).ValueScale.Minimum = Drifts(0, 0)
.Plot.Axis(VtChAxisIdX).ValueScale.Maximum = jplt
If Check1.value = 1 Then
.Plot.Axis(VtChAxisIdY).ValueScale.Minimum = Val(Text2.Text)
.Plot.Axis(VtChAxisIdY).ValueScale.Maximum = Val(Text3.Text)
Else
.Plot.Axis(VtChAxisIdY).ValueScale.Auto = True
End If
```

```
    .Plot.SeriesCollection(1).SeriesMarker.Auto = False
    .Plot.SeriesCollection(1).DataPoints(-1).Marker.Size = 100
    .Plot.SeriesCollection(1).DataPoints(-1).Marker.Style = VtMarkerStyleFilledCircle
    .Plot.SeriesCollection(2).SeriesMarker.Auto = False
    .Plot.SeriesCollection(2).DataPoints(-1).Marker.Size = 100
    .Plot.SeriesCollection(2).DataPoints(-1).Marker.Style = VtMarkerStyleFilledCircle
    .Refresh
    End With

End Sub

'*********************************************************************

Private Sub SeebeckPlot()

With MSChart2                          'Parameters for S plot
    .Plot.UniformAxis = False
    .ColumnCount = 2
    .RowCount = counter
    .ChartData = Seebeck
    .Plot.SeriesCollection(1).SeriesMarker.Auto = False
    .Plot.SeriesCollection(1).DataPoints(-1).Marker.Size = 100
    .Plot.SeriesCollection(1).DataPoints(-1).Marker.Style = VtMarkerStyleFilledCircle
    .Refresh
End With
End Sub

'*********************************************************************

Private Sub Terminate()
'Debug.Print "Terminate"
    mes = "TEMP 70 10 0"
    Call ibwrt(dev15, mes)
    Sleep 2000
    mes = "FIELD " & "0 100 0 0"
    Call ibwrt(dev15, mes)

    Call ibonl(dev10, 0)
    Call ibonl(dev11, 0)
    Call ibonl(dev12, 0)
    Call ibonl(dev15, 0)
    Close
    Stop
```

```
End Sub

'*********************************************************************

Private Sub Save()
   If curop = 0 Then
      yzero = ybar
      byzero = bybar
      errzero = sd
      GoTo TheEnd
   End If

   POWER = heatres * Curt ^ 2
   Call gettemps(TEMP, Abs(yzero - ybar), tx, delT)
   GetSystemTime st
   SampS = (bybar - byzero) / delT
   tm = st.wHour + (1 / 60) * st.wMinute + (1 / 3600) * st.wSecond

   temp1(counter, 0) = TEMP
   temp1(counter, 1) = SampS

   ReDim Seebeck(counter, 1)

   For i = 0 To counter
   Seebeck(i, 0) = temp1(i, 0)
   Seebeck(i, 1) = temp1(i, 1)
   Next i

   SeebeckPlot

   counter = counter + 1

   Open XNAM For Append As #1
      If LOF(1) = 0 Then Print #1, "Temp, Bathtemp, Time, FIELD, CURRENT,
Power, V0const, dVconst, delT, V0samp, dVsamp, S"
      Print #1, tx, ",", TEMP, ",", tm, ",", HFIELD, ",", Curt, ",", POWER, ",", yzero,
",", ybar, ",", delT, ",", byzero, ",", bybar, ",", SampS
   Close #1

TheEnd:

End Sub
```

```
'*****************************************************************

Private Sub Command2_Click()
   Save
   Curt = 0: SetHeater2
   Close #2
   Close #3
   Terminate
End Sub
```

C. Specific heat Visual Basic 6 program

The program used to automate the $C(T)$ measurement in the dilution refrigerator is copied here, with occasional annotations. Only the main body of the program, which controls the plot window, is shown.

```
'This form codes for the main plot window, and contains the main subroutines
Option Explicit                 'This means that variables must be explicitly declared
Private st As SYSTEMTIME            'usually at the beginning of a form or a
                                                                    ‘subroutine
Private k As Integer, IG As Integer, I As Integer, Counter As Integer
Private F1 As Integer, TW1 As Double, TW2 As Double
Private AV As String * 20
Private U3 As Double, U4 As Double, U8 As Double, U9 As Double, TM1 As
Double, TM2 As Double, V8 As Double, V9 As Double
Private PREVTEMP As Double, M7 As Double, MaxX As Double, sigot As Double

Private temp1(1000, 1) As Double, Drifts() As Double 'temp1/temp2 have all of the
temp drift/spec heat data, but are fixed size arrays.
Private temp2(1000, 1) As Double, SpecHeat() As Double 'Drift/SpecHeat are the
variable size arrays for plotting. Data from temp1/temp2
Private STATUS0 As Double, STATUS1 As Double, TT As Double 'are transferred
to Drift/SpecHeat so that the empty array entries aren't plotted


Private Sub Command1_Click()                'Executes once you click the "Start
Run" button

    NRUN = 1: J = 1: Counter = 0: F1 = 0: T(0) = 0  'J is the data pair index, NRUN is
the spec. heat data pt. index
    Beep 500, 500                   'When F1 = 1, the program terminates
    NPTS = DRLN
    GetLocalTime st                 'Time read from system clock in seconds
    STATUS0 = 3600 * Val(st.wHour) + 60 * st.wMinute + st.wSecond + (1 / 1000) *
st.wMilliseconds
    STATUS0real = STATUS0  '$$$$$
    TempReadRoutine                 'Calls the TempReadRoutine
    DoEvents                    'Updates the form (PlotForm) and any user
actions
End Sub
```

```
'******************  READ ROUTINE  ***************
Private Sub TempReadRoutine()                    'This routine reads and records the temperature from the lock-in
Option1.value = True                             'These control the radio buttons to indicate which routine is running
Option2.value = False
Option3.value = False
'Debug.Print "TempReadRoutine"

GetLocalTime st
   STATUS0 = 3600 * Val(st.wHour) + 60 * st.wMinute + st.wSecond + (1 / 1000) * st.wMilliseconds  ' t = 0 for the present drift

Do Until J > NPTS                                'Read resistance. This is an averaging routine.
                                                 'Take multiple readings and average them.
   AVS = 0
   For IG = 1 To TCONST
      Call ibwrt(dev11, "TRIG")
      Call ibrd(dev11, AV)                       'Reads the DVM output from the lock-in
      AVS = AVS + (Val(AV))
   Next IG

   AVS = Math.Log(RES1 - DRDV * AVS / TCONST) - 6.8
                                                 'Converts voltage to resistance
   GetLocalTime st
   STATUS1 = 3600 * Val(st.wHour) + 60 * st.wMinute + st.wSecond + (1 / 1000) * st.wMilliseconds  ' t at time of voltage reading
   TT = STATUS1 - STATUS0                        ' Relative time from the beginning of the drift
   Treal = STATUS1 - STATUS0real                 ' relative time from the start of the run
   T(J) = TT
   Text3.Text = T(J)                             'Print time on form

   U9 = (A0 + A1 * AVS + A2 * AVS ^ 2 + A3 * AVS ^ 3 + A4 * AVS ^ 4) ^ -4
'Calculate temperature from resistance
   'U9 = (A0 + A1 * AVS + A2 * AVS ^ 2) ^ -4     'Use if only have coefficients to second power
   v(J) = U9

   AddTempDriftToFile                            'Activate to save temp drift data to file
   If Counter = 0 Then
```

```
        temp1(Counter * NPTS + J - 1, 0) = T(J)
        temp1(Counter * NPTS + J - 1, 1) = v(J) / v(1)
    Else
        temp1(Counter * NPTS + J - 1, 0) = temp1(Counter * NPTS - 1, 0) + T(J)
'Write time and temperature to file
        temp1(Counter * NPTS + J - 1, 1) = v(J) / v(1)
    End If

'Redimension the plot data arrays to the correct size to avoid empty array entries
    ReDim Drifts(150, 1)

    If Counter * NPTS + J < 150 Then
    For I = 0 To Counter * NPTS + J - 1                    'Input data from temp1
array to Drifts array
        Drifts(I, 0) = temp1(I, 0)
        Drifts(I, 1) = temp1(I, 1)
    Next I
        MaxX = Drifts(Counter * NPTS + J - 1, 0)
    Else
    For I = 0 To 150
        Drifts(I, 0) = temp1(Counter * NPTS + J + I - 150, 0)
        Drifts(I, 1) = temp1(Counter * NPTS + J + I - 150, 1)
    Next I
        MaxX = Drifts(149, 0)
    End If

    If J = 1 Then U8 = U9

    Text2.Text = J                    'Display J and temperature values on form in
textboxes
    Text4.Text = v(J)

    If NRUN = NTMPS Or v(J) > UPTEMP Or NRUN = 1498 Or Check1.value = 1
Then                                                   'Termination conditions
        F1 = 1
    End If

    J = J + 1

    With MSChart1                    'Temp drifts plot parameters
    .Plot.UniformAxis = False          'Makes the axis change dynamically
    .ColumnCount = 2                  '# columns of data
    .RowCount = 150                   '# rows of data
```

```
    .ChartData = Drifts                    'Data array name
    .Plot.Axis(VtChAxisIdX).ValueScale.Auto = False
    .Plot.Axis(VtChAxisIdX).ValueScale.Minimum = Drifts(0, 0)
    .Plot.Axis(VtChAxisIdX).ValueScale.Maximum = MaxX
    .Plot.Axis(VtChAxisIdY).ValueScale.Minimum = Val(Text14.Text)
    .Plot.Axis(VtChAxisIdY).ValueScale.Maximum = 1
    .Plot.SeriesCollection(1).SeriesMarker.Auto = False
    .Plot.SeriesCollection(1).DataPoints(-1).Marker.Size = 100
    .Plot.SeriesCollection(1).DataPoints(-1).Marker.Style = VtMarkerStyleFilledCircle
    End With
    DoEvents
Loop
Counter = Counter + 1
If J > NPTS Then                           'If this routine finishes, play a sound
    wmp1.URL = "C:\Windows\Media\Festival\Windows Print Complete.wav"
    DriftSlopeIntCalc I9, NPTS, NRUN       'Calculate the slope & intercept
(routine defined in module)
End If

If NRUN > 1 Then                           'If NRUN > 1, heat pulse has been applied,
so go to SpecHeatRoutine
    SpecHeatCalcRoutine
Else
    HeatRoutine                        'If heat hasn't been applied yet, go to HeatRoutine
End If

End Sub

' ************ HEAT ROUTINE ************
Private Sub HeatRoutine()
Option2.value = True                       'Radio button indicators
Option1.value = False
Option3.value = False

Text5.Text = CURT                          'Display CURT in text box 5 on form
ICURT = ICURT + Z14                            ' TURN ON HEAT - old command was
ICURT = ICURT - 1
TM1 = 3600 * Val(st.wHour) + 60 * st.wMinute + st.wSecond + (1 / 1000) *
st.wMilliseconds - STATUS0  'GetLocalTime st
ICURTCOMP = (Z16 - 1) - ICURT    'see Initial code for explanation
MES = "SOUR:DIG:DATA:WORD " & CStr(ICURTCOMP) & ",(@1001)"
Call ibwrt(dev19, MES)
Text6.Text = NRUN                          'Display NRUN in text box 6 on form
```

```
DoEvents                                'Update PlotForm and user actions

For J = 1 To Val(HTLN)
   Sleep 2000
   Call ibwrt(dev20, "MEAS:VOLT:DC? 1")
   Call ibrd(dev20, AA)                 'Read heater current AA -> V3 -> V8
   Call ibwrt(dev22, "MEAS:VOLT:DC? 1")
   Call ibrd(dev22, aaa)                'Read heater voltage aaa -> V2 -> V9
   V2(J) = CSng(Val(aaa)): V3(J) = CSng(Val(AA))
   Text7.Text = J                       'Display J, current, and voltage on form
   Text13.Text = V2(J) * 1000
   Text8.Text = V3(J) * 1000
   DoEvents

   AVS = 0                              ' Read temperature for recording drift data
   'For IG = 1 To 3
      Call ibwrt(dev11, "TRIG")
      Call ibrd(dev11, AV)
      AVS = AVS + (Val(AV))
   'Next IG
   AVS = Math.Log(RES1 - DRDV * AVS) - 6.8
   GetLocalTime st
   Treal = 3600 * Val(st.wHour) + 60 * st.wMinute + st.wSecond + (1 / 1000) *
st.wMilliseconds - STATUS0real
   U9 = (A0 + A1 * AVS + A2 * AVS ^ 2 + A3 * AVS ^ 3 + A4 * AVS ^ 4) ^ -4
   'U9 = (A0 + A1 * AVS + A2 * AVS ^ 2) ^ -4          'if only have coefficients to
second power
   AddTempDriftToFile                   'Activate to save drift data to file

Next J
GetLocalTime st
TM2 = 3600 * Val(st.wHour) + 60 * st.wMinute + st.wSecond + (1 / 1000) *
st.wMilliseconds - STATUS0
ICURT = ICURT - Z14                     ' old command was ICURT = ICURT + 1
ICURTCOMP = (Z16 - 1) - ICURT
MES = "SOUR:DIG:DATA:WORD " & CStr(ICURTCOMP) & ",(@1001)"   '  old
command was MES = "DWRITE 202, " + CStr(ICURT)     ' TURN OFF HEAT ------
---------
Call ibwrt(dev19, MES)

V9 = 0: V8 = 0
```

```
For I = 1 To J - 1                          'Throw out last voltage reading, in case of
transients
   V9 = V9 + V2(I): V8 = V8 + V3(I)
Next I
'If U9 > 4 Then CFAC = 1.05
CURT = CURT * CFAC: ICURT = CInt(CURT) + Z14
ICURT = CInt(CURT) * 16 + 2      'Increment current
ICURTCOMP = (Z16 - 1) - ICURT
MES = "SOUR:DIG:DATA:WORD " & CStr(ICURTCOMP) & ",(@1001)"     'old
command MES = "DWRITE 202, " + CStr(ICURT)
Call ibwrt(dev19, MES)


Q(NRUN) = (V8 / 100 * V9 * (TM2 - TM1)) / (J - 1) ^ 2    'Calculate heat pulse
TW1 = TM2

RELAXCOUNT = 0
Do Until RELAXCOUNT = ITC              'Wait for internal time constant, internal
thermal equilibrium
   AVS = 0
   For IG = 1 To TCONST
      Call ibwrt(dev11, "TRIG")
      Call ibrd(dev11, AV)
      AVS = AVS + (Val(AV))
   Next IG
   AVS = Math.Log(RES1 - DRDV * AVS / TCONST) - 6.8
   GetLocalTime st
   T(J) = 3600 * Val(st.wHour) + 60 * st.wMinute + st.wSecond + (1 / 1000) *
st.wMilliseconds - STATUS0
   Treal = 3600 * Val(st.wHour) + 60 * st.wMinute + st.wSecond + (1 / 1000) *
st.wMilliseconds - STATUS0real
   TW2 = T(J)
   U9 = (A0 + A1 * AVS + A2 * AVS ^ 2 + A3 * AVS ^ 3 + A4 * AVS ^ 4) ^ -4
   'U9 = (A0 + A1 * AVS + A2 * AVS ^ 2) ^ -4              'if only have coefficients to
second power
   AddTempDriftToFile                  'Activate to save drift data to file - stores
Treal, U9
   DoEvents
   RELAXCOUNT = RELAXCOUNT + 1
Loop

GetLocalTime st
```

```
TW2 = 3600 * Val(st.wHour) + 60 * st.wMinute + st.wSecond + (1 / 1000) *
st.wMilliseconds - STATUS0

NRUN = NRUN + 1
J = 1: F1 = 0: T(0) = 0
Beep 500, 500
TempReadRoutine                    'Calls TempReadRoutine again after heat
pulse & thermal equilibrium

End Sub

Private Sub SpecHeatCalcRoutine()          ' Calculate specific heat
Dim MRUN As Integer
Dim TMM As Double
Dim TMD As Double
Dim M7 As Double

Option3.value = True               'Radio button indicators
Option1.value = False
Option2.value = False

MRUN = NRUN - 1


TMM = (TM2 - TM1) / 2 + (TW2 - TW1) / 2
'TMD = (TM2 - TM1) / 2 + (TW2 - TW1) / 2
R1(MRUN) = INTR(MRUN) + SLP(MRUN) * (TMM + TM1)
R2(MRUN) = INTR(NRUN) - SLP(NRUN) * TMM
U3 = R1(MRUN)
U4 = R2(MRUN)
M7 = (U4 + U3) / 2
c(MRUN) = Q(MRUN) / ((U4 - U3) * M7)
c(MRUN) = c(MRUN) / XNMOLE

' AddSpecHeatToFile

temp2(MRUN - 1, 0) = M7
temp2(MRUN - 1, 1) = c(MRUN)
ReDim SpecHeat(MRUN - 1, 1)            'Change size of SpecHeat array so
that there are no extra empty entries
For I = 0 To MRUN - 1                  'Get data from temp2 array
   SpecHeat(I, 0) = temp2(I, 0)
   SpecHeat(I, 1) = temp2(I, 1)
```

```
Next I

PREVTEMP = (U4 + U3) / 2
If F1 = 1 Then
   Terminate
End If

DoEvents

Text9.Text = CFAC                          'Display values in PlotForm
Text10.Text = Q(MRUN)
Text11.Text = R1(MRUN)
Text12.Text = R2(MRUN)

With MSChart2                              'Parameters for spec heat plot, called MSChart 2
   .Plot.UniformAxis = False
   .ColumnCount = 2
   .RowCount = NRUN
   .ChartData = SpecHeat
   .Plot.SeriesCollection(1).SeriesMarker.Auto = False
   .Plot.SeriesCollection(1).DataPoints(-1).Marker.Size = 100
   .Plot.SeriesCollection(1).DataPoints(-1).Marker.Style = VtMarkerStyleFilledCircle
End With

HeatRoutine

End Sub


Private Sub Command2_Click()
   Terminate
End Sub

Private Sub Terminate()                    'Subroutine for when run is finished
Dim msg As String
   msg = "Got here!"
   MsgBox (msg)
   Open XXNAM For Append As #4             'Append to the file
      Print #4, "Temp, C, CoT, Q, R1, R2, Tsqrd, sigotT"
      For I = 1 To NRUN - 1
         TM = (R1(I) + R2(I)) / 2
         sigot = Q(I) / (R2(I) - R1(I)) / TM
```

```
        Print #4, TM, c(I) * TM, c(I), Q(I), R1(I), R2(I), TM ^ 2, sigot 'Information to
be saved
      Next I
   Close #4

   ICURT = CInt(ACURT) + Z14    'old command: ICURT = CInt(ACURT) * 16 + 2
' re-set heater current to starting value
   ICURTCOMP = (Z16 - 1) - ICURT
   MES = "SOUR:DIG:DATA:WORD " & CStr(ICURTCOMP) & ",(@1001)"   'old
command: MES = "DWRITE 202, " + CStr(ICURT)
   Call ibwrt(dev19, MES)

   Call ibonl(dev11, 0)                    'Clear the unit descriptors used by the
devices
   Call ibonl(dev19, 0)
   Call ibonl(dev20, 0)
   Call ibonl(dev22, 0)

        Stop
End Sub

Private Sub AddTempDriftToFile()                'Subroutine writes time and
temperature to file
   Open XXNAMDRFT For Append As #5
      ' Print #5, T(J), ",", U9
      Print #5, Treal, ",", U9  '$$$$$$
   Close #5
End Sub
```

References

Abrikosov, A. A. (1998). "Quantum magnetoresistance." Physical Review B **58**(5): 2788-2794.

Abrikosov, A. A. (2000). "Quantum linear magnetoresistance." Europhysics Letters **49**(6): 789-793.

Ackermann, J. and A. Wold (1977). "Preparation and Characterization of Cobalt Skutte-Rudites Cop3, Coas3 and Cosb3." Journal of Physics and Chemistry of Solids **38**(9): 1013-1016.

Altarawneh, M. M., N. Harrison, G. Li, L. Balicas, P. H. Tobash, F. Ronning and E. D. Bauer (2012). "Superconducting Pairs with Extreme Uniaxial Anisotropy in URu2Si2." Physical Review Letters **108**(6).

Altarawneh, M. M., N. Harrison, S. E. Sebastian, L. Balicas, P. H. Tobash, J. D. Thompson, F. Ronning and E. D. Bauer (2011). "Sequential Spin Polarization of the Fermi Surface Pockets in URu2Si2 and Its Implications for the Hidden Order." Physical Review Letters **106**(14).

Ashby, P. E. C. and J. P. Carbotte (2014). "Theory of magnetic oscillations in Weyl semimetals." European Physical Journal B **87**(4).

Ashcroft, N. W. and N. D. Mermin (1976). Solid state physics. New York,, Holt.
Baibich, M. N., J. M. Broto, A. Fert, F. N. Vandau, F. Petroff, P. Eitenne, G. Creuzet, A. Friederich and J. Chazelas (1988). "Giant Magnetoresistance of (001)Fe/(001) Cr Magnetic Superlattices." Physical Review Letters **61**(21): 2472-2475.

Balberg, I. and J. S. Helman (1978). "Critical Behavior of Resistivity in Magnetic Systems .2. Below Tc and in Presence of a Magnetic-Field." Physical Review B **18**(1): 303-318.

Balents, L. (2010). "Spin liquids in frustrated magnets." Nature **464**(7286): 199-208.

Battiato, M., J. M. Tomczak, Z. Zhong and K. Held (2015). "Unified Picture for the Colossal Thermopower Compound FeSb2." Physical Review Letters **114**(23).

Bentien, A., S. Johnsen, G. K. H. Madsen, B. B. Iversen and F. Steglich (2007). "Colossal Seebeck coefficient in strongly correlated semiconductor FeSb(2)." Epl **80**(1).

Berger, L. (1970). "Side-jump mechanism for the Hall effect of ferromagnets." Physical Review B-Solid State **2**(11): 4559-4566.

Berry, M. V. (1984). "Quantal Phase-Factors Accompanying Adiabatic Changes." Proceedings of the Royal Society of London Series a-Mathematical Physical and Engineering Sciences **392**(1802): 45-57.

Blatt, F. J. (1968). Physics of electronic conduction in solids. New York,, McGraw-Hill.

Bordet, P., I. Gelard, K. Marty, A. Ibanez, J. Robert, V. Simonet, B. Canals, R. Ballou and P. Lejay (2006). "Magnetic frustration on a Kagome lattice in R3Ga5SiO14 langasites with R = Nd, Pr." Journal of Physics-Condensed Matter **18**(22): 5147-5153.

Bramwell, S. T., M. N. Field, M. J. Harris and I. P. Parkin (2000). "Bulk magnetization of the heavy rare earth titanate pyrochlores - a series of model frustrated magnets." Journal of Physics-Condensed Matter **12**(4): 483-495.

Bramwell, S. T. and M. J. P. Gingras (2001). "Spin ice state in frustrated magnetic pyrochlore materials." Science **294**(5546): 1495-1501.

Bramwell, S. T., M. J. Harris, B. C. den Hertog, M. J. P. Gingras, J. S. Gardner, D. F. McMorrow, A. R. Wildes, A. L. Cornelius, J. D. M. Champion, R. G. Melko and T. Fennell (2001). "Spin correlations in Ho(2)Ti(2)O(7): A dipolar spin ice system." Physical Review Letters **87**(4).

Broholm, C., H. Lin, P. T. Matthews, T. E. Mason, W. J. L. Buyers, M. F. Collins, A. A. Menovsky, J. A. Mydosh and J. K. Kjems (1991). "Magnetic Excitations in the Heavy-Fermion Superconductor Uru2si2." Physical Review B **43**(16): 12809-12822.

Brooks, M. L., S. J. Blundell, T. Lancaster, W. Hayes, F. L. Pratt, P. P. C. Frampton and P. D. Battle (2005). "Unconventional magnetic properties of the weakly ferromagnetic metal BaIrO3." Physical Review B **71**(22).

Buhot, J., M. A. Measson, Y. Gallais, M. Cazayous, A. Sacuto, G. Lapertot and D. Aoki (2014). "Symmetry of the Excitations in the Hidden Order State of URu2Si2." Physical Review Letters **113**(26).

Caillat, T. (1993). Novel Transition Metal Compounds with Promising Thermoelectric Properties. The XII International Conference on Thermoelectrics, Yokohama (Japan).

Cao, G., J. E. Crow, R. P. Guertin, P. F. Henning, C. C. Homes, M. Strongin, D. N. Basov and E. Lochner (2000). "Charge density wave formation accompanying ferromagnetic ordering in quasi-one-dimensional BaIrO3." Solid State Communications **113**(11): 657-662.

Chaikin, P. M. (1990). "An Introduction to Thermopower for Those Who Might Want to Use It to Study Organic Conductors and Superconductors." Organic Superconductivity: 101-115.

Chalupa, J. (1977). "Scaling at Critical-Temperature of a Spin Glass." Solid State Communications **24**(6): 429-431.

Champion, J. D. M., A. S. Wills, T. Fennell, S. T. Bramwell, J. S. Gardner and M. A. Green (2001). "Order in the Heisenberg pyrochlore: The magnetic structure of Gd2Ti2O7." Physical Review B **64**(14).

Champnes.Ch, W. B. Muir and P. T. Chiang (1967). "Thermoelectric Properties of N-Type Bi2te3-Bi2se3 Alloys." Canadian Journal of Physics **45**(11): 3611-&.

Chandra, P., P. Coleman and R. Flint (2013). "Hastatic order in the heavy-fermion compound URu2Si2." Nature **493**(7434): 621-626.

Chandra, P., P. Coleman and R. Flint (2014). "Ising quasiparticles and hidden order in URu2Si2." Philosophical Magazine **94**(32-33): 3803-3819.

Chandra, P., P. Coleman and R. Flint (2015). "Hastatic order in URu2Si2: Hybridization with a twist." Physical Review B **91**(20).

Cheng, J. G., J. S. Zhou, J. A. Alonso, J. B. Goodenough, Y. Sui, K. Matsubayashi and Y. Uwatoko (2009). "Transition from a weak ferromagnetic insulator to an exchange-enhanced paramagnetic metal in the BaIrO3 polytypes." Physical Review B **80**(10).

Chien, C. L. and C. R. Westgate (1980). The Hall effect and its applications. New York, Plenum Press.

Coey, J. M. D. (2001). "Magnetic materials." Journal of Alloys and Compounds **326**(1-2): 2-6.

Coey, J. M. D., M. Venkatesan and M. A. Bari (2001). "Half-metallic ferromagnets." High Magnetic Fields **595**: 377-396.

Cotton, F. A. and F. A. Cotton (1999). Advanced inorganic chemistry. New York, Wiley.

Das, P., R. E. Baumbach, K. Huang, M. B. Maple, Y. Zhao, J. S. Helton, J. W. Lynn, E. D. Bauer and M. Janoschek (2013). "Absence of a static in-plane magnetic moment in the 'hidden-order' phase of URu2Si2." New Journal of Physics **15**.

Dun, Z. L., J. Trinh, K. Li, M. Lee, K. W. Chen, R. Baumbach, Y. F. Hu, Y. X. Wang, E. S. Choi, B. S. Shastry, A. P. Ramirez and H. D. Zhou (2016). "Magnetic Ground States of the Rare-Earth Tripod Kagome Lattice Mg2RE3Sb3O14 (RE = Gd,Dy,Er)." Physical Review Letters **116**(15).

Eilertsen, J., J. Li, S. Rouvimov and M. A. Subramanian (2011). "Thermoelectric properties of indium-filled InxRh4Sb12 skutterudites." Journal of Alloys and Compounds **509**(21): 6289-6295.

Eilertsen, J., S. Rouvimov and M. A. Subramanian (2012). "Rattler-seeded InSb nanoinclusions from metastable indium-filled In0.1Co4Sb12 skutterudites for high-performance thermoelectrics." Acta Materialia **60**(5): 2178-2185.

Ekin, J. W. (2006). Experimental techniques for low-temperature measurements : cryostat design, material properties, and superconductor critical-current testing. Oxford ; New York, Oxford University Press.

Evtushinsky, D. V., A. A. Kordyuk, V. B. Zabolotnyy, D. S. Inosov, B. Buchner, H. Berger, L. Patthey, R. Follath and S. V. Borisenko (2008). "Pseudogap-driven sign reversal of the Hall effect." Physical Review Letters **100**(23).

Fagaly, R. L. (2006). "Superconducting quantum interference device instruments and applications." Review of Scientific Instruments **77**(10).

Falicov, L. M. and R. Q. Hood (1994). "Theory of the Negative Magnetoresistance of Ferromagnetic-Normal Metallic Multilayers (Invited)." Journal of Applied Physics **76**(10): 6595-6600.

Feng, D. and G. Jin (2005). Introduction to condensed matter physics. Hackensack, NJ, World Scientific.

Fischbeck, H. J. (1975). "Hall-Effect and Thermopower of 2 Simple Heavily Doped Semiconductor Models." Physica Status Solidi B-Basic Research **67**(1): 157-167.

Fisher, M. E. and J. S. Langer (1968). "Resistive Anomalies at Magnetic Critical Points." Physical Review Letters **20**(13): 665-&.

Flint, R., P. Chandra and P. Coleman (2014). "Hidden and Hastatic Orders in URu2Si2." Journal of the Physical Society of Japan **83**(6).

Flynn, J., J. Li, A. W. Sleight, A. P. Ramirez and M. A. Subramanian (2016). "Structure and Properties of Ir-Containing Oxides with Large Spin-Orbit Coupling: Ba2In2-xIrxO5+delta." Inorganic Chemistry **55**(6): 2748-2754.

Freitas, P. P., R. Ferreira, S. Cardoso and F. Cardoso (2007). "Magnetoresistive sensors." Journal of Physics-Condensed Matter **19**(16).

Friedman, A. L., J. L. Tedesco, P. M. Campbell, J. C. Culbertson, E. Aifer, F. K. Perkins, R. L. Myers-Ward, J. K. Hite, C. R. Eddy, G. G. Jernigan and D. K. Gaskill (2010). "Quantum Linear Magnetoresistance in Multi layer Epitaxial Graphene." Nano Letters **10**(10): 3962-3965.

Fritzsch.H (1971). "General Expression for Thermoelectric Power." Solid State Communications **9**(21): 1813-&.

Fu, W. T. and D. J. W. Ijdo (2014). "Crystal structure of Mn(2)Ln(3)Sb(3)O(14) (Ln=La, Pr and Nd): A new ordered rhombohedral pyrochlore." Journal of Solid State Chemistry **213**: 165-168.

Gerber, A., I. Kishon, I. Y. Korenblit, O. Riss, A. Segal, M. Karpovski and B. Raquet (2007). "Linear positive magnetoresistance and quantum interference in ferromagnetic metals." Physical Review Letters **99**(2).

Getzlaff, M. (2008). Fundamentals of magnetism. Berlin ; New York, Springer.
Gibbs, Z. M., H. S. Kim, H. Wang and G. J. Snyder (2015). "Band gap estimation from temperature dependent Seebeck measurement-Deviations from the 2e vertical bar S vertical bar T-max(max) relation." Applied Physics Letters **106**(2).

Goldsmid, H. J. (2010). Introduction to thermoelectricity. Heidelberg ; New York, Springer.

Haas, C. (1968). "Spin-Disorder Scattering and Magnetoresistance of Magnetic Semiconductors." Physical Review **168**(2): 531-&.

Han, T. H., J. S. Helton, S. Y. Chu, D. G. Nocera, J. A. Rodriguez-Rivera, C. Broholm and Y. S. Lee (2012). "Fractionalized excitations in the spin-liquid state of a kagome-lattice antiferromagnet." Nature **492**(7429): 406-410.

Harima, H., K. Miyake and J. Flouquet (2010). "Why the Hidden Order in URu2Si2 Is Still Hidden-One Simple Answer." Journal of the Physical Society of Japan **79**(3).

Harris, M. J., S. T. Bramwell, D. F. McMorrow, T. Zeiske and K. W. Godfrey (1997). "Geometrical frustration in the ferromagnetic pyrochlore Ho2Ti2O7." Physical Review Letters **79**(13): 2554-2557.

Haule, K. and G. Kotliar (2009). "Arrested Kondo effect and hidden order in URu2Si2." Nature Physics **5**(11): 796-799.

Hayes, I. M., R. D. McDonald, N. P. Breznay, T. Helm, J. W. Moll, M. Wartenbe, A. Shekhter and J. G. Analytis (2016). "Scaling between magnetic field and temperature in the high-temperature superconductor BaFe2(As1-xPx)2." Nature Physics **AOP**.

He, T., J. Z. Chen, H. D. Rosenfeld and M. A. Subramanian (2006). "Thermoelectric properties of indium-filled skutterudites." Chemistry of Materials **18**(3): 759-762.

Herring, C. (1954). "Theory of the Thermoelectric Power of Semiconductors." Physical Review **96**(5): 1163-1187.

Herring, C. (1960). "Effect of Random Inhomogeneities on Electrical and Galvanomagnetic Measurements." Journal of Applied Physics **31**(11): 1939-1953.

Hosur, P. and X. L. Qi (2013). "Recent developments in transport phenomena in Weyl semimetals." Comptes Rendus Physique **14**(9-10): 857-870.

Hu, J. S. and T. F. Rosenbaum (2008). "Classical and quantum routes to linear magnetoresistance." Nature Materials **7**(9): 697-700.

Hu, J. S., T. F. Rosenbaum and J. B. Betts (2005). "Current jets, disorder, and linear magnetoresistance in the silver chalcogenides." Physical Review Letters **95**(18).

Hu, R. W., V. F. Mitrovic and C. Petrovic (2008). "Giant carrier mobility in single crystals of FeSb(2)." Applied Physics Letters **92**(18).

Hu, R. W., V. F. Mitrovic and C. Petrovic (2009). "Magnetism and metal-insulator transition in Fe(Sb1-xTex)(2)." Physical Review B **79**(6).

Hu, R. W., K. F. Wang, H. J. Ryu, H. C. Lei, E. S. Choi, M. Uhlarz, J. Wosnitza and C. Petrovic (2012). "Electronic Griffiths Phase in the Te-Doped Semiconductor FeSb2." Physical Review Letters **109**(25).

Idzikowski, B., M. Wolf, A. Handstein, K. Nenkov, H. J. Engelmann, F. Stobiecki and K. H. Muller (1997). "Inverse giant magnetoresistance in granular Nd2Fe14B/alpha-Fe." Ieee Transactions on Magnetics **33**(5): 3559-3561.

Ikeda, H., M. T. Suzuki, R. Arita, T. Takimoto, T. Shibauchi and Y. Matsuda (2012). "Emergent rank-5 nematic order in URu2Si2." Nature Physics **8**(7): 528-533.

Ikeda, K., S. K. Dhar, M. Yoshizawa and K. A. Gschneidner (1991). "Quenching of Spin Fluctuations by High Magnetic-Fields." Journal of Magnetism and Magnetic Materials **100**(1-3): 292-321.

Jackson, J. D. (1999). Classical electrodynamics. New York, Wiley.
Jie, Q., R. W. Hu, E. Bozin, A. Llobet, I. Zaliznyak, C. Petrovic and Q. Li (2012). "Electronic thermoelectric power factor and metal-insulator transition in FeSb2." Physical Review B **86**(11).

Ju, W. W., G. Q. Liu and Z. Q. Yang (2013). "Exotic spin-orbital Mott insulating states in BaIrO3." Physical Review B **87**(7).

Jungwirth, T., Q. Niu and A. H. MacDonald (2002). "Anomalous Hall effect in ferromagnetic semiconductors." Physical Review Letters **88**(20).

Kambe, S., Y. Tokunaga, H. Sakai, T. D. Matsuda, Y. Haga, Z. Fisk and R. E. Walstedt (2013). "NMR Study of In-Plane Twofold Ordering in URu2Si2." Physical Review Letters **110**(24).

Kambe, S., Y. Tokunaga, H. Sakai and R. E. Walstedt (2015). "Distributed twofold ordering in URu2Si2." Physical Review B **91**(3).

Kapitza, P. (1928). "The study of the specific resistance of bismuth crystals and its change in strong magnetic fields and some allied problems." Proceedings of the Royal Society of London Series a-Containing Papers of a Mathematical and Physical Character **119**(782): 401-443.

Karplus, R. and J. M. Luttinger (1954). "Hall Effect in Ferromagnetics." Physical Review **95**(5): 1154-1160.

Kida, T., S. Yoshii, M. Hagiwara, T. Nakano and I. Terasaki (2009). "Nanoscale spin-dependent transport in a weak itinerant ferromagnet BaIrO(3)." 25th International Conference on Low Temperature Physics (Lt25), Part 2 **150**.

Kim, B. J., H. Jin, S. J. Moon, J. Y. Kim, B. G. Park, C. S. Leem, J. Yu, T. W. Noh, C. Kim, S. J. Oh, J. H. Park, V. Durairaj, G. Cao and E. Rotenberg (2008). "Novel

J(eff)=1/2 Mott state induced by relativistic spin-orbit coupling in Sr2IrO4." Physical Review Letters **101**(7).

Kim, S. J., D. H. Lim, S. J. Kim, C. S. Yoon and C. K. Kim (2003). "Magnetic properties of phase-separated (Ni80Fe20)(1-x)Mn-x thin films." Ieee Transactions on Magnetics **39**(5): 2690-2692.

Kini, N. S., A. Bentien, S. Ramakrishnan and C. Geibel (2005). "Specific heat and transport study of the co-existence of charge-density-wave and weak ferromagnetism in BaIrO3." Physica B-Condensed Matter **359**: 1264-1266.

Klimm, D. (2014). "Electronic materials with a wide band gap: recent developments." Iucrj **1**: 281-290.

Kosterlitz, J. M. and D. J. Thouless (1973). "Ordering, Metastability and Phase-Transitions in 2 Dimensional Systems." Journal of Physics C-Solid State Physics **6**(7): 1181-1203.

Kurmaev, E. Z., A. Moewes, I. R. Shein, L. D. Finkelstein, A. L. Ivanovskii and H. Anno (2004). "Electronic structure and thermoelectric properties of skutterudite compounds." Journal of Physics-Condensed Matter **16**(6): 979-987.

Lecheminant, P., B. Bernu, C. Lhuillier, L. Pierre and P. Sindzingre (1997). "Order versus disorder in the quantum Heisenberg antiferromagnet on the kagome lattice using exact spectra analysis." Physical Review B **56**(5): 2521-2529.

Lederer, P. and D. L. Mills (1968). "Intra-Atomic Coulomb Interactions and Local Exchange-Enhancement Effects in Dilute Transition-Metal Alloys." Physical Review Letters **20**(19): 1036-&.

Lee, M., T. F. Rosenbaum, M. L. Saboungi and H. S. Schnyders (2002). "Band-gap tuning and linear magnetoresistance in the silver chalcogenides." Physical Review Letters **88**(6).

Lee, P. A. and T. V. Ramakrishnan (1985). "Disordered Electronic Systems." Reviews of Modern Physics **57**(2): 287-337.
Lee, S. H., H. Kikuchi, Y. Qiu, B. Lake, Q. Huang, K. Habicht and K. Kiefer (2007). "Quantum-spin-liquid states in the two-dimensional kagome antiferromagnets ZnxCu4-x(OD)(6)Cl-2." Nature Materials **6**(11): 853-857.

Li, K., Y. F. Hu, Y. X. Wang, T. Kamiyama, B. W. Wang, Z. F. Li and J. H. Lin (2014). "Syntheses and properties of a family of new compounds RE3Sb3Co2O14

(RE=La, Pr, Nd, Sm-Ho) with an ordered pyrochlore structure." Journal of Solid State Chemistry **217**: 80-86.

Li, L., P. P. Kong, T. F. Qi, C. Q. Jin, S. J. Yuan, L. E. DeLong, P. Schlottmann and G. Cao (2013). "Tuning the J(eff)=1/2 insulating state via electron doping and pressure in the double-layered iridate Sr3Ir2O7." Physical Review B **87**(23).

Li, R. W., H. B. Wang, X. W. Wang, X. Z. Yu, Y. Matsui, Z. H. Cheng, B. G. Shen, E. W. Plummer and J. D. Zhang (2009). "Anomalously large anisotropic magnetoresistance in a perovskite manganite." Proceedings of the National Academy of Sciences of the United States of America **106**(34): 14224-14229.

Limelette, P., W. Saulquin, H. Muguerra and D. Grebille (2010). "From quantum criticality to enhanced thermopower in strongly correlated layered cobalt oxide." Physical Review B **81**(11).

Lowhorn, N. D., W. Wong-Ng, Z. Q. Lu, J. Martin, M. L. Green, J. E. Bonevich, E. L. Thomas, N. R. Dilley and J. Sharp (2011). "Development of a Seebeck coefficient Standard Reference Material (TM)." Journal of Materials Research **26**(15): 1983-1992.

Luo, Y. K., H. Chen, J. H. Dai, Z. A. Xu and J. D. Thompson (2015). "Heavy surface state in a possible topological Kondo insulator: Magnetothermoelectric transport on the (011) plane of SmB6." Physical Review B **91**(7).

Luttinger, J. M. and L. Tisza (1946). "Theory of Dipole Interaction in Crystals." Physical Review **70**(11-1): 954-964.

Mahendiran, R. and P. Schiffer (2003). "Double magnetic transition in Pr0.5Sr0.5CoO3." Physical Review B **68**(2).

Maiti, K. (2006). "Electronic structure of BaIrO3: A first-principles study using the local spin density approximation." Physical Review B **73**(11).

Maiti, K., R. S. Singh, V. R. R. Medicherla, S. Rayaprol and E. V. Sampathkumaran (2005). "Origin of charge density wave formation in insulators from a high resolution photoemission study of BaIrO3." Physical Review Letters **95**(1).

Maksymenko, M., V. R. Chandra and R. Moessner (2015). "Classical dipoles on the kagome lattice." Physical Review B **91**(18).

Mallik, R. C., C. Stiewe, G. Karpinski, R. Hassdorf and E. Muller (2009). "Thermoelectric Properties of Co4Sb12 Skutterudite Materials with Partial In Filling and Excess In Additions." Journal of Electronic Materials **38**(7): 1337-1343.

Manyala, N., Y. Sidis, J. F. DiTusa, G. Aeppli, D. P. Young and Z. Fisk (2000). "Magnetoresistance from quantum interference effects in ferromagnets (vol 404, pg 581, 2000)." Nature **408**(6812): 616-U618.

Matsuda, T. D., E. Hassinger, D. Aoki, V. Taufour, G. Knebel, N. Tateiwa, E. Yamamoto, Y. Haga, Y. Onuki, Z. Fisk and J. Flouquet (2011). "Details of Sample Dependence and Transport Properties of URu2Si2." Journal of the Physical Society of Japan **80**(11).

Mcguire, T. R. and R. I. Potter (1975). "Anisotropic Magnetoresistance in Ferromagnetic 3d Alloys." Ieee Transactions on Magnetics **11**(4): 1018-1038.

Melko, R. G., B. C. den Hertog and M. J. P. Gingras (2001). "Long-range order at low temperatures in dipolar spin ice." Physical Review Letters **87**(6).

Metoki, N., H. Sakai, E. Yamamoto, N. Tateiwa, T. Matsuda and Y. Haga (2013). "Neutron Scattering Experiments for the Study of In-Plane Ordered Moment in URu2Si2." Journal of the Physical Society of Japan **82**(5).

Mirebeau, I., A. Apetrei, J. Rodriguez-Carvajal, P. Bonville, A. Forget, D. Colson, V. Glazkov, J. P. Sanchez, O. Isnard and E. Suard (2005). "Ordered spin ice state and magnetic fluctuations in Tb2Sn2O7." Physical Review Letters **94**(24).

Mito, T., M. Hattori, G. Motoyama, Y. Sakai, T. Koyama, K. Ueda, T. Kohara, M. Yokoyama and H. Amitsuka (2013). "Investigation of Local Symmetries in the Hidden-Order Phase of URu2Si2." Journal of the Physical Society of Japan **82**(12).

Miyako, Y., S. Kawarazaki, H. Amitsuka, C. C. Paulsen and K. Hasselbach (1991). "Magnetic-Properties of U(Ru1-Xrhx)2si2 Single-Crystals (O-Less-Than-or-Equal-to-X-Less-Than-or-Equal-to-1)." Journal of Applied Physics **70**(10): 5791-5793.

Moore, J. E. (2010). "The birth of topological insulators." Nature **464**(7286): 194-198.

Morelli, D. T., T. Caillat, J. P. Fleurial, A. Borshchevsky, J. Vandersande, B. Chen and C. Uher (1995). "Low-Temperature Transport-Properties of P-Type Cosb3." Physical Review B **51**(15): 9622-9628.

Mott, N. F. and E. A. Davis (1979). Electronic processes in non-crystalline materials. Oxford New York, Clarendon Press; Oxford University Press.

Moustakas, T. D., K. Weiser and A. J. Grant (1975). "Anomalous Thermoelectric-Power of Some Liquid Chalcogenide Systems." Solid State Communications **16**(5): 575-579.

Mydosh, J. A. and P. M. Oppeneer (2011). "Colloquium: Hidden order, superconductivity, and magnetism: The unsolved case of URu2Si2." Reviews of Modern Physics **83**(4).

Nagai, O., S. Miyashita and T. Horiguchi (1993). "Ground-State of the Antiferromagnetic Ising-Model of General Spin-S on a Triangular Lattice." Physical Review B **47**(1): 202-205.

Nagaosa, N., J. Sinova, S. Onoda, A. H. MacDonald and N. P. Ong (2010). "Anomalous Hall effect." Reviews of Modern Physics **82**(2): 1539-1592.

Nakano, T. and I. Terasaki (2006). "Giant nonlinear conduction and thyristor-like negative differential resistance in BaIrO3 single crystals." Physical Review B **73**(19).

Nayak, C., S. H. Simon, A. Stern, M. Freedman and S. Das Sarma (2008). "Non-Abelian anyons and topological quantum computation." Reviews of Modern Physics **80**(3): 1083-1159.

Niklowitz, P. G., S. R. Dunsiger, C. Pfleiderer, P. Link, A. Schneidewind, E. Faulhaber, M. Vojta, Y. K. Huang and J. A. Mydosh (2015). "Role of commensurate and incommensurate low-energy excitations in the paramagnetic to hidden-order transition of URu2Si2." Physical Review B **92**(11).

Ohkuni, H., Y. Inada, Y. Tokiwa, K. Sakurai, R. Settai, T. Honma, Y. Haga, E. Yamamoto, Y. Onuki, H. Yamagami, S. Takahashi and T. Yanagisawa (1999). "Fermi surface properties and de Haas-van Alphen oscillation in both the normal and superconducting mixed states of URu2Si2." Philosophical Magazine B-Physics of Condensed Matter Statistical Mechanics Electronic Optical and Magnetic Properties **79**(7): 1045-1077.

Okamoto, Y., M. Nohara, H. Aruga-Katori and H. Takagi (2007). "Spin-liquid state in the S=1/2 hyperkagome antiferromagnet Na4Ir3O8." Physical Review Letters **99**(13).

Okamoto, Y., H. Yoshida and Z. Hiroi (2009). "Vesignieite BaCu3V2O8(OH)(2) as a Candidate Spin-1/2 Kagome Antiferromagnet." Journal of the Physical Society of Japan **78**(3).

Okazaki, R., T. Shibauchi, H. J. Shi, Y. Haga, T. D. Matsuda, E. Yamamoto, Y. Onuki, H. Ikeda and Y. Matsuda (2011). "Rotational Symmetry Breaking in the Hidden-Order Phase of URu2Si2." Science **331**(6016): 439-442.

Oliver, M. R., Mcwhorte.Al, J. O. Dimmock and T. B. Reed (1972). "Conductivity Studies in Europium Oxide." Physical Review B **5**(3): 1078-&.

Olsen, J. L. (1962). Electron transport in metals. New York,, Interscience Publishers.

Onsager, L. (1939). "Electrostatic interaction of molecules." Journal of Physical Chemistry **43**(2): 189-196.

Ott, H. R., H. Rudigier, Z. Fisk and J. L. Smith (1983). "Ube13 - an Unconventional Actinide Superconductor." Physical Review Letters **50**(20): 1595-1598.

Palstra, T. T. M., A. A. Menovsky, J. Vandenberg, A. J. Dirkmaat, P. H. Kes, G. J. Nieuwenhuys and J. A. Mydosh (1985). "Superconducting and Magnetic Transitions in the Heavy-Fermion System Uru2si2." Physical Review Letters **55**(24): 2727-2730.

Pardo, V., J. C. Smith and W. E. Pickett (2012). "Linear bands, zero-momentum Weyl semimetal, and topological transition in skutterudite-structure pnictides." Physical Review B **85**(21).

Parish, M. M. and P. B. Littlewood (2003). "Non-saturating magnetoresistance in heavily disordered semiconductors." Nature **426**(6963): 162-165.

Parish, M. M. and P. B. Littlewood (2005). "Classical magnetotransport of inhomogeneous conductors." Physical Review B **72**(9).

Paul, I. and G. Kotliar (2001). "Thermoelectric behavior near the magnetic quantum critical point." Physical Review B **64**(18).

Petrovic, C., J. W. Kim, S. L. Bud'ko, A. I. Goldman, P. C. Canfield, W. Choe and G. J. Miller (2003). "Anisotropy and large magnetoresistance in the narrow-gap semiconductor FeSb2." Physical Review B **67**(15).

Phillips, P. and C. Chamon (2005). "Breakdown of one-parameter scaling in quantum critical scenarios for high-temperature copper-oxide superconductors." Physical Review Letters **95**(10).

Picot, T. and D. Poilblanc (2015). "Nematic and supernematic phases in kagome quantum antiferromagnets under the influence of a magnetic field." Physical Review B **91**(6).

Pippard, A. B. (1989). Magnetoresistance in metals. Cambridge Cambridgeshire ; New York, Cambridge University Press.

Pugh, E. M. (1930). "Hall effect and the magnetic properties of some ferromagnetic materials." Physical Review **36**(9): 1503-1511.
Qi, X. L. and S. C. Zhang (2011). "Topological insulators and superconductors." Reviews of Modern Physics **83**(4).

Ramirez, A. P. (1997). "Colossal magnetoresistance." Journal of Physics-Condensed Matter **9**(39): 8171-8199.

Ramirez, A. P., P. Coleman, P. Chandra, E. Bruck, A. A. Menovsky, Z. Fisk and E. Bucher (1992). "Nonlinear Susceptibility as a Probe of Tensor Spin Order in Uru2si2." Physical Review Letters **68**(17): 2680-2683.

Ramirez, A. P., G. P. Espinosa and A. S. Cooper (1990). "Strong Frustration and Dilution-Enhanced Order in a Quasi-2d Spin-Glass." Physical Review Letters **64**(17): 2070-2073.

Ramirez, A. P., A. Hayashi, R. J. Cava, R. Siddharthan and B. S. Shastry (1999). "Zero-point entropy in 'spin ice'." Nature **399**(6734): 333-335.

Ramirez, A. P., B. S. Shastry, A. Hayashi, J. J. Krajewski, D. A. Huse and R. J. Cava (2002). "Multiple field-induced phase transitions in the geometrically frustrated dipolar magnet: Gd2Ti2O7." Physical Review Letters **89**(6).

Ramirez, A. P., T. Siegrist, T. T. M. Palstra, J. D. Garrett, E. Bruck, A. A. Menovsky and J. A. Mydosh (1991). "Superconducting Phases of Uru2si2." Physical Review B **44**(10): 5392-5395.

Rau, J. G. and H. Y. Kee (2012). "Hidden and antiferromagnetic order as a rank-5 superspin in URu2Si2." Physical Review B **85**(24).

Rautama, E. L., P. Boullay, A. K. Kundu, V. Caignaert, V. Pralong, M. Karppinen and B. Raveau (2008). "Cationic ordering and microstructural effects in the ferromagnetic perovskite La0.5Ba0.5CoO3: Impact upon magnetotransport properties." Chemistry of Materials **20**(8): 2742-2750.

Renard, J. P., P. Bruno, R. Megy, B. Bartenlian, P. Beauvillain, C. Chappert, C. Dupas, E. Kolb, M. Mulloy, J. Prieur, P. Veillet and E. Velu (1996). "Inverse giant magnetoresistance." Journal of Applied Physics **79**(8): 5270-5275.

Riggs, S. C., M. C. Shapiro, A. V. Maharaj, S. Raghu, E. D. Bauer, R. E. Baumbach, P. Giraldo-Gallo, M. Wartenbe and I. R. Fisher (2015). "Evidence for a nematic component to the hidden-order parameter in URu2Si2 from differential elastoresistance measurements." Nature Communications **6**.

Ross, K. A., L. Harriger, Z. Yamani, W. J. L. Buyers, J. D. Garrett, A. A. Menovsky, J. A. Mydosh and C. L. Broholm (2014). "Strict limit on in-plane ordered magnetic dipole moment in URu2Si2." Physical Review B **89**(15).

Rowe, D. M. (1995). CRC handbook of thermoelectrics. Boca Raton, FL, CRC Press.

Sachdev, S. (1992). "Kagome-Lattice and Triangular-Lattice Heisenberg Antiferromagnets - Ordering from Quantum Fluctuations and Quantum-Disordered Ground-States with Unconfined Bosonic Spinons." Physical Review B **45**(21): 12377-12396.

Saito, Y., Y. Nakamura, M. S. Bahramy, Y. Kohama, J. T. Ye, Y. Kasahara, Y. Nakagawa, M. Onga, M. Tokunaga, T. Nojima, Y. Yanase and Y. Iwasa (2016). "Superconductivity protected by spin-valley locking in ion-gated MoS2." Nature Physics **12**(2): 144-+.

Sales, B. C., D. Mandrus and R. K. Williams (1996). "Filled skutterudite antimonides: A new class of thermoelectric materials." Science **272**(5266): 1325-1328.

Sanders, M. B., J. W. Krizan and R. J. Cava (2016). "RE3Sb3Zn2O14 (RE = La, Pr, Nd, Sm, Eu, Gd): a new family of pyrochlore derivatives with rare earth ions on a 2D Kagome lattice." Journal of Materials Chemistry C **4**(3): 541-550.

Savary, L., K. A. Ross, B. D. Gaulin, J. P. C. Ruff and L. Balents (2012). "Order by Quantum Disorder in Er2Ti2O7." Physical Review Letters **109**(15).

Schaffer, R., S. Bhattacharjee and Y. B. Kim (2013). "Spin-orbital liquids in non-Kramers magnets on the kagome lattice." Physical Review B **88**(17).

Schmidt, M. A., D. M. Silevitch, G. Aeppli and T. F. Rosenbaum (2014). "Using thermal boundary conditions to engineer the quantum state of a bulk magnet." Proceedings of the National Academy of Sciences of the United States of America **111**(10): 3689-3694.

Segal, A., O. Shaya, M. Karpovski and A. Gerber (2009). "Asymmetric field dependence of magnetoresistance in magnetic films." Physical Review B **79**(14).

Shankar, R. (1994). Principles of quantum mechanics. New York, Plenum Press.

Sharp, J. W., E. C. Jones, R. K. Williams, P. M. Martin and B. C. Sales (1995). "Thermoelectric Properties of Cosb3 and Related Alloys." Journal of Applied Physics **78**(2): 1013-1018.

Shi, X., J. Yang, J. R. Salvador, M. F. Chi, J. Y. Cho, H. Wang, S. Q. Bai, J. H. Yang, W. Q. Zhang and L. D. Chen (2011). "Multiple-Filled Skutterudites: High Thermoelectric Figure of Merit through Separately Optimizing Electrical and Thermal Transports." Journal of the American Chemical Society **133**(20): 7837-7846.

Shklovskiĭ, B. I. and A. L. Ėfros (1984). Electronic properties of doped semiconductors. Berlin ; New York, Springer-Verlag.
Siddharthan, R., B. S. Shastry and A. P. Ramirez (2001). "Spin ordering and partial ordering in holmium titanate and related systems." Physical Review B **63**(18).

Siddharthan, R., B. S. Shastry, A. P. Ramirez, A. Hayashi, R. J. Cava and S. Rosenkranz (1999). "Ising pyrochlore magnets: Low-temperature properties, "ice rules," and beyond." Physical Review Letters **83**(9): 1854-1857.

Siegrist, T. and B. L. Chamberland (1991). "The Crystal-Structure of Bairo3." Journal of the Less-Common Metals **170**(1): 93-99.

Singh, D. J. and W. E. Pickett (1994). "Skutterudite Antimonides - Quasi-Linear Bands and Unusual Transport." Physical Review B **50**(15): 11235-11238.

Singh, S., R. K. Gopal, J. Sarkar and C. Mitra (2016). "Quantum and Classical Contributions to Linear Magnetoresistance in Topological Insulator Thin Films." International Conference on Condensed Matter and Applied Physics (Icc 2015) **1728**.

Slack, G. A. and V. G. Tsoukala (1994). "Some Properties of Semiconducting Irsb3." Journal of Applied Physics **76**(3): 1665-1671.

Sluchanko, N. E., V. V. Glushkov, S. V. Demishev, A. A. Pronin, A. A. Volkkov, M. V. Kondrin, A. K. Savchenko and S. Kunii (2001). "Low-temperature transport anisotropy and many-body effects in SmB6." Physical Review B **64**(15).

Smit, J. (1955). "The Spontaneous Hall Effect in Ferromagnetics .1." Physica **21**(11): 877-887.

Smith, A. W. (1910). "The variation of the hall effect in metals with change of temperature." Physical Review **30**(1): 1-34.

Song, J., L. L. Wang, A. Zibart and C. Koch (2012). "Corrosion Protection of Electrically Conductive Surfaces." Metals **2**(4): 450-477.

Stewart, G. R. (1984). "Heavy-Fermion Systems." Reviews of Modern Physics **56**(4): 755-787.

Stewart, G. R., Z. Fisk, J. O. Willis and J. L. Smith (1984). "Possibility of Coexistence of Bulk Superconductivity and Spin Fluctuations in Upt3." Physical Review Letters **52**(8): 679-682.

Sun, P., N. Oeschler, S. Johnsen, B. B. Iversen and F. Steglich (2009). "FeSb2: Prototype of huge electron-diffusion thermoelectricity." Physical Review B **79**(15).

Sun, P., N. Oeschler, S. Johnsen, B. B. Iversen and F. Steglich (2009). "Huge Thermoelectric Power Factor: FeSb2 versus FeAs2 and RuSb2." Applied Physics Express **2**(9).

Sun, P., M. Sondergaard, Y. Sun, S. Johnsen, B. B. Iversen and F. Steglich (2011). "Unchanged thermopower enhancement at the semiconductor-metal transition in correlated FeSb2-xTex." Applied Physics Letters **98**(7).

Sun, P. J., N. Oeschler, S. Johnsen, B. B. Iversen and F. Steglich (2010). "Narrow band gap and enhanced thermoelectricity in FeSb2." Dalton Transactions **39**(4): 1012-1019.

Sun, P. J., B. P. Wei, D. Menzel and F. Steglich (2014). "Resonant charge relaxation as a likely source of the enhanced thermopower in FeSi." Physical Review B **90**(24).

Sun, P. J., W. H. Xu, J. M. Tomczak, G. Kotliar, M. Sondergaard, B. B. Iversen and F. Steglich (2013). "Highly dispersive electron relaxation and colossal thermoelectricity in the correlated semiconductor FeSb2." Physical Review B **88**(24).

Tabata, Y., H. Kadowaki, K. Matsuhira, Z. Hiroi, N. Aso, E. Ressouche and B. Fak (2006). "Kagome ice state in the dipolar spin ice Dy2Ti2O7." Physical Review Letters **97**(25).

Tafti, F. F., Q. D. Gibson, S. K. Kushwaha, N. Haldolaarachchige and R. J. Cava (2016). "Resistivity plateau and extreme magnetoresistance in LaSb." Nature Physics **12**(3): 272-+.

Tahir-Kheli, J. (2013). "Resistance of high-temperature cuprate superconductors." New Journal of Physics **15**.

Takagi, T. and M. Mekata (1993). "Magnetic-Ordering of Ising Spins on Kagome Lattice with the 1st and the 2nd Neighbor Interactions." Journal of the Physical Society of Japan **62**(11): 3943-3953.

Takagi, T. and M. Mekata (1995). "New partially disordered phases with commensurate spin density wave in frustrated triangular lattice." Journal of the Physical Society of Japan **64**(12): 4609-4627.

Takahashi, H., R. Okazaki, I. Terasaki and Y. Yasui (2013). "Origin of the energy gap in the narrow-gap semiconductor FeSb2 revealed by high-pressure magnetotransport measurements." Physical Review B **88**(16).

Takahashi, H., R. Okazaki, Y. Yasui and I. Terasaki (2011). "Low-temperature magnetotransport of the narrow-gap semiconductor FeSb2." Physical Review B **84**(20).

Takahashi, H., Y. Yasui, I. Terasaki and M. Sato (2011). "Effects of ppm-Level Imperfection on the Transport Properties of FeSb2 Single Crystals." Journal of the Physical Society of Japan **80**(5).

Takegahara, K. and H. Harima (2003). "Systematic study of electronic band structures for binary skutterudite compounds." Physica B-Condensed Matter **328**(1-2): 74-76.

Tari, A. (2003). The specific heat of matter at low temperatures. London River Edge, NJ, Imperial College Press; Distributed by World Scientific Pub. Co.

Terasaki, I., S. Ito, T. Igarashi, S. Asai, H. Taniguchi, R. Okazaki, Y. Yasui, K. Kobayashi, R. Kumai, H. Nakao and Y. Murakami (2016). "Novel Charge Ordering in the Trimer Iridium Oxide BaIrO3." Crystals **6**(3).

Tomczak, J. M., K. Haule and G. Kotliar (2013). "Thermopower of the Correlated Narrow Gap Semiconductor FeSi and Comparison to RuSi." New Materials for Thermoelectric Applications: Theory and Experiment: 45-57.

Tomczak, J. M., K. Haule, T. Miyake, A. Georges and G. Kotliar (2010). "Thermopower of correlated semiconductors: Application to FeAs2 and FeSb2." Physical Review B **82**(8).

Tonegawa, S., K. Hashimoto, K. Ikada, Y. H. Lin, H. Shishido, Y. Haga, T. D. Matsuda, E. Yamamoto, Y. Onuki, H. Ikeda, Y. Matsuda and T. Shibauchi (2012). "Cyclotron Resonance in the Hidden-Order Phase of URu2Si2." Physical Review Letters **109**(3).

Tonegawa, S., S. Kasahara, T. Fukuda, K. Sugimoto, N. Yasuda, Y. Tsuruhara, D. Watanabe, Y. Mizukami, Y. Haga, T. D. Matsuda, E. Yamamoto, Y. Onuki, H. Ikeda, Y. Matsuda and T. Shibauchi (2014). "Direct observation of lattice symmetry breaking at the hidden-order transition in URu2Si2." Nature Communications **5**.
Tritt, T. M. (2011). "Thermoelectric Phenomena, Materials, and Applications." Annual Review of Materials Research, Vol 41 **41**: 433-448.

Van der Pauw, L. (1958). "A method of measuring specific resistivity and Hall effect of discs of arbitrary shape." Philips Research Reports **13**(1): 1-9.
Vining, C. B. (2009). "An inconvenient truth about thermoelectrics." Nature Materials **8**(2): 83-85.

Wagner-Reetz, M., D. Kasinathan, W. Schnelle, R. Cardoso-Gil, H. Rosner, Y. Grin and P. Gille (2014). "Phonon-drag effect in FeGa3." Physical Review B **90**(19).

Wakeham, N. and N. E. Hussey (2012). "Hall effect in quasi-one-dimensional metals in the presence of anisotropic scattering." Physical Review B **85**(23).
Wang, C. M. and X. L. Lei (2012). "Linear magnetoresistance on the topological surface." Physical Review B **86**(3).

Wang, L., K. F. Cai, Y. Y. Wang, H. Li and H. F. Wang (2009). "Thermoelectric properties of indium-filled skutterudites prepared by combining solvothermal synthesis and melting." Applied Physics a-Materials Science & Processing **97**(4): 841-845.

Webster, J. G. (1999). The measurement, instrumentation, and sensors handbook. The electrical engineering handbook series. Boca Raton, Fla., CRC Press : IEEE Press,**:** 1 v. (various pagings).

Weinstein, E. W. "Euler Characteristic." Retrieved Oct. 31, 2014, from http://mathworld.wolfram.com/EulerCharacteristic.html.

Wen, X.-G. (2004). Quantum field theory of many-body systems : from the origin of sound to an origin of light and electrons. Oxford ; New York, Oxford University Press.

Whangbo, M. H. and H. J. Koo (2001). "Structural and electronic features of BaIrO3 causing the simultaneous occurrence of weak ferromagnetism and charge density wave formation." Solid State Communications **118**(10): 491-495.

Wills, A. S., R. Ballou and C. Lacroix (2002). "Model of localized highly frustrated ferromagnetism: The kagome spin ice." Physical Review B **66**(14).

Wisniewski, P. (2007). "Giant anisotropic magnetoresistance and magnetothermopower in cubic 3 : 4 uranium pnictides." Applied Physics Letters **90**(19).

Witczak-Krempa, W., G. Chen, Y. B. Kim and L. Balents (2014). "Correlated Quantum Phenomena in the Strong Spin-Orbit Regime." Annual Review of Condensed Matter Physics, Vol 5 **5**: 57-82.

Wojciechowski, K. T. (2007). "Study of transport properties of the Co1-xRhxSb3." Journal of Alloys and Compounds **439**(1-2): 18-24.

Wolf, S. A., D. D. Awschalom, R. A. Buhrman, J. M. Daughton, S. von Molnar, M. L. Roukes, A. Y. Chtchelkanova and D. M. Treger (2001). "Spintronics: A spin-based electronics vision for the future." Science **294**(5546): 1488-1495.

Wray, L. A., J. Denlinger, S. W. Huang, H. W. He, N. P. Butch, M. B. Maple, Z. Hussain and Y. D. Chuang (2015). "Spectroscopic Determination of the Atomic f-Electron Symmetry Underlying Hidden Order in URu2Si2." Physical Review Letters **114**(23).

Xia, Y., D. Qian, D. Hsieh, L. Wray, A. Pal, H. Lin, A. Bansil, D. Grauer, Y. S. Hor, R. J. Cava and M. Z. Hasan (2009). "Observation of a large-gap topological-insulator class with a single Dirac cone on the surface." Nature Physics **5**(6): 398-402.

Yamada, H. and S. Takada (1972). "Negative Magnetoresistance of Ferromagnetic Metals Due to Spin Fluctuations." Progress of Theoretical Physics **48**(6A): 1828-1848.

Yang, J. (2005). "Potential applications of thermoelectric waste heat recovery in the automotive industry." ICT: 2005 24th International Conference on Thermoelectrics: 155-159.

Yin, W. H., Y. Y. Zhang, D. Y. Cao, J. Yang, W. Bai, Y. Chen, G. S. Wang, X. L. Dong, C. G. Duan and X. D. Tang (2015). "Highly orientated growth and characterization of La0.7Sr0.3MnO3 thin films with different orientations on SrTiO3

substrates by chemical solution deposition method." Journal of Applied Physics **117**(17).

Yuasa, S., T. Nagahama, A. Fukushima, Y. Suzuki and K. Ando (2004). "Giant room-temperature magnetoresistance in single-crystal Fe/MgO/Fe magnetic tunnel junctions." Nature Materials **3**(12): 868-871.

Zhang, H. J., C. X. Liu, X. L. Qi, X. Dai, Z. Fang and S. C. Zhang (2009). "Topological insulators in Bi2Se3, Bi2Te3 and Sb2Te3 with a single Dirac cone on the surface." Nature Physics **5**(6): 438-442.

Zhang, W., R. Yu, W. X. Feng, Y. G. Yao, H. M. Weng, X. Dai and Z. Fang (2011). "Topological Aspect and Quantum Magnetoresistance of beta-Ag2Te." Physical Review Letters **106**(15).

Zhang, X. and L. D. Zhao (2015). "Thermoelectric materials: Energy conversion between heat and electricity." Journal of Materiomics **1**: 92-95.

Zhang, Z. C., X. Feng, M. H. Guo, K. Li, J. S. Zhang, Y. B. Ou, Y. Feng, L. L. Wang, X. Chen, K. He, X. C. Ma, Q. K. Xue and Y. Y. Wang (2014). "Electrically tuned magnetic order and magnetoresistance in a topological insulator." Nature Communications **5**.

Zhao, J. G., L. X. Yang, K. Mydeen, F. Y. Li, R. C. Yu and C. Q. Jin (2008). "Effects of pressure on electrical property of BaIrO(3)." Solid State Communications **148**(9-10): 361-364.

Zhao, Y., W. Li, B. Xi, Z. Zhang, X. Yan, S. J. Ran, T. Liu and G. Su (2013). "Kosterlitz-Thouless phase transition and re-entrance in an anisotropic three-state Potts model on the generalized kagome lattice." Physical Review E **87**(3).

Zhou, H. D., B. W. Vogt, J. A. Janik, Y. J. Jo, L. Balicas, Y. Qiu, J. R. D. Copley, J. S. Gardner and C. R. Wiebe (2007). "Partial field-induced magnetic order in the spin-liquid kagome Nd(3)Ga(5)SiO(14)." Physical Review Letters **99**(23).

Zorko, A., F. Bert, P. Mendels, P. Bordet, P. Lejay and J. Robert (2008). "Easy-axis kagome antiferromagnet: Local-probe study of Nd(3)Ga(5)SiO(14)." Physical Review Letters **100**(14).